Accumulation, Gelation, and Crystallization of Prebiotic Molecules in a Thermal Gradient and Deep UV Circular Dichroism

Matthias Morasch

München 2019

Accumulation, Gelation, and Crystallization of Prebiotic Molecules in a Thermal Gradient and Deep UV Circular Dichroism

Matthias Morasch

Dissertation
an der Fakultät für Physik
der Ludwig–Maximilians–Universität
München

vorgelegt von
Matthias Morasch
aus München

München, den 22.03.2019

Zusammenfassung

Der Ort an dem das Leben entstanden ist hat die physikalischen Randbedingungen, unter denen sich die ersten replizierenden Systeme entwickelten, definiert. Dabei waren Nichtgleichgewichtssysteme notwendig, welche die Energie lieferten um diese anzutreiben. Eine solche Form von Nichtgleichgewicht stellen beispielsweise Temperaturgradienten dar, wie sie in porösem Gestein in hydrothermalen Quellen am Meeresboden möglich sind. Diese Arbeit behandelt die Auswirkungen von solchen Temperaturgradienten auf Moleküle in Lösung und die Frage wie man diese analysieren kann.

Im ersten Teil wird dabei die Akkumulation von selbstkomplementären Oligonukleotiden in einer thermischen Falle demonstriert. Die dabei stattfindende längenselektive Akkumulation führt zur Entstehung von Hydrogelen aus DNA in Lösung, ohne dabei Kondensationsmittel oder multivalente Ionen zu benötigen. Dieser Gelierungsprozess wird für DNA mit zwei oder drei selbstkomplementären Bindungsstellen und einer Länge von lediglich 24 Basen gezeigt. Kontrollversuche zeigen dabei, dass nicht-komplementäre DNA in Lösung bleibt und dass der Prozess nicht von der Interaktion der DNA mit Fluoreszenzfarbstoffen dominiert wird. Zwei selbstkomplementäre Stränge mit zueinander orthogonalen Sequenzen, also einer minimalen Komplementarität, bilden im Experiment sequenzreine Hydrogele

Im zweiten Teil wird die Akkumulation von Molekülen an Gas-Wasser-Grenzflächen in einem Temperaturgradienten gezeigt. In diesem System führt die lokale Verdunstung von Wasser an der warmen Seite der Grenzfläche zu einer Kapillarströmung hin zum Meniskus. Dies führt zu einer Akkumulation von Molekülen, welche eine mehr als 1000-fache Konzentration erreichen. Dieser Mechanismus akkumuliert größere Moleküle und daher auch längere Polymere besser. An dieser Grenzfläche kommt es zu einer stark erhöhten Aktivität des Hammerhead Ribozyms, da sowohl Oligonukleotide als auch das für die Aktivität wichtige Magnesium akkumuliert werden. Außerdem kommt es auch hier zur Gelierung selbstkomplementärer RNA sowie zum Einschluss von Molekülen in Vesikelclustern, zur Kristallisation von Ribose Aminooxazolin und zu einer gesteigerten Phosphorylierung von Nukleotiden. Eine vollständige Simulation des Akkumulationsmechanismus bestätigt die Ergebnisse.

Der dritte Teil beschreibt den Aufbau eines Circulardichroismus-Mikroskops (CDIM) im UV-Bereich. Ziel war es, den Circulardichroismus (CD) von präbiotischen Molekülen, wie etwa dem Vorprodukt von RNA Nukleotiden—Ribose Aminooxazolin—zu untersuchen und gleichzeitig dessen Akkumulation und eventuelle Kristallisation zu beobachten. In diesem Kapitel wird dabei die experimentelle Realisierung des CDIM gezeigt. Ein Schwerpunkt liegt dabei auf der Erzeugung von zirkular polarisiertem Licht mittels einem gepulsten UV-Laser und einem photoelastischen Modulator. Messungen von Proben mit einem bekannten CD wurden zur Kalibrierung des Systems verwendet. Die Ergebnisse zeigen, dass das CDIM eingeschränkt verwendet werden kann, um das Vorzeichen des CD einer Probe in Wasser zu bestimmen. Weitere Experimente sind jedoch notwendig um Artefakte auszuschließen und zu zeigen, ob man das System mit thermischen Fallen kombinieren kann.

Summary

The location at which life emerged on Earth defined the physical boundary conditions under which the first replicating systems evolved. Nonequilibrium systems were necessary to provide the energy driving these processes. One such nonequilibrium system could have been temperature gradients, found for example across porous rock in hydrothermal vents. The work presented here focuses on the effects of temperature gradients on molecules in these water-filled micro-compartments and on methods how they could be analyzed.

In the first part of this thesis, the accumulation of self-complementary oligonucleotides in a thermal trap is demonstrated. The length-selective accumulation in this system is used to create hydrogels from DNA in solution without the use of condensing agents or multivalent ions. This gelation process is demonstrated for DNA with two and three self-complementary binding sites and strands as short as 24mers. Control experiments show that non-complementary DNA stays in solution and that the process is not dominated by the interaction of DNA with fluorescent dyes. Two self-complementary strands with orthogonal sequences, i.e. a minimal sequence overlap, form pure hydrogels when accumulated together.

In part two, the accumulation of molecules at gas-water interfaces in a temperature gradient is demonstrated. In this system, the local evaporation of water at the warm side of the interface leads to a capillary flow towards the meniscus and therefore an accumulation of molecules in this area, reaching a more than 1000-fold concentration increase. This mechanism is length-dependent, accumulating larger molecules better. At the interface, the activity of the Hammerhead ribozyme strongly increases due to the combined accumulation of oligomers and magnesium. In addition, the accumulation can trigger the gelation of self-complementary RNA, the encapsulation of molecules in vesicle clusters, the crystallization of ribose aminooxazoline, and the enhanced phosphorylation of nucleotides. A full simulation of the accumulation mechanism confirms these results.

The third part describes the implementation of a circular dichroism imaging microscope (CDIM) in deep UV. The aim was to study the circular dichroism (CD) of prebiotic molecules such as the RNA precursor ribose aminooxazoline, while simultaneously observing its accumulation and possible crystallization. In this part, the experimental realization of the CDIM is shown, with a focus on the mechanisms to create circularly polarized light from a pulsed UV laser using a photoelastic modulator. Measurements of samples with a known CD were used to calibrate the system. The results show that the system might be used to determine the sign of the CD of a sample in water. However, further experiments are necessary to exclude measurement artifacts and investigate if the system can be combined with thermal traps.

Contents

Introduction

Evidence points towards the fact that life has been on Earth for more than 3.7 billion years. It was found for example in Greenland and Australia in form of stromatolites—sedimentary rocks assumed to have formed from microbes [1, 2]. The question, however, where and under which circumstances life developed on Earth remains one of the biggest unanswered questions of modern science. Most evidence from this time has been destroyed over the billions of years, making it virtually impossible to answer the question of how exactly life evolved on Earth. The goal is therefore to depict possible pathways for the emergence of the first living systems on early Earth and setting chemical, physical, and geological constraints. An important aspect of this task is to define the transition point from non-living to living matter. One of the most commonly used definitions is that

"life is a self-sustaining chemical system capable of Darwinian evolution" [3]. This chemical system must be independent of other living organisms and maintain its own metabolic and replicating system by harnessing energy from the environment. To fulfill these requirements, the environment in which it exists must be in a constant thermodynamic non-equilibrium, as famously stated by Erwin Schrödinger [4]. Otherwise, any chemical processes would eventually come to a rest and the system would die. The same principle is applicable to the emergence of life, before the first cells had formed. A simple replicator on early Earth would have required a continuous supply of feeding molecules and energy to maintain its replication and removal or recycling of waste products.

The environment in which it formed thereby sets the boundary conditions for the chemical and physical processes that could help to sustain it. These conditions should support and enhance the processes required to sustain the system and prevent its dilution to infinity.

Several distinct environments have been debated to be plausible or necessary for the origin of life. Settings with dry intermediate phases were deemed essential [5], because a wide range of prebiotic processes are inefficient in aqueous solutions. Examples are the phosphorylation of nucleosides, during which water competes for the activated phosphate intermediate [6, 7], or their subsequent polymerization [6, 8, 9]. Many of these processes require dry intermediate conditions and elevated temperatures, but their products are essential for the emergence of an informational polymer world. They can take place for example in hydrothermal ponds or small lakes that dry out and rehydrate over the years [5]. Meteoritic bombardment or interplanetary dust particles were suggested

as a delivery system to supply the ponds with new material. Thermal energy from these impacts, but also from the sun, would regularly lead to an evaporation of water, leading to high local concentrations and dry conditions that allow reactions such as the phosphorylation of nucleosides.

There are, however, also drawbacks to this system. Dry reactions are mostly efficient at high temperatures above 60 °C. At the same time, upon rehydration, enhanced hydrolysis leads to very short half-lifes of the nucleotides at these temperatures [10]. In a colder system, hydrolysis would be negligible, but at the same time dry reactions become very inefficient. In addition, the question remains how these environments would support the formation of the first cells. An encapsulation of molecules in lipids could still be feasible during drying processes, but the continuous dry-wet cycles would eventually have to end and the system should likely be connected to larger water bodies in order to promote the emergence and survival of simple microbial communities.

A second environment that has been argued as a potential site for the origin of life are hydrothermal vents [11–14]. These are regions on the ocean floor from which hot water emerges, heated for example by volcanic activity [15]. Reactions between the seawater and the ocean's crust could have created alkaline fluids and led to the formation of large chimneys [16] [17]. At such a site, temperature, ion (pH), and redox gradients could be created between the hot hydrothermal fluid and the cold ocean across porous rock, providing a continuous material and energy source for prebiotic processes.

It was hypothesized that protocells could have harnessed ion gradients as an energy source, similar to modern cells [18]. In addition, it was shown that temperature gradients across porous rock can enhance prebiotic processes by providing temperature cycles and high local concentrations due to a combination of convection and thermophoresis, the movement of molecules in a temperature gradient [12, 19]. This was shown to potentially enhance a polymerization reaction in water [20], lead to the formation of stable pH gradients [21], selectively accumulate longer replicating oligonucleotides over short ones [22], and form protocell-like vesicles [23]. The temperature gradient thereby implements a long-lasting non-equilibrium environment that drives the accumulation of molecules. This prevents chemical systems in the pores from being diluted into the ocean and provides a continuous supply of energy and building blocks.

The data presented here expands this setting of thermal gradients. It focuses on the implications of self-complementarity on nucleic acids in these systems and introduces gas-water surface interactions to it. The experiments address some of the main questions of the origin of life—namely how nucleic acid sequences can be selected and separated from a mixed pool of oligonucleotides, how RNA can be concentrated and encapsulated in lipid vesicles, how dry reactions are possible in a submerged system, and how RNA building blocks can be selected and potentially enantiomerically separated in the pores. An approach is shown on how the enantiomeric excess could be analyzed in situ.

The aim of these experiments is to demonstrate how geophysical environments can be reconciled with prebiotic chemistry. As life did not evolve in a test tube, the physical constraints set by the environment have to be considered when regarding life's chemical origin. At the same time, these geological habitats need to support a wide variety of processes to enable the transition from non-living to living matter that eventually fulfills our definition for life.

DNA Gelation

2.1 Summary

Nucleic acids, one of the most abundant molecules in biology, can store large amounts of information in a condensed state at an unprecedented density [24]. At the same time, they can locally unwind and re-pack to allow their information to be transcribed at any moment. The ability of nucleic acids to efficiently condense, for example by self-organization processes, is essential for the development of life and was intensively researched over the last decades [25, 26]. During life's origin, a selection of hybridizing strands could have helped in the formation of e.g. ribozymes, where self-complementarity is essential for catalytic activity [27, 28]. In the following, a sol-gel phase transition of self-complementary DNA in water was induced by their accumulation in a thermal gradient. No condensing agents or multivalent ions were used. Nucleic acids formed a hydrogel from strands with two or three self-complementary binding sites and as short as 24 nts in length. The process is sequence-selective, giving rise to sequence-pure hydrogels from two self-complementary strands. The data presented in this chapter introduces the gelation process and its requirements. A further analysis of the sequence selectivity is given in the appended published article "Heat-Flow-Driven Oligonucleotide Gelation Separates Single-Base Differences".

2.2 Introduction

Condensation processes are usually described as phase transitions between the dilute (sol) phase and a dense phase with high concentrations of DNA and multiply charged ions or proteins. One example is the condensation of DNA, assisted [25, 29] by spermidine^{3+}, $Co(NH_3)_6^{3+}$, or other condensing agents, including cationic lipids, polymers, and metal complexes [26]. Monovalent ions, on the contrary, only partially shield the repulsion force between the DNA strands. This hinders strand condensation without the help of neutral polymers [30, 31].

In pure water, complementary DNA strands can self-organize into liquid crystals (LC) at high concentrations (300-1000 mg/ml) during drying processes [32]. Interestingly, this process was found to select for complementary strands from a pool of random sequences during their concentration [33], forming initial conditions for abiotic ligation [34].

DNA self-organization into almost arbitrary, nanometer-precise shapes is possible with DNA origami [35]. In this method, the DNA sequence dominates the ordering process: multiple short strands act as a molecular glue and can reshape a large viral DNA into sophisticated, three-dimensional structures during a slow cool-down [36]. The resulting objects were used as intracellular transportation vehicles [37], plasmonic metamolecules [38], or ruler in superresolution microscopy [39, 40].

The formation of hydrogels from complementary DNA strands was observed using self-assembling DNA nanostars [41]. The structure, dynamics, and aging properties of the hydrogels depended strongly on the hybridization strength and internal flexibility of the nanostars.

The experiments discussed above illustrate the diversity of DNA self-assembly and aggregation, though they look at the respective end-point of the ordering process: the DNA resides in an equilibrium state after an external change of the hydration shell (often for example by drying), salt concentrations, or an addition of condensing agents. In the following, the formation of DNA hydrogels in a non-equilibrium environment is demonstrated that requires only a minimal set of short DNA strands in PBS buffer (137 mM NaCl, 2.7 mM KCl, 10 mM phosphate buffer). No multivalent ions or other condensing agents were used. A constant temperature gradient across a water-filled pore accumulated the nucleic acids above the gelation threshold, making use of the hyperexponential escalation in a thermal gradient demonstrated by Mast *et. al.* [20]. The key mechanism, the accumulation of molecules in a temperature gradient, is based on thermophoresis.

2.2.1 Thermophoresis

Thermophoresis is the directed movement of molecules along a temperature gradient. In solution, most charged biomolecules such as DNA or RNA move from the warm to the cold side. The movement is described by the thermophoretic mobility D_T along the temperature gradient ∇T. The drift velocity v of the molecules in the temperature gradient is

$$v = -D_T \nabla T. \tag{2.1}$$

Under dilute conditions [42], the flow density of molecules in the temperature gradient

is then given by

$$j = j_D + j_{D_T} = -D \cdot \nabla c - D_T \cdot c \cdot \nabla T \tag{2.2}$$

with the diffusion coefficient D and the concentration gradient ∇c [43–45]. In steady state ($j = 0$) and assuming the temperature gradient to be linear, the concentration of a molecule depends only on the temperature difference $T - T_0$ with the cold temperature T_0. It can be calculated *via* the relation

$$\frac{c}{c_0} = exp[-S_T(T - T_0)] \tag{2.3}$$

with the Soret coefficient $S_T = \frac{D_T}{D}$ and the initial concentration c_0.

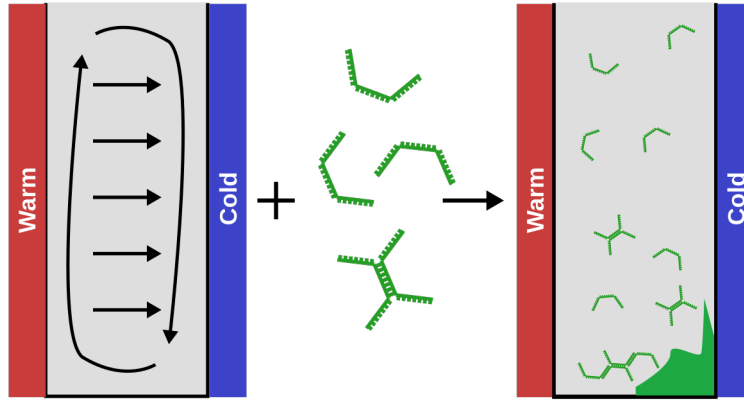## 2.2.2 Thermal Trapping

Figure 2.1: Principles of thermal trapping. A horizontal temperature gradient across a vertically aligned water-filled pore leads to convection of water (left, circular arrows) and thermophoresis (horizontal arrows). The combination of both accumulates the molecules on the bottom cold side of the pore. Self-complementary DNA (green) that can form larger networks is illustrated here to form a hydrogel in the accumulation region.

In the beginning of the 20th century, Clusius and Dickel described the separation of gases and isotopes between a cold and a hot wall based on the combination of thermodiffusion and gravitational convection. This led to the accumulation of heavier components on the bottom of the apparatus and lighter components on the top. In this work, a similar principle was used to accumulate (trap) molecules in water. Consider an upright, rectangular, water-filled pore (Figure 2.1) that is heated on one side and cooled on the other side. Due to this horizontal temperature gradient, the term j_c describing the convection of water due to its thermal expansion has to be added to Equation 2.2, which now reads

$$j = j_D + j_{D_T} + j_c = -D \cdot \nabla c - D_T \cdot c \cdot \nabla T + v_c \cdot c \tag{2.4}$$

with the convection speed v_c. The maximum concentration in a chamber with height h and width w can then be approximated by

$$\frac{c_{bottom}}{c_{top}} = exp\left(0.42 \cdot S_T \cdot \Delta T \cdot h \cdot w^{-1}\right) \tag{2.5}$$

with the temperature difference ΔT across the width of the chamber [12] and the concentrations at the bottom and top of the pore c_{bottom} and c_{top}, respectively.

2.3 Laser-Driven Accumulation of Self-Complementary DNA

2.3.1 Experimental Setup

The experimental setup (Figure 2.2) used in the following experiments differed from the model of thermogravitational trapping described above and was the same as in previous experiments [20]. The water-filled capillary was not vertically but horizontally aligned and the convection flows were induced artificially using a laser. To this end, the capillary was placed onto a silicon wafer that was cooled to 10 °C. One end of the capillary was connected to a syringe system, the other end was connected to a buffer reservoir. This allowed a controlled flushing of the system. The capillary was imaged from above using a fluorescence microscope. The temperature gradient was induced using a 1940 nm infrared (IR) laser, which was reflected from a mirror system and focused inside the capillary. The mirror system moved the laser spot along an approximately 7 mm long accumulation region in the capillary. When running, the laser first moved from one end of the accumulation region to the center of the capillary, then jumped to the other end and again moved inwards to the center. This asymmetric pattern was repeated at a frequency of 200 Hz and induced a flow pattern as shown in Figure 2.2 through thermoviscous pumping [46, 47]. Because the laser was focused in the center of the capillary, a temperature gradient was created along the x-direction, with the warmest region in the middle at 60 °C and the coldest at the edges in x-direction at 53 °C. In addition to thermophoresis, this temperature gradient also caused a gravitational convection roll perpendicular to the flows induced by thermoviscous pumping (Figure 2.2, top right).

The combination of thermophoresis and the two flows then led to an accumulation of DNA in the center of the capillary. However, the two orthogonal flows created two separate traps with different accumulation characteristics (Figure 2.3). Finite element simulations show that the flow along the capillary in y-direction, induced by laser pumping, in combination with thermophoresis, predominantly accumulated short DNA strands of 37 base pairs (bps) in length for the here used geometry (dotted line). They were accumulated in the y-directional center of the capillary (Figure 2.2, top left, red marked areas). The orthogonal trap in x-z-direction accumulated very large DNA better, with an increasing efficiency with the DNA length (solid line). Its maximum efficiency was at approximately 21 kbps and it accumulated DNA in the center with respect to the x-axis of the capillary (Figure 2.2, top right, red marked area). Therefore, the first trap continuously supplied the system with new material from the edges of the accumulation region, while the second trap triggered the formation of DNA hydrogels along the capillary close to the center.

2.3.2 DNA Designs

Two different DNA designs were used to create DNA hydrogels in the thermal trap. The first design, called brDNA, was a single stranded DNA with three self-complementary binding sites (Figure 2.4, left; hybridization energy $\Delta G \approx 32$ kcal/mole per binding site, $T_M \approx 60$ °C per site). Several of these strands could bind to each other, forming a large
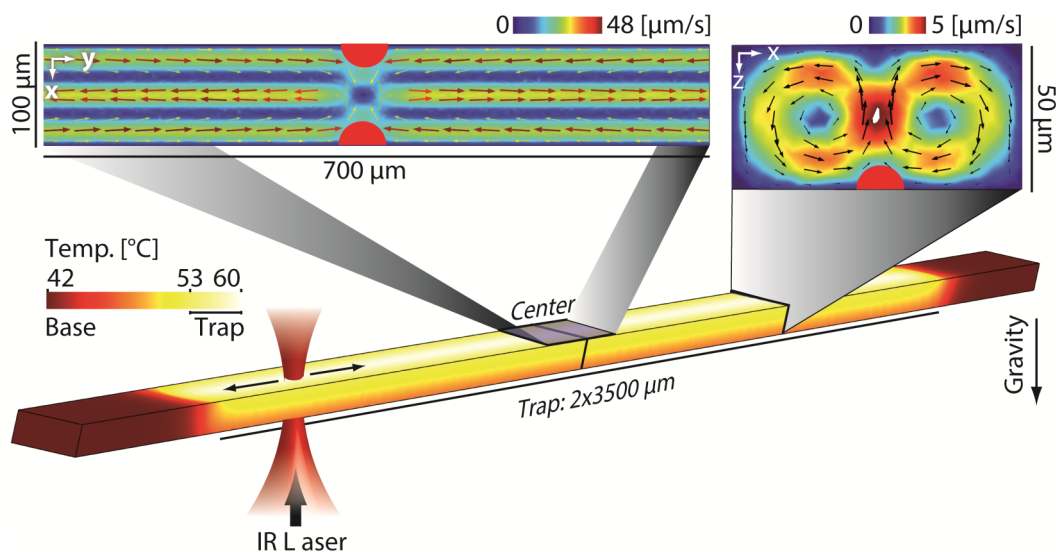
Figure 2.2: Setup for DNA gelation as described in [20]. Bottom: A water-filled borosilicate capillary (50 µm ·100 µm cross-section) was placed on a silicon wafer that was cooled by a Peltier device to 10 °C. From below, the water inside the capillary was heated by a 1940 nm IR laser focused in its center. This increased the base temperature to 42 °C and created a temperature gradient between the center and the edges of the capillary in x-direction. **Top left:** A movement of the laser along the y-axis induced a flow *via* thermoviscous pumping [46, 47] in the center and a subsequent back-flow at the edges, mimicking the gravitational convection. Flow speeds were calculated using finite element simulations. **Top right:** A second flow in the x-z plane was created by the temperature gradient, which generated a gravitational convection roll. The two flows in y- direction and the x-z-plane implemented two independent thermal traps with different accumulation characteristics. The first trap (y-direction) accumulates molecules in the horizontal center (red markings, top left), while the second trap induces high concentrations in the vertical center (red marking, top right) along the capillary. Reproduced from [48].

network of DNA. Each binding site could only bind to the same site on another strand, for example the center of a strand could only bind to the center of another strand. The pure GC-content of the sequences and the presence of a binding site in the center allowed also very short oligonucleotides down to 24mers to form a gel.

The second design, termed linDNA (Figure 2.4, right), was the same double-stranded DNA that had previously been used to demonstrate the escalation of polymerization in a thermal gradient [20]. It had a 95 base pairs long stem part in the center (melting temperature $T_M \approx 83$ °C) and two 25 nucleotide (nt) long sticky ends ($T_M \approx 67$ °C, ΔG = 46 kcal/mole), meaning that the two ends were self-complementary. Several of these strands could bind to each other and form one large dsDNA strand.
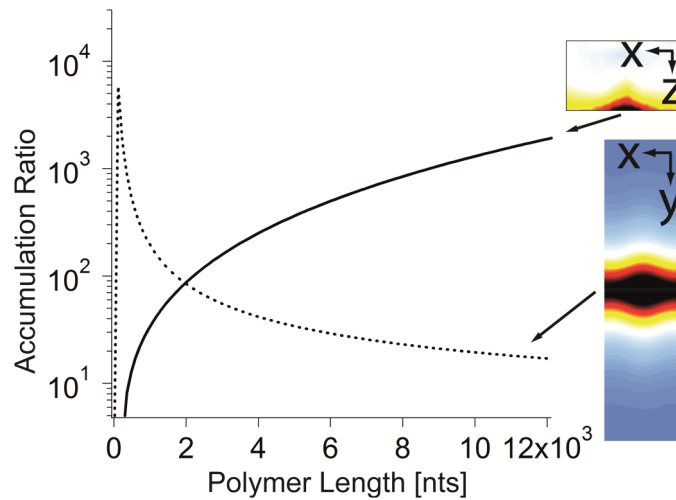
Figure 2.3: Characteristics of the two orthogonal traps from finite element simulations. The trap in x-y-direction (dotted line) predominantly accumulated DNA strands with a length of 37 bps in the center of the capillary (with respect to the y-direction). In contrast, the trap in x-z-direction (solid line) accumulated larger DNA along the capillary, with a maximum at 21 kbps. Reproduced from [48]
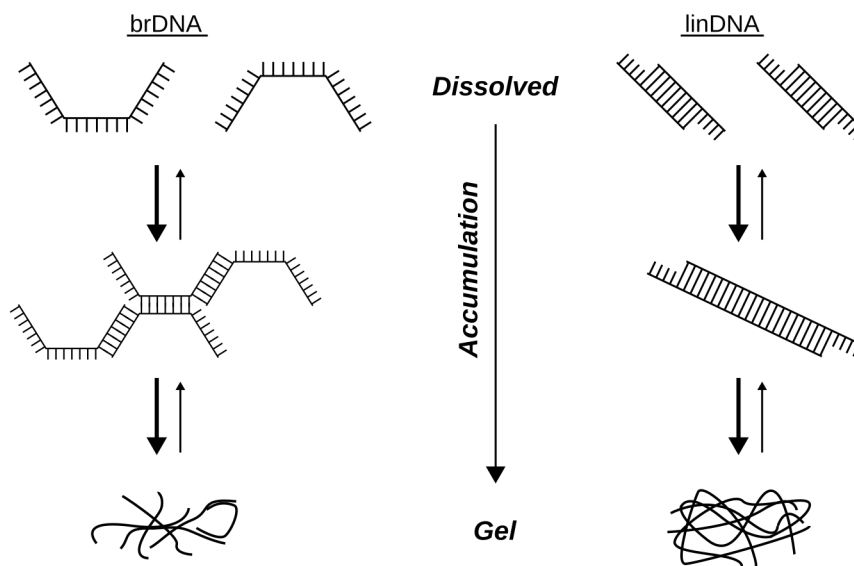

Figure 2.4: brDNA and linDNA structures. Left: The branching DNA (brDNA) had three separate self-complementary binding sites consisting only of the bases G and C. The binding sites allowed the DNA to form an ever larger network, forming a DNA hydrogel at high concentrations. In this work, several strands with lengths between 24 nts and 36 nts were used to demonstrate a brDNA gelation. Right: The 120mer linear DNA design (linDNA) consisted of a double-stranded 95 bps stem part with two 25 nts long sticky ends. Two or more of these strands could bind to each other and form one long dsDNA strand. At very high concentrations, these long strands eventually also formed a DNA hydrogel.

2.4 Results

2.4.1 DNA Gelation Overview

The length-selective accumulation described above was shown to hyperexponentially increase the concentration of double stranded (ds) DNA that had two self-complementary binding sites at its ends (linDNA) [20]. In the following, it is demonstrated that this mechanism eventually triggers the formation of DNA hydrogels. In addition, much shorter strands with three self-complementary binding sites, allowing the formation of an arbitrarily large DNA network (brDNA, Figure 2.4), are shown to create a similar gel.

Upon accumulation, the higher local concentration in the trapping region increased the fraction of strands bound to each other, i.e. they increased the size of the linDNA strands or brDNA networks. As the accumulation was length-selective, larger complexes were accumulated better by the second trap in the x-z-plane, further increasing their local concentration and therefore the size of the networks. Eventually, this self-enhancing process triggered the formation of DNA hydrogels along the center of the capillary (Figure 2.5a), consistent with theory as described in Section 2.3.
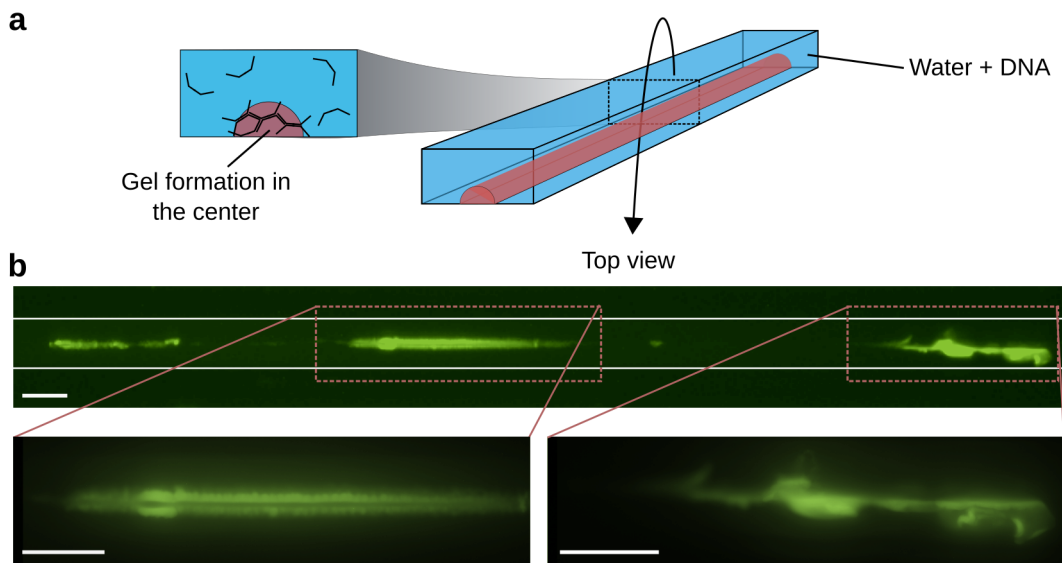

Figure 2.5: Gelation of a 36mer brDNA. (a) The accumulation of self-complementary DNA in the capillary led to the formation of larger complexes and eventually DNA hydrogels. The gels were found along the center of the capillary in the accumulation region (red marked area), consistent with the theory that the trap in the x-z plane accumulates larger complexes better in the center (see Figure 2.3). **(b)** DNA hydrogels formed from a 36mer brDNA along the capillary after 167 minutes of accumulation (PBS buffer, $c_0 = 10$ μM). The gel formed only close to the center and not directly in it, as the laser that was driven horizontally along the capillary melted the gel. This produced a fine horizontal line in the center where no gel was found. White lines indicate edges of the capillary. Scale bars: 100 μm

Figure 2.5b shows the DNA gel formed from a 36mer brDNA in PBS buffer after 167 minutes of accumulation (initial concentration: 10 μM). After their formation, the gels were stable for several days and dissolved back into solution when the base temperature was increased above the melting temperature of the separate binding sites.

2.4.2 Gelation of Single Strands

In addition to the gelation of the 36mer brDNA, the gelation of shorter strands was explored. Figure 2.6 shows the formation of DNA hydrogels using a 30mer brDNA. Starting from a 100 µM concentration (1 min), no gel could initially be observed. DNA accumulated in the center of the capillary over time (42 minutes), reaching a critical concentration after around 80 minutes, after which the first gel spots formed. After 125 minutes, the spots had grown to a several hundred micrometer large gel. The gelation of a 24mer brDNA was tested under the same conditions (Figure 2.7). A gel again formed from a starting concentration of 100 µM after 100 minutes of accumulation. No gel was found for an 18mer brDNA strand.
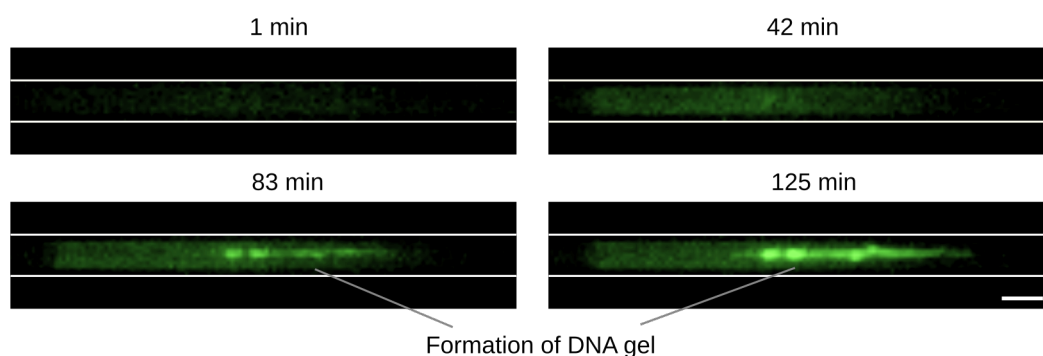

Figure 2.6: Gelation of a 30mer brDNA over time. After 80 minutes of accumulation ($c_0 = 100$ μM, PBS buffer) the DNA started to form a gel in the center of the capillary. Within 125 minutes it had grown to several hundred micrometer in length. White lines indicate edges of the capillary. Scale bar: 100 µm
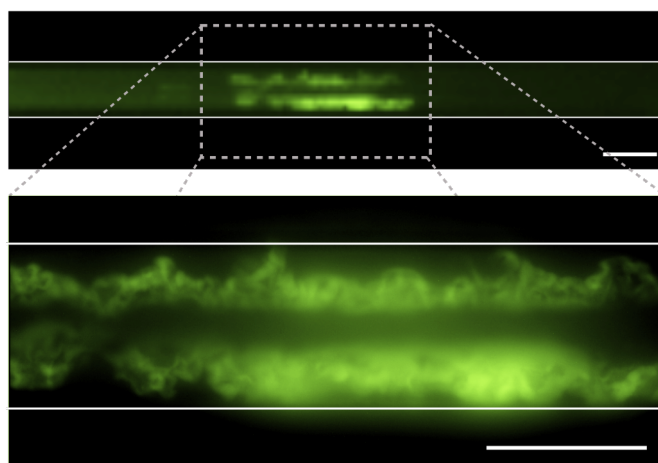

Figure 2.7: Gel from a 24mer brDNA. A gel had formed after 100 minutes of accumulation ($c_0 = 100$ μM, PBS buffer). In the center, the horizontal path of the laser where the gel was melted can be seen. This is the shortest brDNA strand for which a gel-formation could be observed. White lines indicate edges of the capillary. Scale bars: 100 µm

As stated above, DNA can also form hydrogels when it has only two self-complementary binding sites. Figure 2.8a shows a linear, double stranded 125mer DNA that was accu-

mulated in the trap with a starting concentration of 2.5 μM. Similar to the brDNA, the linDNA formed a gel in the trap within 30-60 minutes after starting the accumulation. Its two single stranded components, linDNA and the complement $\overline{\text{linDNA}}$, each had a fluorescent dye attached to it, a FAM tag and a ROX tag, respectively.

To rule out the possibility that fluorescent tags were responsible for the gel formation, several control measurements were performed. First, linDNA without any fixed fluorescent tags was accumulated in the trap. Label-free strands were mixed with the intercalating dye SYBR Green I, a free dye that attaches to double stranded DNA. Figure 2.8b shows that this DNA also formed a DNA hydrogel, similar to the DNA with the attached fluorophores. As a second control, the same label-free linDNA was accumulated blindly, without SYBR Green I present (Figure 2.8c). To this end, the system was first calibrated with the fluorescent dye BCECF (2',7'-Bis-(2-Carboxyethyl)-5-(and-6)-Carboxyfluorescein) to ensure that the accumulation was working. Next, as the capillary was attached to a syringe system on one end, the solution inside the capillary could be exchanged with linDNA without touching it. After 1.5 hours of blind accumulation, a 10-fold concentrated solution of SYBR Green I in PBS buffer was slowly flushed into the system. As the DNA gel formed on the bottom of the capillary and was sticking to it, this was possible without damaging or flushing out the gel if flow speeds were low enough. After the buffer was exchanged, the dye attached to the hydrogel and was detected by fluorescence microscopy. This demonstrates that the hydrogel formation resulted solely from DNA-DNA interactions and not from interactions between the fluorescent tags.

Interestingly, when the buffer of the capillary shown in Figure 2.8a was exchanged with pure water, the hydrogel broke apart as the ions were removed from its surroundings, leaving behind rod-like gels of similar sizes (Figure 2.8d). One explanation for this could be that the strands in the hydrogel formed from linDNA align alongside each other inside the gel. When the buffer was exchanged, the ions inside the hydrogel remained, as they shielded the negatively charged DNA from each other and were therefore kept in place. Strands that were not perfectly aligned or stood out were, however, more likely to lose these ions and detach from the gel, resulting in the rod-like structures.

To show that the DNA hydrogel only forms from self-complementary DNA, linDNA with only one sticky end was accumulated (Figure 2.8e). This structure prevented the dsDNA strands from binding to each other. After 100 minutes, the DNA still accumulated in the center of the capillary, however no DNA gel was found.

Applying a large enough flow to the system allowed flushing the hydrogel out of the capillary. This gave the opportunity to analyze it further. To do so, the solution with the floating gel was flushed out of the open end of the capillary and into a small droplet of pure water on a glass slide. The droplet was then allowed to dry and subsequently imaged under fluorescent and scanning electron microscopy (SEM) (Figure 2.9). The resulting images show the DNA gel and its fibrous structure. This also demonstrates that the gel can withstand moderate shear forces.
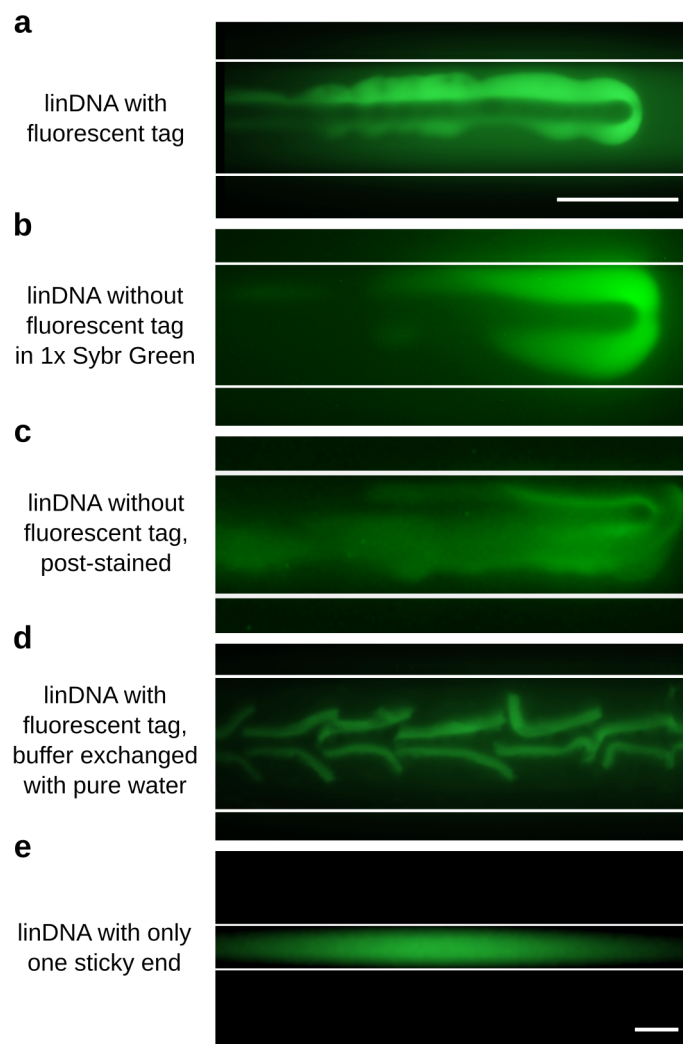
a linDNA with fluorescent tag

b linDNA without fluorescent tag in 1x Sybr Green

c linDNA without fluorescent tag, post-stained

d linDNA with fluorescent tag, buffer exchanged with pure water

e linDNA with only one sticky end

Figure 2.8: Gelation of linDNA and control measurements. (a) A hydrogel formed from linDNA after 50 minutes of accumulation (c_0 = 2.5 μM). **(b)** Control: Gel formed after 60 minutes from linDNA without attached fluorescent tags, but with free SYBR Green I dye in the buffer (c_0 = 5 μM) **(c)** DNA gel formed after 1.5 hrs of blind accumulation. No fluorescent dye was present during the accumulation. After the experiment, 10-fold concentrated SYBR Green I dye was flushed in the system, which post-stained the gel. **(d)** The same gel from (a) after the buffer was exchanged with pure water. The DNA gel separated into several rod-like compartments. **(e)** linDNA with only one sticky end after 100 minutes of accumulation (c_0 = 5 μM). Here, no gel was found. White lines indicate edges of the capillary. Scale bars: 100 µm
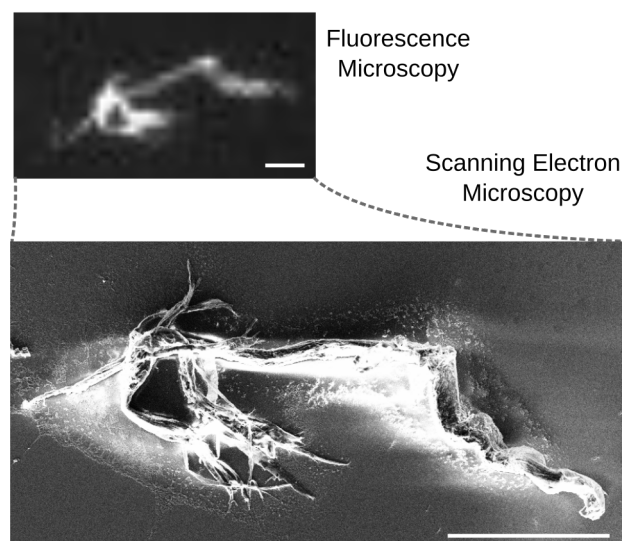
Figure 2.9: Image of a DNA hydrogel under a scanning electron microscope. The top image shows a gel extracted from the capillary under fluorescence microscopy. The SEM image (bottom) exhibits a similar structure. On its left side, the fibrous nature of the gel can be seen. Scale bars: 100 μm.

2.4.3 Selective Gelation

In addition to the gelation of one 36mer brDNA in solution, a competition between two 36mer brDNA strands with different, orthogonal sequences was probed. To this end, a second brDNA strand (brDNA-2) was designed that had minimal base-complementarity with the previously used strand, despite also consisting only of the bases G and C. The hybridization energies between its self-complementary binding sites were approximately 32 kcal/mole, similar to brDNA, however only up to 20 kcal/mole for bonds between brDNA and brDNA-2 bases. The two strands were labeled with different fluorescent tags to be able to distinguish them under a fluorescence microscope. As a first control measurement, two of the same 36mer strands, $brDNA_{Cy5}$ (red) and $brDNA_{FAM}$ (green) with the same sequence but different fluorescent labels were accumulated in the chamber (Figure 2.10a). Within 60 minutes, both strands were concentrated in the center of the capillary and formed a DNA hydrogel. As they had the same sequence, they formed the same gel and could not be distinguished when examining them separately. The gels in the two color channels fully overlapped.

Figure 2.10b shows what happened when $brDNA_{FAM}$ was exchanged with the still self-complementary, but not to brDNA complementary, brDNA-2$_{FAM}$. After starting the accumulation of these two strands, $brDNA_{Cy5}$ started to form a DNA hydrogel within 30 minutes. This gel was only observed in the red color channel, up to this point the green colored brDNA-2$_{FAM}$ did not form a gel. This could have been due to $brDNA_{Cy5}$'s slightly higher binding energies or small variations in the initial concentration from pipetting errors. However, after 60 minutes also brDNA-2$_{FAM}$ started forming a hydrogel (green). It can be seen that it initially grew in the center of the capillary and moved outward over time (white arrows indicate direction). The two DNA strands therefore

unmixed and formed separate hydrogels. Within the next 30 minutes, brDNA-2$_{FAM}$'s gel had almost completely replaced the red-colored gel, which was pushed further outwards and partially melted in the center of the capillary. After 120 minutes, however, the red brDNA$_{Cy5}$ could be seen to start forming a gel in the center again. The single-channel images at this time point (Figure 2.10b, bottom) show that the two gels did not overlap and were sequence-pure.
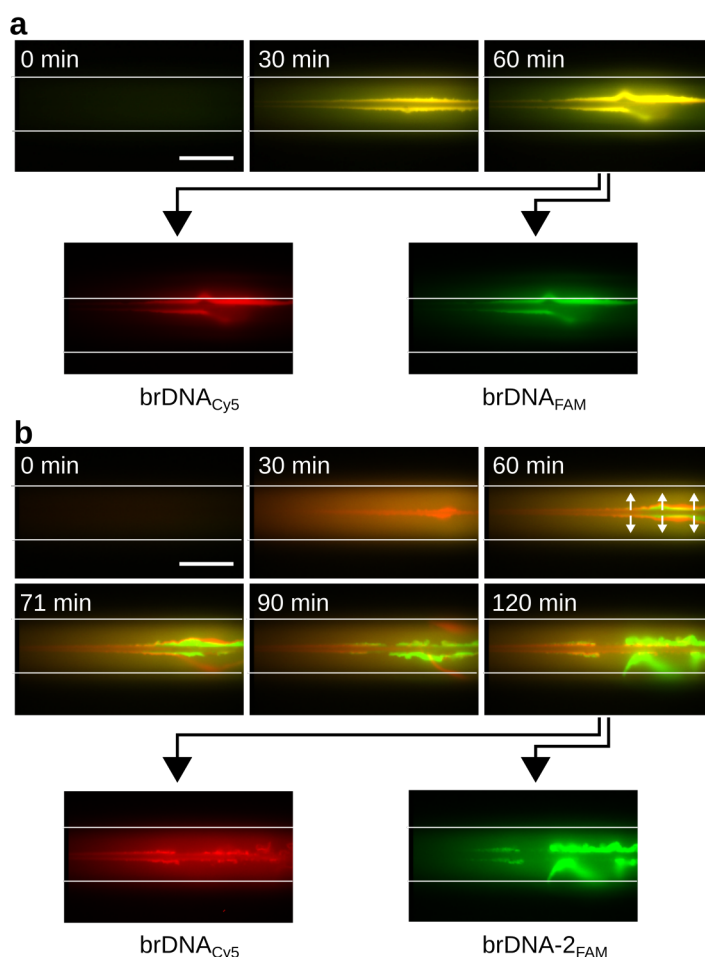

Figure 2.10: Selective Gelation of brDNA. (a) Control experiment using two 36mer brDNA with the same sequence but two different fluorescent labels (Cy5 and FAM in red and green, respectively). The gels that formed after 60 minutes completely overlapped when comparing the two color channels. This shows that, despite the different labels, the two strands formed the same DNA hydrogel as they had the same sequence. **(b)** Competitive gelation of the two orthogonal strands brDNA$_{Cy5}$ and brDNA-2$_{FAM}$. Initially, brDNA$_{Cy5}$ (red) formed a hydrogel in the center of the capillary after 30 minutes of accumulation. However, after 60 minutes, also brDNA-2$_{FAM}$ (green) started forming a gel in the center (white arrows), pushing the red gel aside (71 and 90 minutes). After 120 minutes, the red-colored brDNA$_{Cy5}$ again formed a gel in the center of the capillary. A comparison of both color channels shows that the gels formed here were sequence-pure. White lines indicate edges of the capillary. Scale bars: 100 µm.

2.5 Discussion and Conclusion

The experiments demonstrate that self-complementary DNA can form macroscopic, millimeter-sized hydrogels when it is locally accumulated. Gels were formed from strands with two or more self-complementary binding sites. Such sol-gel phase transitions normally require the presence of condensing agents [25, 26, 29] or neutral polymers [30, 31], especially in the absence of multivalent ions. Here, no condensing agents or multivalent ions were used. Instead, the self-enhancing accumulation mechanism, which concentrates molecules better the larger they become, triggered the formation of the DNA hydrogels from strands as short as 24mers. The process also took place in the absence of fluorescent dyes and only depends on the sequence of the DNA. Once formed, the hydrogels were stable for days and, for a short time, even survived a drastic reduction in salt concentration of the surrounding buffer solution. Due to its similar thermophoretic behavior, RNA is expected to behave similarly (see also Chapter 3).

The formation of hydrogels is also interesting from an origin of life perspective. The accumulation and gelation process is driven by purely physical mechanisms and could take place for example in porous rock heated by hydrothermal or volcanic activity. In such a setting, strands of similar sequence could bind to each other and form a gel inside these pores from an initially random pool of oligonucleotides. This could be a first mechanism to reduce the large sequence space and promote self-complementarity. Especially in the case of RNA the gel state could protect the nucleic acids from hydrolysis [49] and dilution, and allow them to survive sudden changes in external buffer conditions. Strands with different sequences were shown to be separated into sequence-pure hydrogels by purely physical means, providing a further selection mechanism. Due to the high local concentrations inside the gels, this process could then enhance the catalytic activity of for example ribozymes [28] as the hydrogels are likely still accessible to small oligonucleotides by diffusion.

The results give an overview over the requirements to form DNA hydrogels and the mechanisms behind it. In further experiments, the sequence selectivity of the brDNA gelation by thermal accumulation was explored in detail. They showed that by changing a single base in the sequence of brDNA it could be separated from the original strand; the first remained in solution, the latter formed a gel. In addition, the experiments showed that changing one base-pair per self-complementary site was enough to form separate, sequence-pure hydrogels. These results were published in *Angewandte Chemie International Edition* under the title "Heat-Flow-Driven Oligonucleotide Gelation Separates Single-Base Differences". The publication is given in Appendix A.

2.6 Materials and Methods

The Sequences of the here used DNA were:
36mer brDNA: 5'- GCGGGCGCCCGC-CGCGGCGCCGCG-GGCCGCGCGGCC - 3'
36mer brDNA-2: 5'- GGCGCGCGCGCC-CGGGCCGGCCCG-CCCGCCGGCGGG - 3'
30mer brDNA: 5' - GGCGGCCGCC-GCGGGCCCGC-CGCCCGGGCG - 3'
24mer brDNA: 5' - GCGGCCGC-CGGGCCCG-CCCGCGGG - 3'
linDNA: 5' - GTTATTGCAC(FAM) - TGCATGTAGC - CCTGAACACT - CTGGGGGCCC - AGTGACTACT - CCTCCTCGAC - GCCTGAGGGC - ACTTGGTCTT - GAGAGCCCCT - TAGGTAGTTG - AACCGGCCAT - TCCCCAGGGC - 3'
linDNA: 3' - TGTGAGACCC - CCGGGTCACT - GATGAGGAGG - AGCTGCGGAC - TCCCGTGAAC - CAGAACTCTC - GGGGAATCCA - TCAACTTGGC - CGGTAAGGGG - TCCCGCAATA - ACGTG(ROX)ACGTA - CATCGGGACT - 5'

All DNA strands were bought from Biomers (Ulm, Germany), experiments were performed in PBS buffer (137 mM NaCl, 2.7 mM KCl, 10 mM $Na_2HPO_4 \cdot H_2O$, 2 mM KH_2PO_4) if not stated otherwise.

Accumulation chambers were built by gluing a custom-made borosilicate capillary (VitroCom, Mountain Lakes, NJ; with a rectangular cross section of 100 μm x 50 μm) onto an approx. 2 cm x 1 cm large silicon wafer. The capillaries were lying so that the 100 μm long side was facing downwards/upwards. As a glue, two drops of a two component epoxy glue were placed on each edge of the capillary. On one side the capillary was connected to a high precision syringe pump (neMESYS, cetoni) using polyethylene tubings. In the accumulation area it was topped with immersion oil (Zeiss) and a sapphire window.

Temperature and laser calibrations were performed as follows: A capillary was filled with 50 μM BCECF (2',7'-Bis-(2-Carboxyethyl)-5-(and-6)-Carboxyfluorescein) in 10 mM TRIS buffer. As the fluorescence of BCECF depended on the pH, and the pH of TRIS was temperature dependent, this could be used to track the temperature of the capillary *via* the fluorescence of BCECF. First, the capillary was filled with BCECF and the system cooled to 10 °C. Then, the fluorescence of the BCECF was recorded as the base temperature of the capillary was slowly increased to approx. 90 °C using the Peltier device. The laser (TLR-20-1940, IPG Photonics) was turned off during this time. As a next step, the capillary was again cooled down to 10 °C, the operation temperature in all experiments. The laser intensity was then set to a minimum and turned on together with the mirror system (6200-XY, Cambridge Technology). In order to reduce changes in fluorescence due to a thermophoresis of BCECF, images of the fluorescence were taken very quickly (within 200 ms) after turning on the laser. Next, the laser intensity was increased and the procedure repeated several times. From these two measurements, the mean temperature of the trap could be determined with respect to the laser intensity.

Scanning Electron Microscopy was performed using a Zeiss Ultra-55 Scanning Electron Microscope. SYBR Green I was obtained from Thermofischer.

3

Accumulation of Molecules at Gas-Water Interfaces in a Thermal Gradient

3.1 Summary

Non-equilibrium conditions must have been crucial for the assembly of the first informational polymers of early life by supporting their formation and continuous enrichment in a long-lasting environment. The results presented in this chapter explore how gas bubbles subjected to a thermal gradient in water, a likely scenario inside rocks on early Earth [15, 50], drive a complex, continuous enrichment of prebiotic molecules. Monomers, oligonucleotides, ribozymes, lipids, and RNA precursors are shown to (1) cycle between dry and wet states, enabling the central step of RNA phosphorylation, (2) accumulate at the interface, increasing their catalytic activity, (3) condense into hydrogels, (4) form pure crystals, and (5) encapsulate into vesicle aggregates that protect their content and subsequently undergo fission. These effects occur within less than 30 minutes. The findings unite physical conditions into one location that have been demonstrated to be crucial for the chemical emergence of biopolymers. They suggest that microbubbles could have hosted the first cycles of molecular evolution.
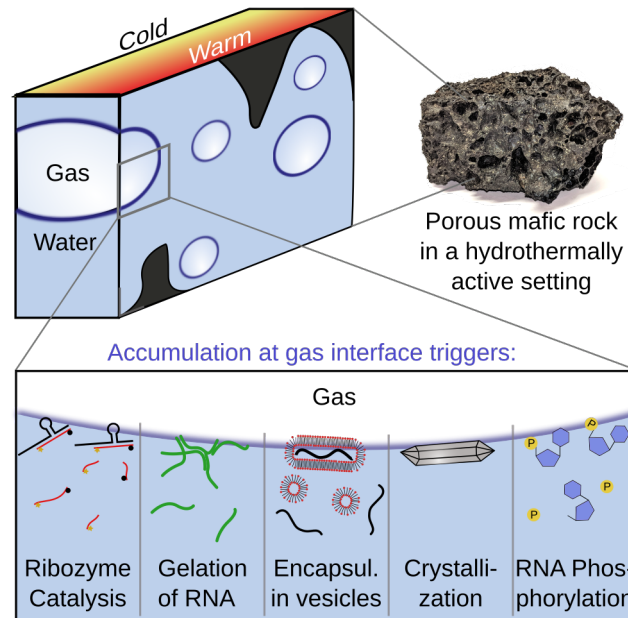
3.2 Introduction

Figure 3.1: DNA accumulation at gas bubbles in a thermal gradient. Hot porous volcanic rock hosts water in pore spaces of both primary (magmatic vesicles) and secondary (fractures) origin. Microbubbles in this system lead to an accumulation of molecules at the warmer side of the gas-water interfaces. As shown experimentally, this environment can trigger the increased catalysis of ribozymes, the formation of a hydrogel from self-complementary RNA, the encapsulation of oligonucleotides in vesicle aggregates and their subsequent fission, the crystallization of ribose aminooxazoline (RAO)—a prebiotic RNA precursor—or initiate the phosphorylation of RNA nucleosides.

Diverse locations for the origins of life have been studied. Based on entropic arguments, near-equilibrium conditions were unlikely to trigger evolutionary processes [4]. In contrast, non-equilibrium systems can locally reduce entropy, give rise to patterns [51], and lean the system towards a continuous, dynamic self-organization [52]. Non-equilibrium dynamics can be found in wide range of fluid systems, including gravity-driven instabilities in the atmosphere [53], the accumulation of particles in nonlinear flow [54] [55], and shear-dependent platelet activation in blood [56]. The experiments shown here demonstrate that the interplay between prebiotic molecules and a non-equilibrium environment near microscopically small gas bubbles drives a wide range of processes that have been discussed in context with the emergence of life.

On the warm, early Earth, non-equilibrium systems in the form of heat flows were a very common and simplistic setting, found ubiquitously on the planet [50]. Temperature gradients would have occurred in natural fluid systems and were created, for example, by the flow of warm water in hydrothermal vents or by hot vapor across porous volcanic rocks [15, 57] (Figure 3.1). They have been studied as non-equilibrium driving forces for biological molecules in a variety of processes [12, 19–23, 44, 48].

At the same time, heated systems promote the formation of gas bubbles due to outgassing from liquids. The bubbles create gas-water interfaces, which previously have been discussed in connection with atmospheric bubble-aerosol-droplet cycles [58], the

adsorption of lipid monolayers and DNA to the interface [59, 60], or the formation of peptide bonds [61].

In the absence of a temperature gradient, the evaporation of a drop of water on a surface exhibits the so-called "coffee-ring effect" [62]. Upon the evaporation, molecules dissolved in the drop are accumulated at its rim by a resulting capillary flow. After complete evaporation, a ring of concentrated material is deposited. In the inverted setting studied here, where a gas bubble is immersed in water (Figure 3.1), a temperature gradient drives this process continuously.

3.3 Results

3.3.1 Accumulation at Gas-Water Interfaces

The accumulation of molecules at heated gas-water interfaces is caused by a continuous evaporation-recondensation cycle of water. The interfaces were held in a constant non-equilibrium state, leading to a steady state coffee-ring effect that does not end in a fully dry state. Here, six physico-chemical processes were observed, which have all individually been suggested to be relevant for the emergence of prebiotic evolution and are co-located in a single non-equilibrium system: (i) accumulation of ribozymes and their increased catalytic activity, (ii) condensation of self-complementary RNA 36mers into millimeter-sized hydrogels, (iii) vesicle aggregation at the bubble interface along with encapsulation of oligonucleotides with up to 18-fold enhanced concentration, (iv) fission of the vesicle structures in the adjacent micro-convection, (v) formation of euhedral 300 μm crystals from the RNA precursor sugar ribose aminooxazoline (RAO) around bubbles, which also act as seeds for new bubbles, and (vi) dry-wet cycles enhancing for example the phosphorylation of nucleosides, created by fluctuating and moving interfaces (Figure 3.1). All six mechanisms were established within 30 minutes and, importantly, operated in continuous contact with bulk water under physiological buffer conditions.

In this part, the capillary from Chapter 2 was replaced with a 240 μm thick microfluidic chamber that allowed a better control over the mimicked pore structure. Fluorescently labeled molecules were flown into a corrugated geometry that spontaneously formed gas pockets and generated several well-defined gas-water interfaces (Figure 3.2a). They were monitored through the warm side using a fluorescence microscope. The optical axis runs along the temperature gradient (Figure 3.2b) and the fluorescence was captured with a CCD camera. The front- and back-sides of the chamber were heated and cooled, respectively, to generate a temperature gradient (Figure 3.3).

Initially, the chamber was filled with a solution of 200 nM FAM labeled 132 base single-stranded DNA (ssDNA) oligomer in 0.1-fold PBS buffer (1-fold PBS buffer: 137 mM NaCl, 2.7 mM KCl, 10 mM phosphate buffer). When no temperature gradient was applied to the system ($T_{warm} = T_{cold} = 10$ °C), DNA did not accumulate near the gas-water interface. The fluorescence signal exhibited a constant small peak at the observed interface, possibly due to a slight surface adsorption of the DNA to the gas-water interface (Figure 3.4a(i), 0 s). Heating one side of the chamber ($T_{warm} = 30$ °C, $T_{cold} = 10$ °C) resulted in the rapid accumulation of DNA in a small area on the warm side at the contact line (Figure 3.4a(ii), dashed red box). The chamber-averaged fluorescence at the contact line increased within six minutes approximately 12-fold compared to the bulk fluorescence (Figure 3.4b). It did not matter for the accumulation whether the bubble was at the top, as shown in most experiments here, or at the bottom of the chamber. No accumulation was observed on the cold side.

The local concentration at the contact line was calculated from the ratio of the meniscus- and bulk-fluorescence and the geometry of the curved gas-water interface. Since the fluorescence was averaged over the chamber by the long distance objectives, a 60-fold higher concentration in addition to the higher fluorescence is inferred due to the thinner size of the accumulation region (approximately 4 μm) as compared to the 240 μm wide
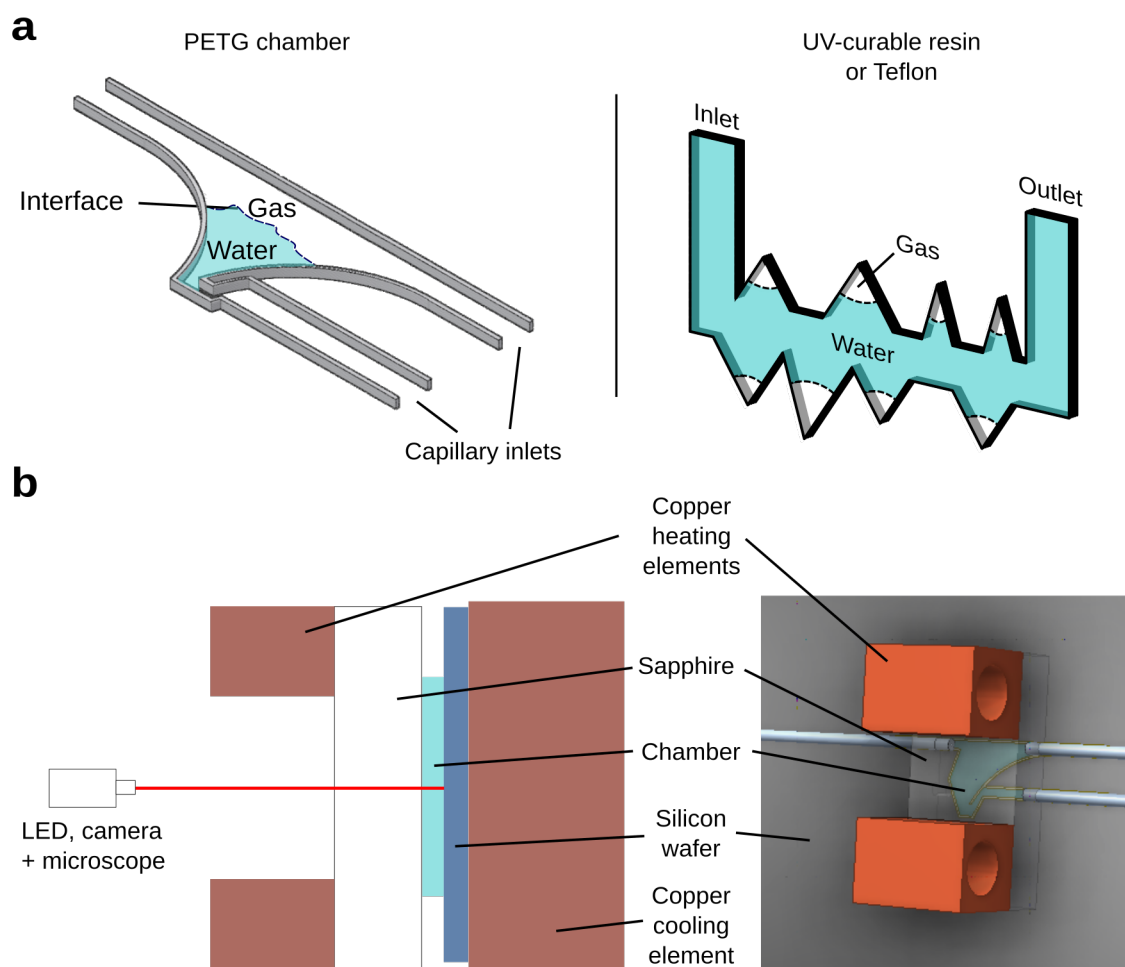
Figure 3.2: Chamber Setup. (a) Diagram of the microfluidic chamber. Chamber walls were made of PETG plastic (for experiments in Figure 3.4), UV-curable resin (most experiments), or Teflon foil (Hammerhead and phosphorylation experiments), creating e.g. a funnel-like profile that enables easy creation of a gas-water interface. The thickness of the chamber was 240 μm if not stated otherwise, and was set by the thickness of the capillary inlets (PETG chamber), by calibrated spacers (resin chamber), or the thickness of the Teflon foil. **(b)** Diagram of the experimental setup. The temperature gradient was produced by heating and cooling the sapphire and silicon substrate, respectively, effectively creating constant temperature boundaries on the walls of the chamber. The fluorescence microscope pointed through the transparent sapphire. The solution was excited with an LED, a CCD camera captured the fluorescence signal.

chamber. The observed 12-fold increase in fluorescence therefore inferred a concentration increase by a factor of 700, corresponding to 140 μM DNA concentration in the meniscus when starting from a 200 nM bulk solution (Figure 3.4c).

Further analysis from experiment and theory showed that the accumulation was caused by the focused evaporation of water at the tip of the meniscus [62] (Figure 3.4d, orange). A continuous flow of water into the meniscus dragged the molecules with it, which, since they could not evaporate, could only escape against the one-way capillary flow by diffusion. The flow was visualized by filling the chamber with a suspension of 200 nm
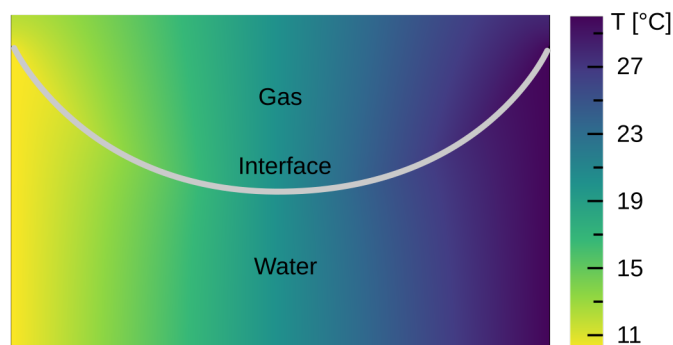
Figure 3.3: Simulation of temperature gradient. Temperature profile with 30 °C on the right and 10 °C on the left. The profile is linear in the bulk gas and water regions. Along the interface, it is slightly deformed, but can still be approximated as linear.

diameter FAM-labeled polystyrene beads. Using particle tracking the velocity profile in the meniscus was measured (Figures 3.4d,e). Beads moved towards the accumulation region near the hot side of the chamber at the contact line. A comparison of the bead speeds over the last few seconds before they reached their endpoints (Figure 3.5) with the simulation shows that the latter gives only slightly higher average values.

The flows towards the meniscus are assumed to be capillary flows, which superseded the comparatively weak bulk buoyant convection (Figure 3.4e). In addition, evidence for Marangoni flow was found in the form of strong lateral flows close to the interface, driven by the difference in water surface tension at the interface in a temperature gradient [63] (Figure 3.4d, green).

The water that evaporated near the warm chamber wall was found to condense on the cold wall, forming small water droplets. As a result, the gas bubble had less space, expanded, and moved the gas-water interface. Once the condensed droplets had grown, they merged and eventually re-entered into the bulk solution, driven by surface tension. Subsequently the interface moved back to its initial position. These fluctuations of the contact line triggered a drying and recondensation of the molecules at the very location where the capillary flow initially accumulated them.

A fluid dynamics model described the main features of the accumulation by considering a 2D section perpendicular to the interface. Since the width of the channel was smaller than the capillary length for water and gas [64], the interface geometry was approximated by an arc of a circle. The contact line of the interface was pinned in the simulation [65] [66], motivated by the observation that the accumulation kinetics was generally faster than the fluctuating movement of the interface.

The model superposed four water flows that provide the boundary condition for the accumulation of DNA. They were (i) the capillary flow at the meniscus, (ii) the diffusion of water vapor between the interface and the gas bubble, (iii) the convection of water, and (iv) the Marangoni flow along the interface. The relative strength of the Marangoni flow— a free parameter due to the unknown presence of surface-active molecules [67]—was adjusted to fit the velocities measured in the experiment.

The interplay of all four flows led to the accumulation of molecules at the meniscus. As only water evaporated on the warm side, dissolved molecules were continuously dragged
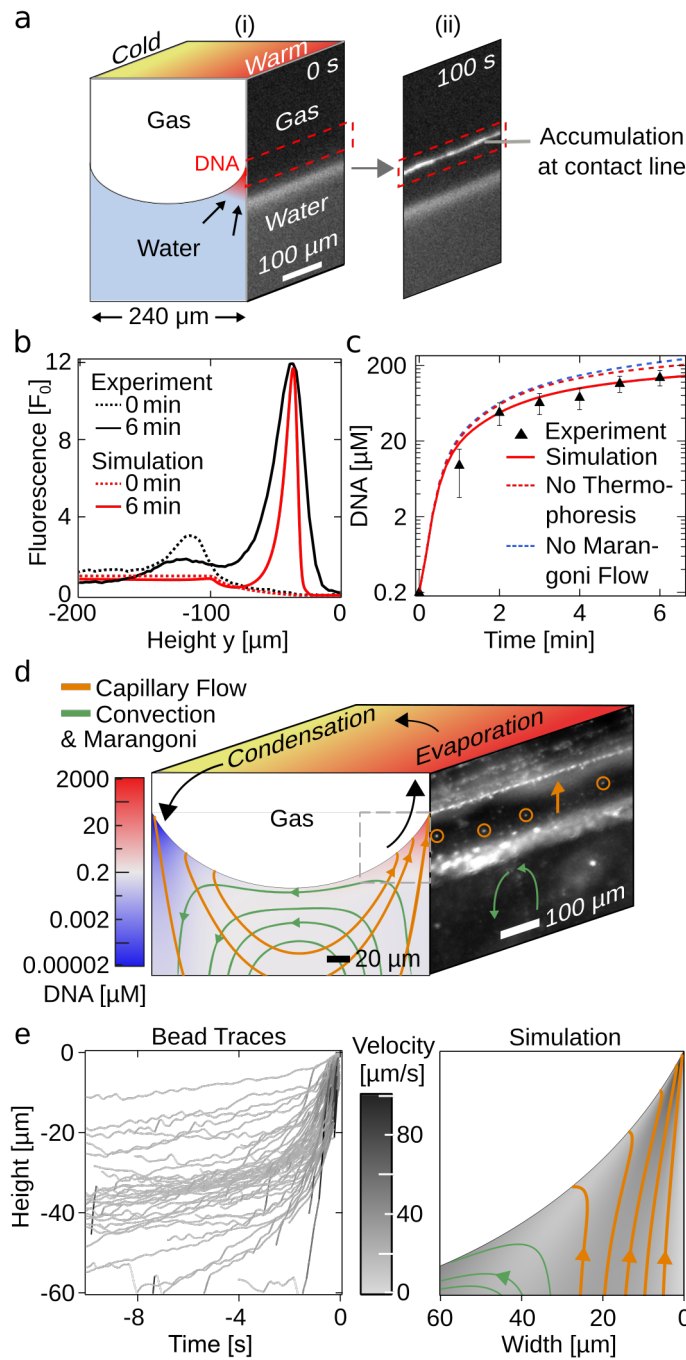
Figure 3.4: DNA accumulation by capillary flow. (a) (i) Gas-water interface in the chamber with images from fluorescence microscopy. (ii) 132mer DNA in water accumulated near the contact line at the warm temperature side (T_{cold} = 10 °C, T_{warm} = 30 °C). **(b)** The fluorescence profile reached a 12-fold increase as compared to the bulk fluorescence within six minutes. **(c)** Due to the confined meniscus geometry, the accumulated concentration was significantly higher. The 12-fold increase in fluorescence corresponded to a 700-fold increase in DNA concentration at the meniscus, consistent with simulation results (red lines). In the absence of thermophoresis (red interrupted line) or Maranogi flows (blue interrupted line) the simulation predicts a slightly higher accumulation. Error bars were estimated from fluorescence analysis at several positions along the contact line. **(d)** Fluid flow near the contact line measured by single particle tracking. The capillary flow (orange) pulled the beads upwards toward the contact line as water mainly evaporated at the tip of the meniscus. Marangoni- and convection flows (green) shuttled the beads between hot and cold side. Superposed is the logarithmic concentration profile obtained from the simulation for the accumulation in (a). **(e)** Single-particle tracking and simulation of the capillary flow. Peak flow velocities reached 50 µm/s in the last second of the water flow before its evaporation (Figure 3.5). Here T_{cold} = 10 °C, T_{warm} = 40 °C.

towards the contact line, where their concentration depended on their back-diffusion and the speed of the capillary flow. Convection and Marangoni flow provided a constant cycling of water and new material towards the accumulation region. In the absence of thermophoresis or Marangoni flows, the model predicts a slightly higher accumulation (Figure 3.4c).

The DNA accumulation was experimentally measured for various temperature differences and DNA lengths (Figures 3.6a,b). It rises with increasing temperature difference (ΔT), reaching a 4000-fold increase for ΔT = 40 °C. Also, smaller (15mer) DNA accumulated three times less effective than larger (132mer) DNA, which was attributed to their higher diffusion coefficient. The model predicts a multi-fold accumulation of mono- and divalent ions (Figure 3.6c), resulting in a higher salt concentration at the meniscus.
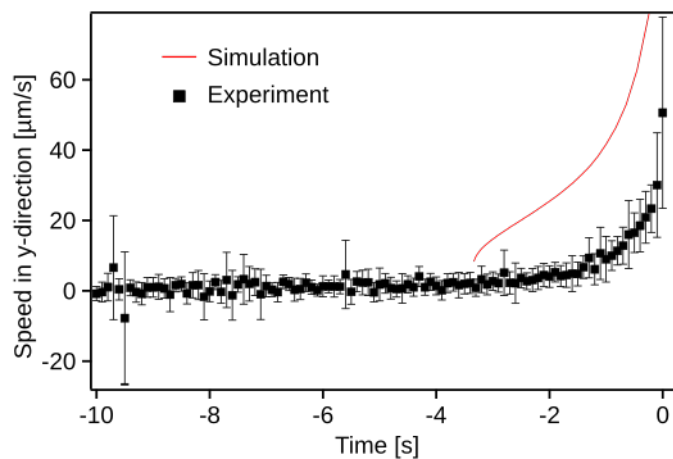

Figure 3.5: Bead Analysis. Velocities of beads in y-direction, perpendicular to the contact line, 10 seconds before reaching the interface. Error bars are standard deviations. Simulation results are shown in red. They were determined by calculating the average y-speed of the flow in 2 µm intervals away from the contact line and then integrated over that distance.
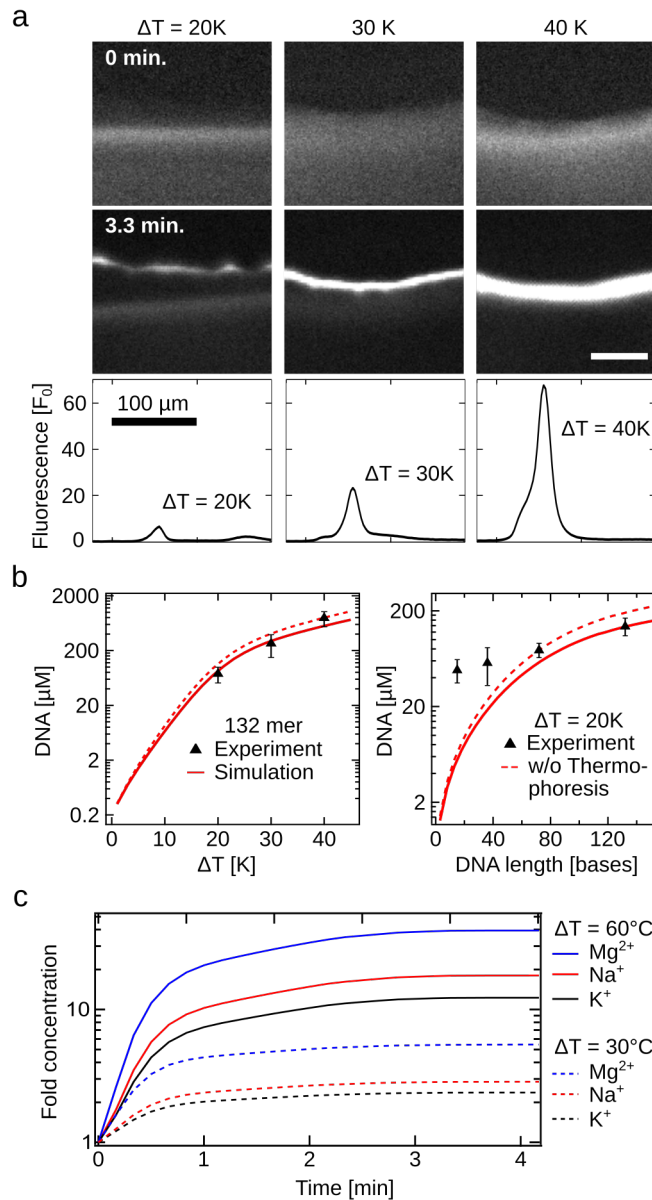
Figure 3.6: Size and temperature dependence of accumulation. **(a)** Dependence on temperature difference. The interfaces initially showed no significant accumulation of 132mer DNA with $T_{cold} = T_{warm} = 10\,°C$. After 3.3 minutes of heating the warm side to T_{warm}, a marked dependence of the fluorescence profiles on the applied warm temperature was found, reaching a more than 60-fold increase for $T_{warm} = 50\,°C$, i.e. a temperature difference of 40 °C. This amounted to a 4000-fold accumulation. Scale bar: 100 μm. **(b)** The simulation (red line) predicted the accumulation with good accuracy over time, temperature, and DNA length. DNA between 15 and 132 bases in a 20 °C temperature difference was probed over the course of six minutes per strand. The smallest strand accumulated about threefold less than the largest DNA. Interestingly, the simulation predicted a significantly lower accumulation for short DNA. Thermophoresis did not contribute to the accumulation mechanism significantly and its omission would slightly increase the accumulation (broken line). **(c)** The simulation predicted an accumulation of salt molecules by at least one order of magnitude for T_{warm} and T_{cold} at 70 °C and 10 °C, respectively. The accumulation still reached a factor of two to five for a lower temperature difference. Caused by its comparatively small diffusion coefficient, Mg^{2+} accumulated the strongest. Concentrations are given in units of their initial concentration.
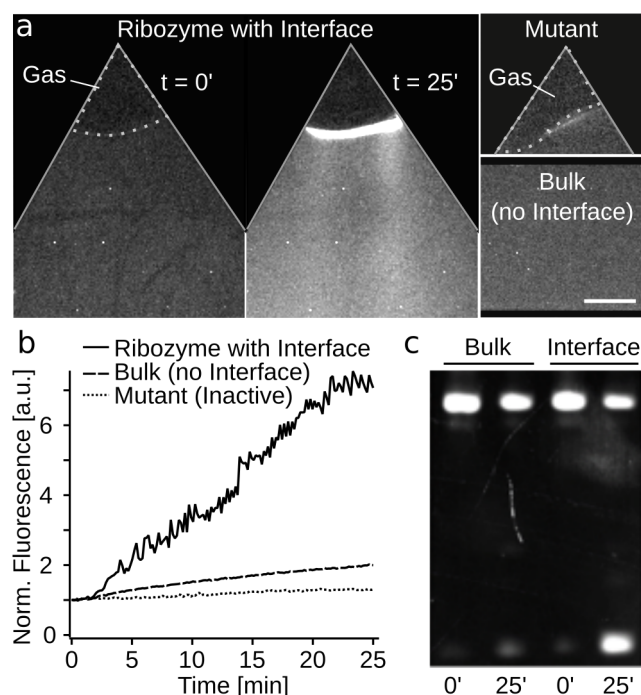
3.3.2 Ribozyme Catalysis

Figure 3.7: Ribozyme catalysis triggered by interface. Fluorescence microscopy and PAGE analysis of Hammerhead ribozyme activity. **(a)** Hammerhead in a chamber with gas-water interface at 0 and 25 minutes (left and right, respectively, T_{warm} = 40 °C, T_{cold} = 10 °C, 0.1 µM Ribozyme, 0.5 µM Substrate, 0.4 mM MgCl$_2$). The fluorescence increased strongly at the interface over time. Without interface (bottom right), the Hammerhead shows little activity; an inactive mutant (top right) showed no significant increase in fluorescence. Scale bar: 500 µm. **(b)** Overall fluorescence in the chambers from (a) over time. **(c)** PAGE analysis with and without interface after 25 minutes (Figure 3.8 for all measurements). A significant increase in cleaved product with the interface (35 % ± 13 %, five measurements) compared to bulk samples in the same temperature gradient (3.79 % ± 0.35 %, three measurements) was found.

The accumulation of larger biomolecules as well as ions at the interface makes it a powerful mechanism to enhance the activity of functional nucleic acids. To test this, the activity of the Hammerhead ribozyme [27, 68], which cleaves a 12mer RNA substrate strand, was monitored. The substrate and magnesium concentration [69] determined its activity, and both were accumulated in a 30 °C gradient (T_{warm} = 10 °C, T_{cold} = 40 °C) at low bulk concentrations (0.1 µM Hammerhead, 0.5 µM Substrate, 0.4 mM MgCl$_2$, Figure 3.7a). As a control, chambers without gas interfaces were studied. A FAM dye and a black hole quencher were attached on opposite sides of the substrate, inhibiting the fluorescence of the FAM dye. Upon cleavage, the dye was not quenched anymore and it could be detected by fluorescence microscopy.

Figures 3.7a,b show the average fluorescence in the chamber over time. The substrate strands were cleaved predominantly in the accumulation region, as seen by the rise of fluorescence (solid line). Due to the movement of the interface, they were frequently ejected into the bulk solution. After 25 minutes, samples were extracted and analyzed by polyacrylamide gel electrophoresis (PAGE, Figure 3.7c, Figure 3.8, Table 3.1). The analysis shows that up to 50 % of the substrate was cleaved in a chamber with bubbles. In the

same temperature gradient, but without interfaces (interrupted line), only 3.8 % of the substrate was cleaved.

When using an inactive mutant version of the ribozyme, the fluorescence did not noticeably increase (Figure 3.7a, top right, Figure 3.7b, dotted line), demonstrating that it did not originate from an enhanced hydrolysis at the interface. This shows that the accumulation mechanism can enhance the catalytic activity of ribozymes, while maintaining low salt conditions in the bulk solution. It increases the turnover, i.e. the number of strands cleaved per ribozyme, by the accumulation of substrates and ions.
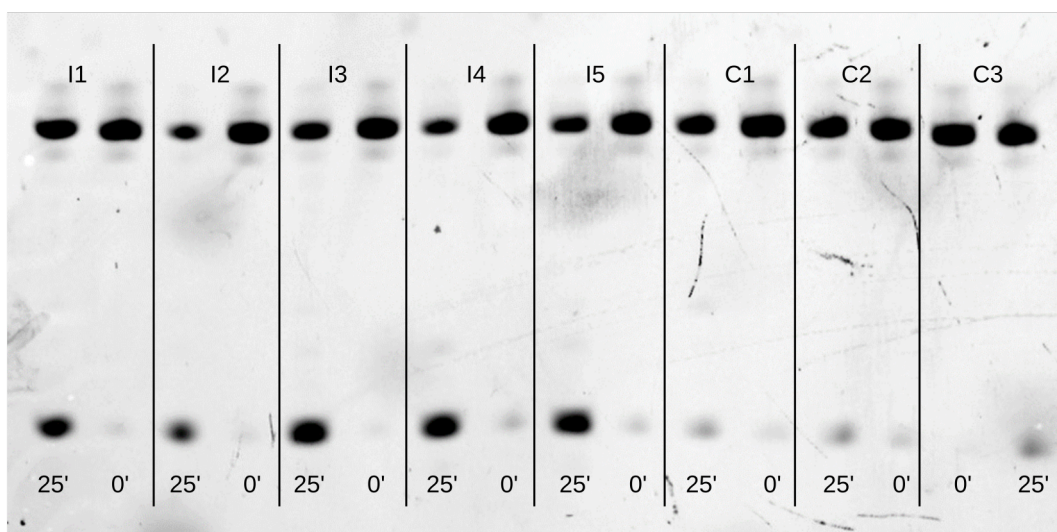
Figure 3.8: Polyacrylamide gel electrophoresis (PAGE) analysis of extracted ribozyme experiments. Measurements were performed as described in Figure 3.7. Lanes marked "I" were experiments with interfaces, lanes marked "C" were control experiments in the same temperature gradient but without bubbles in the chamber. An analysis of the yields is given in Table 3.1

#	% cleaved (0 min)	% cleaved (25 min)
I1	0.19	15.04
I2	0.17	31.05
I3	0.01	37.97
I4	0.48	50.3
I5	0.51	40.85
C1	0.12	3.9
C2	0.27	3.4
C3	0.4	4.07

Table 3.1: PAGE evaluation of extracted material from Figure 3.8. Experiments with Interface ("I") on average yielded 35 % ± 13 %, without interface ("C") only 3.79 % ± 0.35 %.

3.3.3 RNA and DNA Gelation

Figure 3.9: Sequence selective gelation of RNA and DNA. Fluorescence microscopy of DNA and RNA revealed the formation of hydrogels at the interface. **(a)** Gelation of DNA. (i) Before applying the temperature gradient, DNA accumulated at the interface only due to slight surface adsorption. (ii) After applying the temperature gradient, a DNA hydrogel formed and detached from the interface. (iii) At $T_{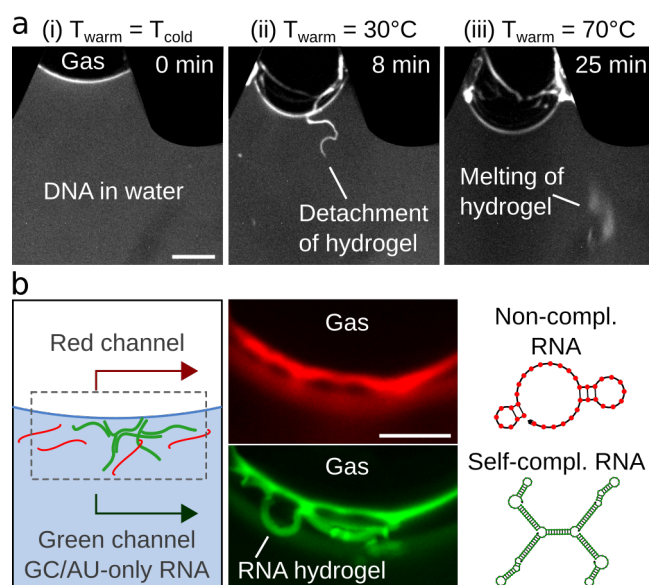warm}$ = 70 °C, the gel melted and redistributed the DNA back into the bulk fluid. The DNA concentration in the gel is estimated to be 100 µM. Scale bar: 500 µm. (b) Gelation of RNA. In a single experiment, non-complementary 36mer ssRNA (red) was accumulated with self-complementary 36mer ssRNA (green). Both strands accumulated at the interface (T_{warm} =30 °C, T_{cold} = 10 °C), however only the self-complementary RNA formed an elongated, fibrous hydrogel. The same behavior was found for DNA (Figure 3.10). Scale bar: 250 µm.

The length-selectivity observed in nucleic acid accumulation can enhance the concentration of self-complementary oligonucleotides to the point that gel-forming concentrations are reached (Figure 3.9a). Indeed, self-complementary strands were found to form a macroscopic, millimeter-sized hydrogel, as described in Chapter 2. The formation of these gels was observed for both self-complementary DNA and RNA (Figure 3.9) and for GC-only (Figure 3.9b) and AU-only RNA (Figure 3.10a). All oligonucleotides were end-labeled and HPLC purified to minimize the presence of free dye in the experiments.

Starting from uniformly distributed DNA in bulk solution (Figure 3.9a(i), initial concentration 10 µM; PBS buffer), the DNA was quickly accumulated at the interface once the temperature gradient had been established. Within eight minutes, a hydrogel had formed, detached from the interface, and entrained in the convection flow (Figure 3.9a(ii)). The gel nature of the DNA was checked by increasing the temperature from 30 °C, below the melting point of the self-complementary sequences, to 70 °C, where the gel dissolved into the convection flow (Figure 3.9a(iii)).

The formation of hydrogels from self-complementary RNA was also observed. Here, two different sequences were co-accumulated in a 20 °C temperature difference (Figure 3.9b, Figure 3.10a). The red fluorescence channel monitored a 36mer non-complementary ssRNA strand, the green fluorescence channel a self-complementary ssRNA strand.
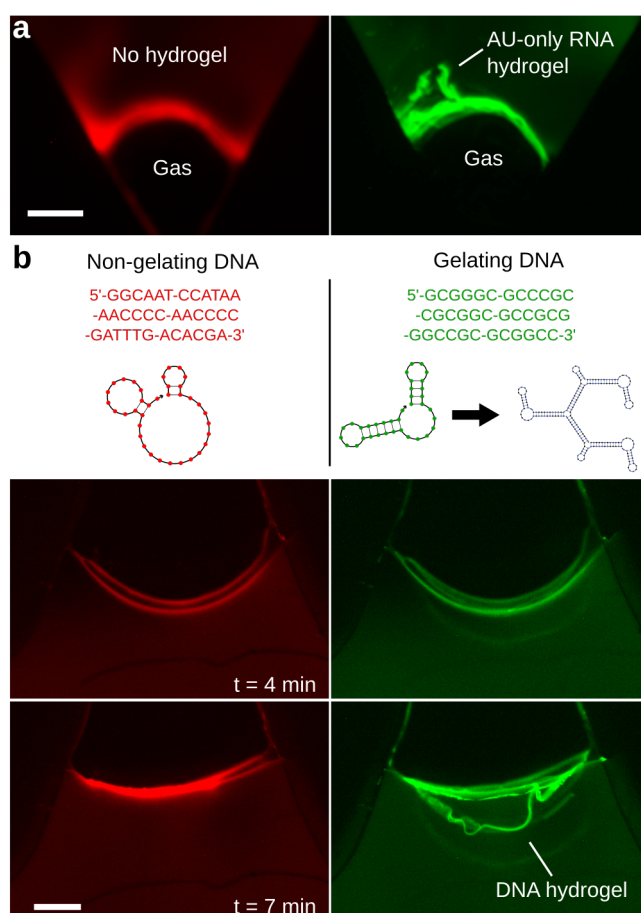
Figure 3.10: AU-only RNA and GC-only DNA Gelation. (a) AU-only RNA formed a gel (right) in the presence of a non-complementary RNA strand (left) under the same conditions as the GC-only gel. Scale bar: 500 μm. **(b)** The same sequences (replacing the base U for T) as for the RNA gelation from Figure 3.9b separate by selective gelation in a 20 °C temperature difference. Both DNA strands were accumulated simultaneously and the color channels illuminated separately. It shows that the gel structure formed by the green labeled DNA is not visible in the red color channel. The linear, non-complementary red strand is therefore not incorporated into the green gel. Here: T_{warm} = 30 °C, T_{cold} = 10 °C, initial DNA concentration: 10 μM, buffer: 1-fold PBS. Scale bar: 250 μm.

This was a 36mer for the GC-only RNA and a 60mer for the AU-only RNA, each with three self-complementary binding sites. Based on simulations (Nupack [70]), the gel-forming strands bind to each other and form a network of polymers (Figure 3.9b, right). Over the course of the experiment, both the non-complementary and the self-complementary strands accumulated at the same interface. But, after 21 minutes, a gel was only observed for the self-complementary RNA. No gel could be observed for the non-complementary RNA, which also accumulated near the surface but was not forming large-scale structures.

The two strands therefore separated macroscopically based only on their sequence. The self-complementary strands, even if detached from the surface, remained at high concentrations in the hydrogel and offered reduced hydrolysis rates due to their predominantly double-stranded nature. This sequence-selective gelation was also found for DNA (Figure 3.10b).

3.3.4 DNA Encapsulation in Vesicular Structures

A key requirement for the emergence of cellular life is the encapsulation of molecules at increased concentration relative to their more dilute external environment. Fatty acids are potential candidates that could separate nucleic acids in vesicles, possibly incorporating phospholipids into their membranes over time [71, 72]. For the encapsulation, three autonomous processes need to occur: (i) The accumulation of oligonucleotides to meaningful concentrations, (ii) the accumulation of lipids to trigger their aggregation or fusion, and (iii) the combination of both in one location to encapsulate oligonucleotides into vesicular structures. Here, it is shown that heated gas-water interfaces could fulfill these requirements.

To introduce lipids in a homogeneous manner, the chamber was filled with small 100 nm-sized vesicles prepared from a 10 mM oleic acid solution (0.2 M Na-Bicine, 1 mM EDTA, pH 8.5) and 2 µM DNA. In addition, approximately 0.1 % 1,2-dioleoyl-sn-glycero-3-phosphoethanolamine (DOPE, either with fluorescent label or without) was added to the oleic acid before diluting it in buffer, which significantly increased the aggregation described below. The initially small vesicles appeared as a continuous background (Figures 3.11a,b). After turning on the temperature gradient, the accumulation of these vesicles together with DNA was observed within ten minutes at the interface (T_{warm} = 70 °C, T_{cold} = 10 °C). Here, the vesicles aggregated together and formed larger clusters. Interestingly, the co-accumulated DNA was encapsulated into these vesicle clusters at an up to 18-fold increased oligonucleotide concentration compared to the bulk solution. These vesicle clusters were shuttled into the convection and Marangoni flows and frequently formed thread-like structures.

Vesicles formed from the phospholipid DOPC (3.6 mM DOPC, 0.2 M Na-Bicine, 1 mM EDTA, pH 8.5) showed a similar behavior. DOPE was added here as well, as described above. The accumulated 100 nm-sized phospholipid vesicles formed larger and more spherical structures compared to the oleic acid aggregates, and encapsulated DNA equally well. They also underwent fission due to shear stress in the convection flow (Figure 3.11c).

To characterize the vesicles more properly, the functionality of the encapsulated material was tested. To this end, the fluorophore DFHBI-1T was accumulated together with the RNA aptamer "Broccoli", which increases the fluorescence of DFHBI-1T when bound. Both were encapsulated into DOPC-vesicle aggregates (1 µM Aptamer, 10 µM DFHBI-1T, 3.6 mM DOPC, 50 mM HEPES, pH 7.6, 100 mM KCl, 1 mM $MgCl_2$). The aggregates could be observed in the lipid and DFHBI-1T color channel (Figure 3.11d, right). When the aptamer was exchanged with a non-binding RNA strand, the fluorescence of the fluorophore was reduced more than 100-fold. RNA can therefore readily bind inside the aggregates.

As a next step, it was investigated whether the encapsulated molecules were protected from their environment. To investigate this, a double-stranded DNA (dsDNA) strand was accumulated with DOPC vesicles (7.1µM DNA, 3.6 mM DOPC, 0.2 M Na-glycineamide pH 8.5, 6 mM $MgCl_2$, 1 mM $CaCl_2$). Each pair of dsDNA strands contained a FAM dye on one strand and a ROX dye opposite to it on the other strand. These dyes form a Förster resonance energy transfer (FRET) pair, in which the excited FAM dye can transfer energy to the ROX dye that then fluoresces. As this energy transfer works only in close proximity of the dyes, it was used to measure the amount of dsDNA inside the vesicle
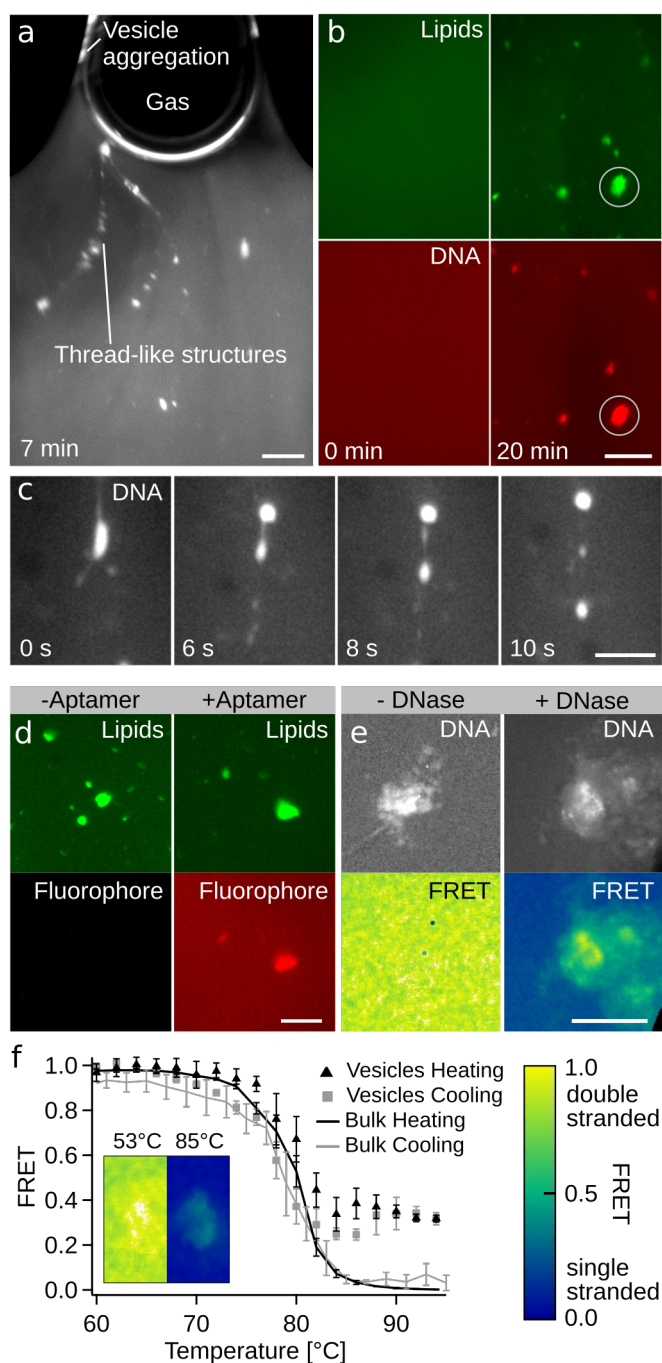
Figure 3.11: Vesicle aggregation and RNA and DNA encapsulation at the interface. Fluorescence microscopy images of DNA and lipid color channels. **(a)** Lipid channel: 100 nm-sized oleic acid vesicles were accumulated at the gas-water interface. They formed aggregates of vesicles that were ejected into the bulk and formed thread-like structures. **(b)** Comparison of lipid and DNA color channels (green: lipid, red: DNA) showed that lipids and DNA co-locate, meaning that the 100 nm-sized vesicles formed larger clusters and encapsulated DNA at up to 18-fold enhanced concentration compared to the bulk. **(c)** DNA channel: DOPC vesicles were accumulated under the same conditions and also encapsulated DNA at enhanced concentrations. Here, a fission of the DOPC vesicles containing DNA was observed in the shear flow. **(d)** Accumulation of a fluorophore with (right) and without (left) aptamer shows that RNA can be folded inside the aggregates. **(e)** FRET image of dsDNA before (left) and after (right) addition of DNase. DNA inside the aggregates was protected from the DNase. **(f)** Melting of DNA inside the aggregates observed by FRET signal over temperature. Scale bars: a,b,d,e: 200 μm; c: 100 μm.
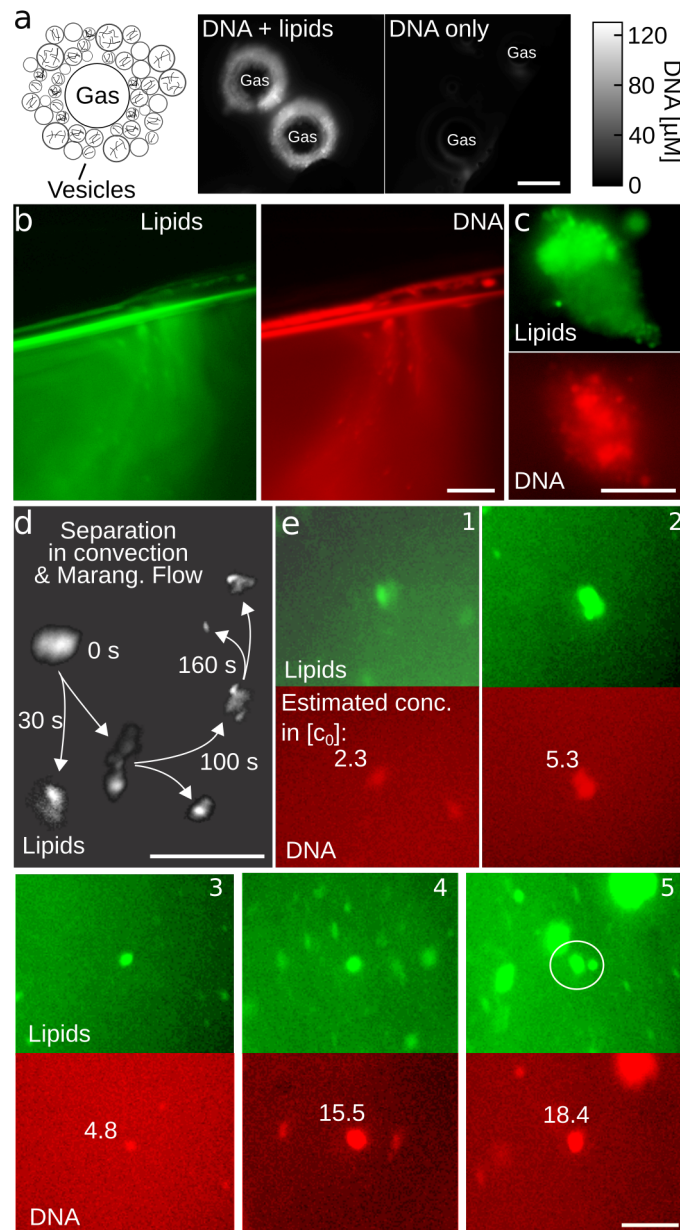
Figure 3.12: Formation of vesicle aggregates with accumulated oligonucleotides. (a) The aggregation of vesicles around small bubbles led to high local DNA concentrations, seen in the DNA color channel. The grayscale shows a lower limit of the inferred DNA concentration. In the absence of lipids, the accumulation around small bubbles was about four times lower. **(b)** Vesicular structures also form at a flat interface in contrast to the bent shape seen in Figure 3.11. **(c)** One of the large clusters formed at a gas-water interface. With the dual color fluorescence imaging it can be seen that it consists of several smaller parts with brighter and less bright areas in both the lipid and DNA color channels. **(d)** Tracing of the clusters formed at the interface shows that they become smaller and separate in the Marangoni and convection flows over the course of several minutes. **(e)** Five exemplary vesicles containing varying DNA concentrations with sizes between 15 µm and 40 µm in diameter. They all formed throughout the same experiment at a gas-water interface. Brightness/Contrast have been changed for each image to improve visibility. Fluorescence measurements and calculations of original images are given in the Methods section. Scale bars: a,b: 200 µm; c,d,e: 100 µm
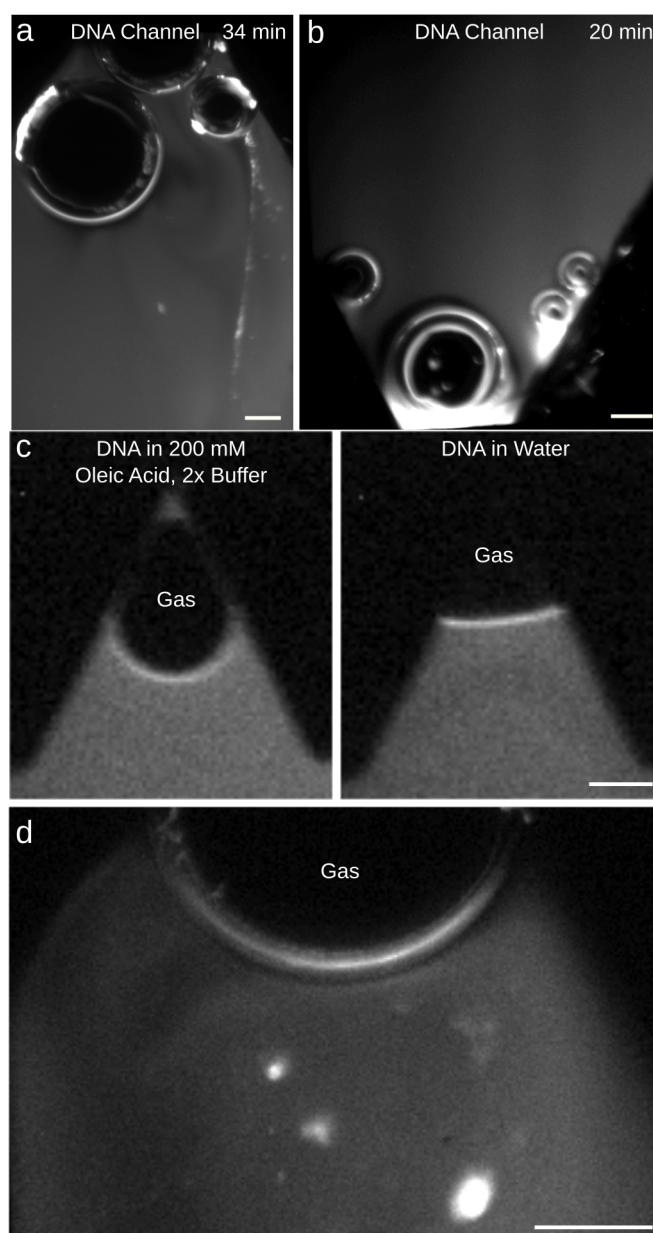
Figure 3.13: Vesicle Control Experiments. (a) Vesicle formation from non-extruded vesicles gives similar results. However, the formation of larger structures with encapsulated DNA takes longer. This suggests that vesicles larger than approx. 10 μm are not as easily accumulated as smaller, 0.1 μm large, vesicles. Still, however, within 34 minutes of accumulation the formation of large, thread-like structures around bubbles can be seen. **(b)** Accumulation of DNA under the same buffer conditions and concentrations as before in the absence of lipids. This control shows that no vesicles/encapsulated DNA emerges when lipids are not present throughout the experiment. **(c)** DNA [3.3 μM] in water (right) and in 200 mM oleic acid and 2x Bicine buffer (left) shows the same fluorescence intensity, the lipid concentration has no influence on the fluorescence. **(d)** The same aggregates form in the absence of DNA, they are not dominated by DNA-lipid interaction. Scale bars: a,b: 200 μm; c,d: 1 mm.

aggregates. The higher the signal—between 0 (all strands unbound) and 1 (all bound)—the more dsDNA was present. Calculations were performed as described in [20]. After the formation of aggregates at the interface, most of the solution was extracted and DNase I added to it (0.5 units to approx. 10 μl solution). The solution was then filled back into the chamber and the FRET signal observed at 37 °C. The DNase digested the DNA strands outside the aggregates, where the signal quickly dropped (Figure 3.11e). The FRET signal of the aggregates reduced only slightly, likely from the digestion of DNA in solution above/below the aggregates or sticking to their surface. Molecules within the aggregates were therefore efficiently protected from the DNase.

Using the same technique, melting curves of the dsDNA inside the aggregates could be measured. Figure 3.11f shows the FRET signal of the bulk and aggregates over temperature. The signal can be seen to start from 1 (all DNA bound) and going down to 0 (all DNA unbound) in the bulk. Inside the aggregates, the signal is reduced to approx. 0.3. Parts of the strands are likely stabilized or encapsulated by the aggregates in a way that does not allow them to unbind at higher temperatures. When the system is cooled again, both signals return to 1. Despite the fact that not all strands could be melted, the measurement shows that in large parts the encapsulated material is in an aqueous phase that allows the strands to unbind and bind again.

The vesicle aggregates (oleic acid or DOPC) concentrated around smaller gas-bubbles (150 μm in diameter), inducing a clustering of DNA (Figure 3.12a). This was not observed in the absence of lipids. Lipid vesicles therefore enriched the local DNA concentration. Figure 3.12b shows that aggregates also formed at perfectly flat geometries. Here, a chamber was constructed that did not contain any corners or angles where bubbles could be trapped but rather one large interface with gas on top. Vesicle clusters with concentrated DNA inside formed here due to their accumulation at the interface and their dissolution from the wall over time. Figure 3.12c shows an example of the clusters that formed in the chamber from Figure 3.11. Due to thermal convection, they were observed to divide and split into smaller compartments (Figure 3.12d). An overview of the observed aggregates in both lipid and DNA fluorescence channels is given in Figure 3.12e in the center of each image. They show varying intensities of DNA concentration, with a maximum of an 18.4-fold compared to the bulk solution. Calculations for the concentrations are given in the Methods section.

Above experiments assumed the presence of uniformly 100 nm-sized vesicles at the beginning. The behavior of the system when it initially contained a range of vesicle sizes with up to approximately 30 μm in diameter was also explored (Figure 3.13a). They exhibited a similar, but often slower accumulation behavior. Within 34 minutes, the system again started to form vesicle clusters that contained enhanced DNA concentrations. In the absence of lipids, the accumulation exhibited the enhanced accumulation at the interface, however no additional formation of clusters or vesicles was observed (Figure 3.13b). As a control, the fluorescence of DNA (3.3 μM) in water was compared to the fluorescence of DNA in high concentrations of lipids (200 mM oleic acid, 0.4 M Na-Bicine, Figure 3.13c). Both samples showed the same fluorescence, it did not change at high concentrations of fatty acids. To exclude that the aggregation was dominated by DNA-lipid interaction, vesicles were accumulated without DNA (Figure 3.13d). As expected, aggregates formed also under these conditions.
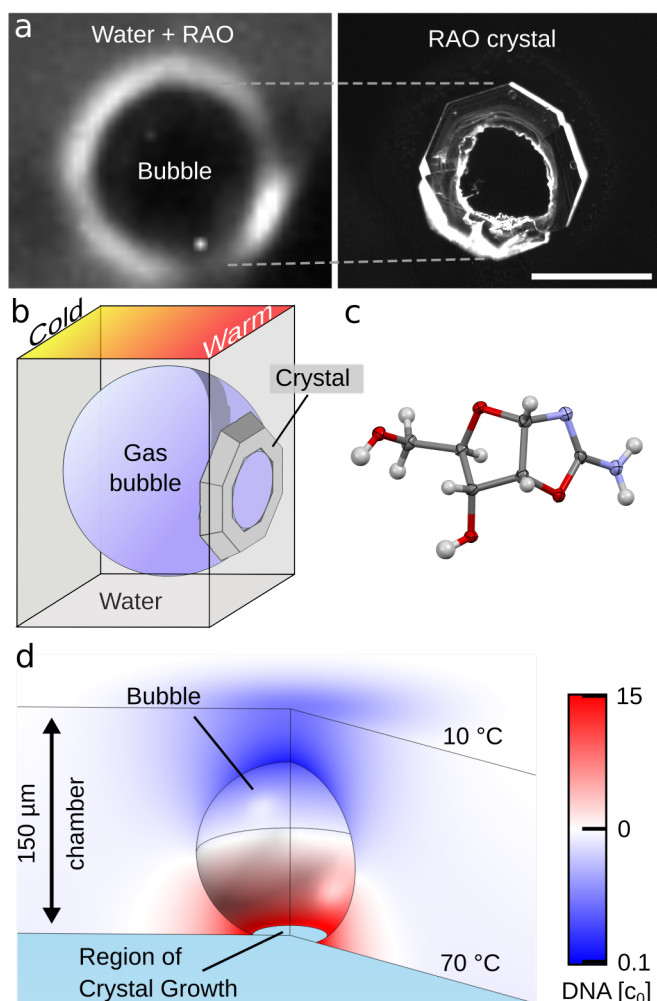
3.3.5 Crystallization at Gas Bubbles

Figure 3.14: Crystallization and bubble movement. (a) RAO accumulated from 40 mM bulk concentration around a growing bubble at the warm side of the chamber (70 °C). After 37 minutes, an RAO crystal formed below the bubble at the water-gas-solid interface as indicated. **(b)** The crystal shape suggests that it formed successively as the bubble grew, consistent with simulation results shown in (d). **(c)** X-ray crystal structure analysis of a D-RAO crystal grown at a gas-water interface. **(d)** The accumulation around small bubbles is lower compared to larger interfaces. This simulation shows the accumulation of a monomer around a small bubble in a 150 μm thick chamber in a 60 °C temperature difference (T_{warm} = 70 °C, T_{cold} = 10 °C). The maximum concentration increases by a factor of 15 compared to the bulk concentration. This reduced accumulation can be explained by the small size of the bubble and the fact that it is not in contact with the cold side of the chamber, both decreasing the turnover of evaporated water. Scale bars: 250 μm.

The building blocks for single nucleotides, such as the prebiotic RNA precursor ribose aminooxazoline (RAO), also accumulated near gas bubbles to concentrations that could trigger their crystallization. For RAO, a crystallization is of fundamental interest since it can be both diastereoisomerically purified by selective sequential crystallization of its precursors and enantiomerically enriched by conglomerate crystallization where the two enantiomers (D- and L-) of RAO crystallize into discrete independent domains [73,

74]. Elevated temperatures (70 °C warm side, 10 °C cold side) were used to trigger the spontaneous formation of a bubble. Subsequently, RAO accumulated and crystallized around it (Figures 3.14a,b). To achieve this, a 40 mM solution of D-RAO, 2.8-fold below the saturation concentration at T_{warm} = 70 °C (approximately 110 mM), was filled in a chamber without a corrugated geometry, which did not create a gas-water interface. For the crystallization to occur at the warm side of the chamber, RAO would have needed to accumulate several fold in order to overcome the nucleation energy barrier [75]. The fluorescence was monitored by adding 1 µM Cy5 to the solution, which co-accumulated at the gas-water interface but was not incorporated into the crystals.

An initially small bubble formed on the warm side and accumulated RAO around it. Within 40 minutes, the bubble grew while continuously increasing the concentration at the warm side. Here, the crystal shown in Figure 3.14a was found at the location where the bubble had formed. No crystals were found on the cold side of the chamber. Using micromanipulators and a needle, crystals from several experiments were scraped off the warm side of the chamber after it was disassembled. An X-ray crystal structure determination of this material confirmed that crystals grown on the warm side were indeed D-RAO (Figure 3.14c).

The accumulation of RAO at a small bubble in a 150 µm large chamber was simulated by transferring the simulation to an axial-symmetric system (see Methods section). It shows that small molecules such as RAO accumulated up to 15-fold in the system described above (Figure 3.14d). Very likely, the slow increase in accumulation as the bubble grew larger led to the growth of the crystal shown here. Faster accumulation kinetics would have formed many small crystals instead of one large crystal.
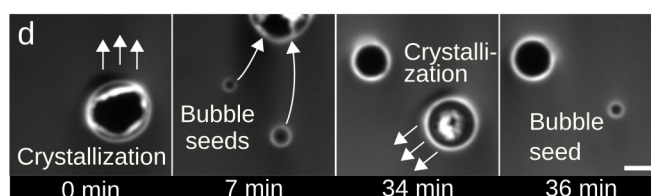
Figure 3.15: Crystal-induced bubble growth. Moving bubbles leave behind crystals (7 minutes) that act as seeds for new bubbles (34 minutes). Scale bar: 250 µm.

Interestingly, the formation of RAO crystals led to the re-formation of gas-bubbles near small cavities—a known and well-described process of heterogeneous nucleation in supersaturated solutions [75]. This crystal-induced bubble formation was observed in experiments at high T_{warm} = 70 °C (Figure 3.15). Once a gas bubble, around which RAO crystals had formed, moved away, it left behind accumulated material, possibly crystal cavities filled with gas, which facilitated the growth of new daughter bubbles at the same location. When these daughter bubbles also increased in size sufficiently, they started to accumulate RAO, formed crystals, and eventually moved away. The remaining crystals again hosted the growth of new bubbles and began the bubble-induced crystallization cycle again.

3.3.6 Dry-Wet-Cycles and Phosphorylation by Moving Interfaces

Figure 3.16: Dry-wet cycles and phosphorylation of nucleosides. (a) The movement of bubbles in the chamber left behind dried material in the front that was rehydrated at the back of the bubble as it moved in the indicated direction, leading to dry-wet cycles. The dashed circle indicates the position of the accumulation region at t = 0 minutes. **(b)** Using a hydrophobic cold side in the chamber increased the dry-wet cycling. Water droplets on the cold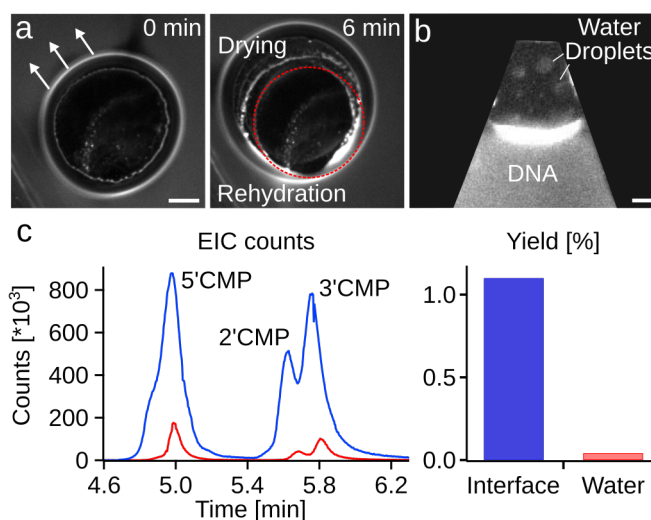 side grew larger and caused a stronger interfacial movement when merging with the bulk fluid. **(c)** cytidine nucleosides were phosphorylated in the chamber shown in (b). Over 12h, cytidine phosphorylated on average twenty times more effective at interfaces (blue, T_{warm} = 60 °C, T_{cold} = 37 °C, CMP yield: 1.1% ± 0.73% from 12 repeats) compared to bulk water at 60 °C (red, CMP yield: 0.042 % ± 0.02 % from 5 repeats) or 50 °C (CMP yield: 0.056% ± 0.0015% from 15 repeats). Left: Extracted-ion chromatogram (EIC) counts for CMP peaks after HPLC-MS analysis; right: Yields measured by HPLC and UV detection. Scale bars: a: 100 μm; b: 250 μm.

Bubbles tended to move upwards in the chamber (Figure 3.16a, left) due to buoyancy forces. This movement led to a continuous cycling of dry-wet conditions (Figure 3.16a, right), as accumulated material close to the interface entered the bubble, dried, and was rehydrated when the bubble moved away. At the same time, accumulated material at the trailing edge was dragged along as the bubble moved, keeping high molecule concentrations in the vicinity of the interface.

At a hydrophilic surface material such as silicon dioxide (quartz) used on the cold side in the experiments before, the contact angles of the condensed droplets were small and they re-entered quickly into the bulk water, leading to only little movement of the gas-water interface.

To trigger many wet-dry cycles, a Teflon foil was placed on the warm and cold sides of the chamber. In this setting, the phosphorylation of nucleosides, a reaction which usually requires dry conditions at elevated temperatures, was tested. The reaction is known to be most effective when the solution is dried at 100 °C, a scenario hard to reconcile with typical RNA-world conditions [7, 76]. Here, this phosphorylation reaction was twenty times more efficient (Figure 3.16c, T_{warm} = 60 °C, T_{cold} = 37 °C, 240 mM cytidine and ammonium dihydrogen phosphate, 2.4 M urea) compared to bulk water at the average temperature of 50 °C or 60 °C. The found enhanced *in situ* phosphorylation reaction would improve the recycling of hydolyzed RNA.

3.4 Discussion

In the experiments shown here, a general accumulation mechanism of molecules and small vesicles at gas bubbles subjected to heat flow in water was found. A temperature gradient across a gas-water interface created a continuous process of evaporation and condensation of water between the warm and cold sides. This moved molecules towards the bubble interface and increased their concentration by several orders of magnitude, depending on their diffusion coefficient. Since the contact line between gas and water was mobile, dry-wet cycles were created, in many conditions as often as twice per minute.

The simulation captured the basic characteristics of this accumulation and validated the experimental results. A 4000-fold DNA accumulation was reached both in experiment and simulation. In comparison with thermophoretic traps, with which the setting could be combined, the accumulation at the interface occurred significantly faster, on the timescale of minutes rather than hours [12].

The temperature gradients used in the experiments were adapted to the individual scenario, influencing also the strength of the accumulation (Figure 3.6). The gradients were kept at $10 - 40$ °C and $10 - 30$ °C for the Hammerhead and gelation experiments, respectively, to accumulate RNA strongly, but still under cold conditions to keep hydrolysis insignificant. Vesicles aggregated under similar conditions (Figure 3.11d), but the faster convective flows from higher temperature difference (10 °C $- 70$ °C) shuttled aggregated vesicles more efficiently away from the interface for downstream analysis. The creation of crystals from RAO required the larger temperature gradients for an efficient accumulation of the comparably small molecules. The phosphorylation chemistry of monomers profited from an overall enhanced temperature. However, all these systems could be combined with thermal traps as discussed in Chapter 2 by placing a bubble at the bottom of a pore. The thermal trap would then increase the bulk concentration of selected molecules around the bubble, while the bubble would provide a stronger local concentration at the interface. Smaller temperature differences could then reach similar concentrations due to already increased bulk concentration.

The co-accumulation of small ions offers additional reactivity. Divalent salts such as Mg^{2+} were predicted by our model to accumulate by a factor of 4 - 5 for temperature differences of 20 - 30 °C. High salt environments could enhance the hydrolysis of for example accumulated RNA, however the larger temperature differences also increase the movement of the interface by the recondensation of water, decreasing the time accumulated molecules spend dried at high temperatures. On the other side, the enhanced salt concentrations would trigger ribozymatic activity at the interface while the molecules in the bulk would be protected by low salt concentrations from hydrolysis.

The system provided in a single setting a network of widely different reactions, connected by the fast diffusive transport of molecules through water between different microbubbles. For example, the ligation chemistry to drive replication could be made possible by the high local concentrations of substrates, whilst the drying process in close proximity would trigger the necessary phosphorylation [7, 76] and activation chemistry [77] to drive the polymerization [8] of monomers. The dry-wet cycles were implemented continuously at the moving interface and molecules were retained at high concentrations at the interfaces after rehydration. In the adjacent water, molecules

thermally cycle between warm and cold by laminar thermal convection.

At the interface, a strongly enhanced ribozymatic activity was demonstrated by the accumulation of the Hammerhead ribozyme. Its activity at the interface clearly dominates the turnover of substrate in the system, with up to 50 % of the product being cleaved in a chamber with the gas interface compared to 3.8 % in the bulk. This can be attributed to higher local concentrations of ribozyme, substrate, and $MgCl_2$ at the interface. Product strands were shuttled back into the bulk solution, where they were protected against the higher salt conditions. The mechanism thereby provides a way to enhance catalytic activity and increase the efficiency of RNA-catalyzed processes.

Complex sequence phenotypes of RNA, such as several self-complementary sites on a single strand, have manifested themselves by a sequence selective formation of hydrogels at the interface. This process was not achieved by drying [48] and the gel maintained a high local RNA concentration in water, an interesting setting to support efficient RNA catalysis [78, 79]. Moreover, the high amount of hybridization in hydrogels likely protected oligonucleotides from hydrolysis [49], enabling RNA sequences to survive even in challenging salt concentrations.

In the presence of lipids such as oleic acid or DOPC, the accumulation at the heated gas-water interface led to the continuous encapsulation of oligonucleotides into vesicle aggregates. The local DNA concentration inside the aggregates increased by a factor of up to 18 as compared to the bulk solution. The encapsulation of oligonucleotides into lipid membranes is considered to be one of the key elements for more complex life and it has been suggested that lipids facilitate the assembly and polymerization of monomers [80, 81]. Their functionality was shown here by encapsulating folded RNA and demonstrating the melting and re-annealing of DNA inside the aggregates. In the convection flow, the aggregates were subjected to temperature cycles and shear forces, which lead to their fission. DOPC produced similar aggregates compared to oleic acid, showing that phospholipids produced under potentially prebiotic conditions [82] could accumulate and encapsulate oligonucleotides in the shown conditions.

For the prebiotic synthesis of RNA from sugar-nucleobase precursors, the crystallization at microbubbles would enable their purification [73] and possibly also their chiral amplification by the enhanced growth of conglomerate RAO crystals [74]. Interestingly, these crystals became condensation sites that later again triggered the formation of new gas bubbles. If the seed crystal was homochiral, the subsequent bubble formation could accumulate and promote the assembly of more homochiral molecules at the same location. Finally, prebiotic dry chemistry such as the phosphorylation of nucleosides was enhanced by the interface. Cytidine formed CMP twenty times more effective compared to its phosphorylation under aqueous conditions.

To conclude, the experiments show multiple modes of condensation, enrichment, and accumulation at heated gas microbubbles. This led to the physicochemical assembly and localization of prebiotic molecules such as RNA precursors, lipids, and oligonucleotides. The accumulation of molecules at a gas-water interface is likely a robust feature of natural microfluidic systems in submerged volcanic pores, a setting ubiquitous on early Earth [15, 50]. The simultaneous occurrence of six synergistic mechanisms for the accumulation and processing of prebiotic molecules, all operated in close proximity, fulfills the requirements to connect a cascade of reactions in the same non-equilibrium

environment.

The setting presented here could have largely helped in an informational polymer world, in which the first simple replicators were evolving. Following a synthesis of life's first building blocks, the accumulation at gas-water interfaces offers a mechanism to select polymers, enhance their catalytic activity, and subsequently encapsulate them.

3.5 Methods

DNA sequences.

The sequences for the accumulation experiments were:

- 132mer (length-selective accumulation): 5'-GGC AAT CCA TAA – 18*(AACCCC) – GAT TTG ACA CGA-3'

- 72mer (length-selective accumulation, vesicle accumulation, FRET): 5'-TGG ACA TGC GTG CTG AGT AGA AGG AAG GAA GGA AGG AAG GAA GGA AGG AAG GCA GTC TTG TGA CGG GAT GTG-3'

- 72mer complement (FRET): 5'-CAC ATC CCG TCA CAA GAC TGC CTT CCT TCC TTC CTT CCT TCC TTC CTT CCT TCT ACT CAG CAC GCA TGT CCA-3'

- 36mer (length-selective accumulation, selective gelation–non-complementary): 5'-GGC AAT CCA TAA AAC CCC AAC CCC GAT TTG ACA CGA-3'

- 36mer (selective gelation—self-complementary): 5'-GCGGGC GCCCGC CGCGGC GCCGCG GGCCGC GCGGCC-3'

- 15mer (length-selective accumulation): 5'-GGC AAT CCA TAA AAC -3'

RNA sequences.

- Hammerhead ribozyme: 5'-GGGAG CUGAA CUGAU GAGUC CGUGA GGACG AAAGG CACA-3'

- Hammerhead inactive mutant: 5'-GGGAG CUGAA CUAAU GAGUC CGUGA GGACA AAAGG CACA-3'

- Hammerhead Substrate (Synthesized by eurofins Genomics): 5'-[FAM]-UGCCUC UUCAGC-[BHQ1]-3'; BHQ1 is the "Black Hole Quencher 1" from Biosearch Technologies, Inc.

-AU self-complementary RNA (Gelation): 5'-UUUAA UAUAA UUAUA UUAAA UUAAU AUUAA UUAAU AUUAA AUAUA UAUUU AAAUA UAUAU-3'

- Broccoli Aptamere: 5'-GGGAG ACGGU CGGGU CCAGA UAUUC GUAUC UGUCG AGUAG AGUGU GGGCU-C-3'

- RNA 38mer (Aptamer control): 5'-GGCAA UCCAA UAAAA CCCCA ACCCC GAUUU GAACA CGA-3'

The wild-type Hammerhead (HH), inactive HH, and broccoli RNAs were transcribed in vitro by T7 RNA polymerase by the Mutschler lab (Max Planck Institute for Biochemistry, Martinsried, Germany). Additional samples of broccoli RNA were from chemical synthesis (Biomers, Ulm, Germany). dsDNA templates for transcription were produced by two cycles of mutual extension (GoTaq HotStart, Promega) between the associated DNA oligonucleotide (sTRSV_min_wt_TX/ sTRSV_min_mut_TX / broccoli_TX) and 5T7 followed by column purification (Monarch® PCR & DNA Cleanup Kit, NEB). Ribozyme and aptamer RNA was transcribed from the double-stranded templates using the MEGAshortscript™ T7 Transcription Kit (ThermoFisher), and purified using RNeasy (Qiagen). DNA sequences are GATCG ATCTC GCCCG CGAAA TTAAT ACGAC TCACT ATA (5T7), TGTG CCTTT CGTCC TCACG GACTC ATCAG TTCAG CTCCC TATAG TGAGT CGTAT TAATT TC (sTRSV_min_wt_TX), TGTGC CTTTT GTCCT CACGG ACTCA TTAGT TCAGC TCCCT ATAGT GAGTC GTATT AATTT C (sTRSV_min_mut_TX), GAGCC CACAC TCTAC TCGAC AGATA CGAAT ATCTG GACCC GACCG TCTCC CTATA GTGAG TCGTA

TTAAT TTC (broccoli_TX). All other RNA and DNA strands were from Biomers (Ulm, Germany), if not stated otherwise.

Chamber Construction.

For the experiments in Figure 3.4, a thermal chamber was sandwiched from a thin (>240 μm) layer of PETG plastic film deposited on a silicon wafer using an 3D printer (Ultimaker 2) in a funnel shape to facilitate a gas-water interface (Figure 3.2). A sapphire (Al_2O_3) block sealed the chamber. The chamber was filled through two 240 μm thick borosilicate capillaries (Vitrocom). The system was annealed at 150 °C and the sapphire pressed down, fixing the thickness to 240 μm. Polydimethylsiloxane (PDMS) was deposited around to seal the chamber. For most other experiments, chambers were built with a UV-curable resin (Photocentric 3D Daylight Resin, flexible, color: amber) through a master obtained by laser printing on a transparency film. Spacers between master and resin defined a chamber thickness to 150 μm or 250 μm. After illumination, sapphire windows were placed on top of the chambers and sealed with the resin. Microfluidic access was given through holes in the sapphire. Similarly, the chamber used for the phosphorylation and Hammerhead experiments was built by replacing the resin with a 254 μm thick Teflon foil from which the structure was cut out. Additional Teflon foils were placed on the warm and cold side of the chamber for the phosphorylation experiments to mimic a hydrophobic surface. The temperature gradient was produced by heating the sapphire block through copper fixtures using joule heaters (heater cartridge for 3D printers, 12V 40W, 6 mm diameter) and cooling the silicon side with a water bath. Temperature sensors and PID software maintained the temperatures. The temperature inside the chamber was calculated from the chamber geometry and known material constants with finite element methods (Comsol).

Fluorescence was measured with a fluorescence microscope (Zeiss Axio) through the transparent sapphire heating block using Mitutoyo infinity corrected long working distance objectives (2x, 10x) and a Zeiss Fluar 5x objective. The accumulation of DNA was detected with 200 nM FAM-labeled 132 base ssDNA in 0.1-fold PBS (DNA sequences above). The silicon substrate was maintained at 10 °C, while the copper heaters were initially turned off. The experiment began with the copper heaters set to maintain a desired temperature. Background intensity levels were obtained from the non-fluorescing gas region. The bulk fluorescence signal was obtained from an area far from the free interface. The accumulated DNA fluorescence ratio was averaged perpendicular to the interface and divided by the bulk fluorescence. The flow was visualized with 200 nm FAM-labeled polystyrene beads in 0.1-fold PBS. The position and velocities of the beads were tracked using ImageJ.

Bead Tracking.

The beads from Figure 3.4 were tracked using the ImageJ plugin "Particle Tracker" from the Mosaic Suite [83]. Here, the particles near the contact line were tracked and the result cropped by hand to get rid of tracks that were too short or did not move towards the contact line. The endpoints of all remaining tracks were set to zero. Figure 3.4e shows the distance of these tracks perpendicular to the contact line. Tracks were slightly smoothed and the speeds analyzed by calculating the central differences ((w[N+1]-w[N-1])/2*dX) of the points using Igor Pro 5.03. The average speed of the beads before reaching the contact

line was ca. 50 μm/s, with many beads reaching top velocities of 80 μm/s (Figure 3.4). The simulation gives slightly higher average values for these speeds. It should, however, be noted that especially the last experimental points are always underestimating the full flow as beads might have gotten stuck to the wall before reaching the contact line and the frame time of 100 ms causes beads that stop within this time to be seen as slower.

Simulation Protocol.

Simulations were performed using the finite element software COMSOL v 4.4. The 2D model solved the convective heat equation, molecule diffusion equation, and Navier-Stokes equations perpendicular to the contact line. Marangoni flows were established by implementing a stress boundary condition of the fluid velocity at the interface and by introducing a temperature-dependent surface tension. Constant temperatures were fixed at the hot and cold walls of the chamber. The water vapor concentration was simulated in the gas region above the interface by a diffusion-convection equation. The gas velocity was calculated from the temperature profile. Its velocity, combined with diffusion, caused an efficient net mass transport of vapor away from the interface into the gas bubble. By coupling a temperature dependent vapor concentration boundary condition to the interface, a velocity boundary condition for water at the interface was imposed by the state equation of water. This resulted in capillary flow and evaporative mass transport of the water vapor, allowing vapor to enter and escape the water through evaporation or condensation. The water vapor concentration was defined by the formula: (exp(20.438 - (5044[K]/T))[mmHg]) / (R_const * T) with R_const the gas constant. It was derived from the ideal gas law and the approximation for the vapor pressure: P = exp(20.438-5132/T). The capillary flow was defined as an outlet flow coupled to the vapor concentration by: (D * M /rho) * (nx * cx + ny * cy) with D the diffusion constant of vapor, M the molecular mass, rho the local density, and nx and ny the normal vectors in x- and y-direction, respectively, and cx and cy the derivation of c in x- and y-direction, respectively. Thermophoresis was introduced via a thermophoretic drift term in the convection-diffusion equation describing the DNA concentration as done in previous publications [12, 20], the Soret coefficients of the DNA were taken from experimental data [84]. To incorporate the time lag of the heating process, the sapphire temperature was measured over time and incorporated as a polynomial function. The above simulation was solved over time, resulting in the time evolution of accumulation at the contact line. To fit the simulation to the observed data, the surface tension dependency on temperature was set within observed values [85] and fine-tuned as a free parameter using the bead tracking data. The geometry of the interface itself was adjusted to moderately tune the DNA accumulation dynamics. Concentrations were determined by averaging the top 10 μm of the meniscus at the hot side and comparing this to the simulated and experimental fluorescence, establishing a relation between fluorescence and average tip-concentration.

From the simulation the temperature gradient along the interface could be inferred (Figure 3.3). It shows that despite some slight deformations it could still be approximated as linear.

To simulate the bubble shown in Figure 3.14, the simulation was transferred to an axial-symmetric geometry with spherical coordinates. Here, the simulation around a small bubble was closed and gravity was pointed downwards. This removed the slow convection of water in the simulation, which, as expected from theoretical modeling, did

not change the accumulation characteristics. Here, the bubble is not in contact with both sides but only the warm side. The warm and cold side temperatures T_{warm} and T_{cold} were 70 °C and 10 °C, respectively. The simulation shows a maximum increase in concentration by a factor of ca. 15 for the estimated diffusion coefficient of 500 $\mu m^2/s$ at 10 °C. Ion and salt diffusion coefficients were taken from [86–88].

Hammerhead Accumulation.

Hammerhead ribozyme, substrate, and $MgCl_2$ were mixed immediately before filling them into the chamber (0.1 µM Hammerhead, 0.5 µM Substrate, 0.4 mM $MgCl_2$). Remaining material was mixed with loading buffer for PAGE analysis, which stopped the reaction, and cooled. This gave the 0 minutes sample. After 25 minutes, samples were flushed out of the chamber, mixed with loading dye, and frozen until analysis. All samples were diluted in order to give the same concentration. For the analysis, the fluorescent intensities of the bands were calculated and normalized. Intensities from the uncleaved substrate were multiplied by 1.69, the factor by which the fluorescence was still quenched due to the Black Hole Quencher [27].

Gelation.

For the gelation, 10 µM of DNA or RNA (Biomers, Ulm, Germany) with two fluorescent dyes were accumulated in a 1-fold PBS buffer at T_{cold} = 10 °C. All strands were denatured at 90 °C for five minutes before each experiment. In the experiment, T_{warm} was set to 30 °C with T_{cold} at 10 °C. Both FAM and Cy5 color channels were alternately illuminated every 5 s (one image every 2.5 s, one image per color per 5 s). Data from the fluorescence measurements was used to estimate the concentration in the gel from Figure 3.9a. Therefore, the fluorescence intensity of the gel, the size of the gel, and the fluorescence of the background DNA was measured. From this, the DNA concentration was calculated as follows: Fluorescence of gel: 996 counts; DNA background: 406 counts; dark background: 82.6 counts; gel size: 50 µm diameter. Chamber size: 240 µm. Estimation of concentration:

$$\frac{(996-82.6-(406-82.6)\cdot(\frac{240-50}{240}))\cdot(\frac{240}{50})}{(405-82.6)}$$

From the fluorescence of the gel the dark background and the assumed background of the DNA in solution behind/in front of the gel was subtracted after subtracting the gel size from the chamber width and normalizing to one. This was then multiplied by the ratio of chamber and gel size to get the assumed counts if the gel was 240 µm thick (fills the whole chamber). Dividing this by the DNA background gives a lower estimate of the factor by which the DNA concentration increased inside the gel. The sequences of the two DNA strands are given in the beginning of this section. For the RNA experiments the same sequences were used (replacing T for U). Sequence analyses and structures were obtained from Nupack [70] (www.nupack.org, structural analysis at 31 °C).

Vesicle Aggregation/Formation at Gas-Water interface.

The vesicle preparation from oleic acid used:1 µl of 99% oleic acid that was mixed with 300 µl 0.0088 mM labeled DOPE CF lipids (Avantilipids, #810332) in Methanol. After the methanol had evaporated the lipids were re-diluted in 300 µl buffer (0.2 M Na-Bicine, 1 mM EDTA, pH 8.5) and vortexed until the lipids had dissolved completely and the

solution was cloudy. The resulting mixture had an oleic acid concentration of 10 mM and DOPE-CF concentration of 8.8 μM. It was then extruded in a Mini-Extruder (Avanti Polar Lipids) using 0.1 μm PC membranes for at least 13 times, until the solution became clear. Adding DNA (2 μM final concentration) before or after vesicle formation did not change the results, experiments were performed under both conditions. Here, T_{warm} and T_{cold} were 70 °C and 10 °C, respectively. Vesicles also formed at T_{warm} = 30 °C, but were ejected less efficiently from the interface into the convection flow. DOPC vesicles were created with the same protocol (DOPC concentration: 150 mM). The DNA concentration inside the vesicles were estimated as follows: The vesicles were assumed to be spherical and the diameter was measured. From all fluorescent measurements a dark background count was subtracted. First, the fluorescence of the DNA background was measured in the beginning of the movie, which gives the mean fluorescence of a 1-fold DNA concentration through the full 240 μm large chamber. The fluorescence of the vesicle d_i was measured in the center of the vesicle and the DNA background e_i around the vesicles as well. From the vesicle fluorescence the calculated fluorescence of the DNA background e_i of (240 μm – vesicle diameter) was subtracted. The resulting intensity gives then the fluorescence of the vesicle alone. This was multiplied by a factor to give the fluorescence of a 240 μm large vesicle and subsequently divided by the 1-fold DNA fluorescence to give the DNA concentration in multiples of the initial DNA concentration. The calculations for the five vesicles from Figure 3.12d can be seen below:

Dark Background: 0.15 counts = a; DNA Background: 13.9 counts = b; Vesicle Diameter: c_i [μm]; Vesicle Fluorescence: d_i [counts]; Vesicle Background: e_i [counts]

Vesicle 1: c_1 = 35 μm; d_1 = 14.3; e_1 = 11.2; Vesicle 2: c_2 = 40 μm; d_2 = 25; e_2 = 15.5; Vesicle 3: c_3 = 15μm; d_3 = 19.3; e_3 = 16.2; Vesicle 4: c_4 = 27 μm; d_4 = 34; e_4 = 11.2; Vesicle 5: c_5 = 30 μm; d_5 = 44; e_5 = 14.1; Calculation were as described above:

$$\frac{(d_i - a - (\frac{240\ \mu m - c_i}{240\ \mu m}) \cdot (e_i - a)) \cdot (\frac{240\ \mu m}{c_i})}{b - a} \tag{3.1}$$

The results are: Vesicle 1: 2.3; Vesicle 2: 5.3; Vesicle 3: 4.8; Vesicle 4: 15.5; Vesicle 5: 18.4

This estimate assumes that the particles were spherical, but these estimates are rather conservative because they assume the DNA fluorescence to be homogeneous inside the vesicular structure in z-direction. Bright, small vesicles local DNA concentrations will have concentrations larger than above estimations.

For FRET measurements, no labeled DOPE but 0.03 mM unlabeled DOPE (Avantilipids, #850725) was added to 3.6 mM DOPC, which increased the number of aggregates formed. Glycineamide buffer was used for these experiments as it was experienced to perform better at the required $MgCl_2$ concentrations. DNase I was from New England Biolabs (#M0303S). For aptamer measurements, 0.03 mM unlabeled DOPE as well as 0.0025 mM DOPE-Cy5 (Avantilipids, #810335) was added to 3.6 mM DOPC before extrusion. HEPES buffer at pH 7.5 was used as the aptamer was more fluorescent under these conditions. DFHBI-1T was from Tocris/Bio-Techne (Cat. #5610). FRET measurements were performed as described in [20]. In short, a donor (FAM) and acceptor (ROX) dye were attached opposite to each other on a 72mer dsDNA strand. The donor was then excited by an LED and could transfer energy via nonradiative dipole-dipole coupling to the acceptor, which then emitted light. A second LED only excited the acceptor, allowing for a calibration of the

system and a concentration-independent measurement. The concentration-independent, crosstalk-corrected signal was then calculated according to Eqs. S11 and S12 in [20].

RAO crystallization.

Ribose aminooxazoline was provided by the Powner Group (UCL, London, UK) in pure D- and L-version. To observe the crystallization, pure D-RAO was saturated at 40 °C (ca. 40 mM) in 1 μM Cy5 solution (Lumiprobe, Germany, #23390) in pure water. For the experiment in Figure 3.14a, T_{warm} and T_{cold} were 70 °C and 10 °C, respectively. For the experiment in Figure 3.14d, the solution was saturated at room temperature and accumulated at T_{warm} = 60 °C, T_{cold} = 10 °C. The chamber thickness was 150 μm. Crystals were collected from the warm side of the chamber after each experiment using micro-manipulators and thin needles. They were transferred to a tube and analyzed using X-ray cystallography. The CCDC number of the analysis is 1847429.

Phosphorylation.

For the phosphorylation, 240 mM cytidine (Sigma Aldrich, #C4654) was mixed with 240 mM Ammonium Dihydrogen Phosphate (#1014400050) and 2.4 M Urea (#U5378) in water. The samples were filled in the Teflon chamber as described above and a temperature gradient between 60 °C and 37 °C was established. After 12h, the chamber was taken apart and the samples extracted from the interface region. Samples were analyzed using HPLC (Agilent Infinity II) and mass spectrometry (Agilent 6230 TOF LC/MS). For comparison, bulk water phosphorylation was performed at 50 °C and 60 °C in a 0.2 ml tube. Here, paraffin oil was placed on top of the mixture to prevent drying.

Single crystal X-ray diffraction.

The crystallographic (analysis performed by the Powner Group) data was collected using an Agilent SuperNova (Dual Source) single crystal X-ray diffractometer equipped with an Atlas CCD detector. The data set was collected at 150 K using CuKα radiation (λ = 1.54184 Å). The data was collected and processed using the CrysAlisPro [89] program. Lorentz and polarization corrections were applied using the same software. Structure solution and refinement were performed using SHELXS [90] and SHELXL [91], respectively. The crystal structure was solved using direct methods. All non-hydrogen atoms were refined anisotropically, while hydrogen atoms associated with carbon and oxygen atoms were refined isotropically in geometrically constrained positions. Hydrogen atoms affiliated with nitrogen atoms were refined isotropically in positions identified in the difference Fourier map. The positions and anisotropic displacement parameter of these hydrogen atoms were constrained in the final refinement cycle. The crystallographic and refinement parameters are given in Table 3.2.

Compound	Amino oxazoline
Empirical formula	$C_6H_{10}N_2O_4$
Formula weight	174.16
Temperature/K	150.00(10)
Crystal system	orthorhombic
Space group	$P2_12_12_1$
a/ Å	8.3862(1)
b/ Å	8.5652(1)
c/ Å	10.0482(1)
$\alpha/°$	90
$\beta/°$	90
$\gamma/°$	90
V / Å^3	721.757(14)
Z	4
ρ_{calc} / g·cm^{-3}	1.603
μ / mm^{-1}	1.168
F(000)	368.0
Crystal size / mm^3	0.221·0.116·0.102
Radiation	CuKα (λ = 1.54184)
2Θ range for data collection /°	13.584 to 147.254
Index ranges	-10≤h≤10 -10≤k≤10 -12≤l≤12
Reflections collected	24569
Independent reflections	1461 [R_{int} = 0.0335, R_{sigma} = 0.0096]
Data/restraints/parameters	1461/0/117
Goodness-of-fit on F^2	1.072
Final R indexes [I>= 2σ(I)]	R_1 = 0.0238, wR_2 = 0.0622
Final R indexes [all data]	R_1 = 0.0240, wR_2 = 0.0623
Largest diff. peak/hole / e Å^{-3}	0.20/-0.19
Flack parameter	0.05(4)
Hooft parameter	0.07(3)
CCDC Number	1847429

Table 3.2: Crystallographic and refinement parameters of D-ribofuranosyl-aminooxazoline

Chapter 4

Circular Dichroism Imaging Microscopy

4.1 Summary

Chirality is a central aspect of biological systems. Cells often use only one chiral version of a biomolecule as a building block for polymers, be it for the synthesis of RNA, DNA, or proteins. The question remains why living systems use e.g. D-ribose as the backbone for DNA and RNA, or why only very little organisms use D-amino acids [92]. During the origin of life, physical processes such as the crystallization of sugar molecules into chirally pure domains could have initiated a chiral amplification at a very early stage [74]. To better understand the role of these processes, a UV-light circular dichroism microscope was designed. The aim was to observe the growth of chirally pure crystals from ribose aminooxazoline, an RNA precursor [74], in solution. In the following, the setup and calibration of the circular dichroism microscope is described along with exemplary measurements. Results show that the sign of the CD of an RAO sample could be determined to a certain extent. Its large UV-absorbance and limits in detection range of the setup, however, made imaging a crystal and precise measurements difficult.

4.2 Introduction

4.2.1 Chirality

Discovered by Louis Pasteur in the 19th century [93], chirality describes the property of an object or molecule of being distinguishable from its mirror image. A prominent example are the left and right hands, which have the same structure but cannot be superposed onto each other. This led to the term left- and right handedness when talking about chiral objects. Two chiral versions of the same molecule are called enantiomers. These are stereoisomers, meaning they have the same molecular formula and structure, but are mirror images of each other when regarding their geometry. Modern life forms can react strongly to two enantiomers of the same molecule. In the 1960s, the drug thalidomide, called Contergan in Germany, was sold as a sedative to pregnant women, but was later discovered to lead to birth defects. It was shown that the sedating effect was caused by one of thalidomide's two enantiomers, R-thalidomide, while S-thalidomide is assumed to be the molecule that is toxic to the human reproductive system [94].

Chiral molecules can, however, also have a biological function. The backbone of DNA and RNA for example exclusively consists of D-ribose. A strand with an L-ribose backbone cannot bind to one with a D-ribose backbone, even if their bases are complementary [94]. This is important for molecular recognition and the replication of nucleic acids [95], and means that at some point in evolution chirally pure polymers were favored over racemic mixtures. From this, the question arises at what stage during the origin of life a chiral selection could have taken place.

Hinting towards an early selection is the fact that an enantiomeric excess (e.e.) of L-amino acids was found in carbonaceous chondrite meteorites [96]. This could have been a starting point for a further chiral selection in which the amino acids amplify the enantiomeric excess of RNA building blocks[97]. This asymmetry in meteorites could have been initiated by circularly polarized light from interstellar radiation [98]. Additionally, it was shown that the crystallization of RNA precursor molecules such as ribose aminooxazoline can lead to an enantioenrichment of their respective stereoisomers in solution, as the two crystallize in independent domains [74, 97].

To detect different enantiomers, circular dichroism (CD) spectroscopy is commonly used. It utilizes the property of chiral molecules, but also of chiral secondary structures such as α-helices in polypeptides [99], to absorb left and right circularly polarized light (CPL) differently.

4.2.2 Circularly Polarized Light and Circular Dichroism

Light, i.e. electromagnetic radiation, can be described by two perpendicular electric and magnetic fields E and H, respectively. Its direction of motion is thereby orthogonal to the two fields. For circularly polarized light, the electric field of a wave can be written as:

$$\vec{E}_L = Re\left\{ \vec{e}_L \, E_0 e^{i\psi} \right\}$$
$$\vec{E}_R = Re\left\{ \vec{e}_R \, E_0 e^{i\psi} \right\} \tag{4.1}$$

with the polarization vectors $\vec{e}_L$ and $\vec{e}_R$ for left and right CPL, respectively, E_0 the amplitude of the wave, and $\psi = \omega t - n\kappa z$ with n the refractive index of the medium

the light is passing through, and $\kappa = \frac{2\pi}{\lambda}$ [100]. The polarization vectors are defined by

$$
\begin{aligned}
\vec{e}_L &= \frac{1}{\sqrt{2}} \begin{pmatrix} 1 \\ i \end{pmatrix} \\
\vec{e}_R &= \frac{1}{\sqrt{2}} \begin{pmatrix} 1 \\ -i \end{pmatrix}.
\end{aligned}
\tag{4.2}
$$

Similarly, the magnetic field is given by

$$
\begin{aligned}
\vec{H}_L &= Re \left\{ \vec{h}_L H_0 e^{i\psi} \right\} \\
\vec{H}_R &= Re \left\{ \vec{h}_R H_0 e^{i\psi} \right\}
\end{aligned}
\tag{4.3}
$$

with

$$
\begin{aligned}
\vec{h}_L &= \frac{1}{\sqrt{2}} \begin{pmatrix} -i \\ 1 \end{pmatrix} \\
\vec{h}_R &= \frac{1}{\sqrt{2}} \begin{pmatrix} i \\ 1 \end{pmatrix}.
\end{aligned}
\tag{4.4}
$$

Here, $H_0 = n \cdot E_0$. These vectors define the rotating electric and magnetic fields of a propagating wave. As definitions for left and right CPL differ in the literature, in this work right CPL is defined by a clockwise rotation of the electric field from the point of view of the source of the radiation, left CPL by a counter-clockwise rotation. Therefore, when pointing in the direction of propagation of the light with the thumb of the right hand, the remaining fingers give the rotation of right CPL.

Only the electric field plays a role when regarding the absorption of light by a medium. The process is determined by the electric dipole transition moment of the excited electrons. When measuring the circular dichroism, also the magnetic moment plays a role. The interaction between the wave's magnetic field and the molecule induce a magnetic dipole moment in chiral molecules that leads to a different absorption of left and right CPL [100, 101]. As a consequence, circular dichroism spectroscopy is used e.g. to analyze the secondary structure of proteins [102] or, as intended here, to measure the enantiomeric excess of a molecule in solution.

CD can be measured in ΔA, i.e. differences in the absorbance A. It is defined as

$$
\Delta A = A_L - A_R = (\epsilon_L - \epsilon_R)Cl = \Delta\epsilon Cl
\tag{4.5}
$$

with A_L and A_R the absorbance of left and right CPL, respectively, ϵ_L and ϵ_R their respective molar extinction coefficients, C the molar concentration and l the path length of the measurement in cm. This follows from the Beer-Lambert law, which states that the absorbance of a medium is given by $A = \log_{10}\left(\frac{I_0}{I_t}\right) = \epsilon \cdot c \cdot d$, with I_0 and I_t the incident and transmitted light intensity, respectively. The molar circular dichroism $\Delta\epsilon$ then gives the CD of a sample independent of its concentration and the measured path length.

For visible light, Kahr et al. demonstrated the construction of a circular dichroism imaging microscope (CDIM) [103], which was used to visualize the CD of anisotropic

crystals. They analyzed the samples using left and right CPL in a transmission microscope and determined the CD of a crystal by calculating

$$CD = \frac{I_R - I_L}{I_0} \tag{4.6}$$

where I_R and I_L are the transmitted intensity of the right and left CPL, respectively.

However, this setup was not applicable to study the CD of RAO crystals as sugar molecules such as RAO show a CD mostly in deep-UV (below 300 nm) [104]. It was therefore attempted here to build a CDIM using deep-UV light.

4.3　Circular Dichroism Imaging Microscope in Deep UV
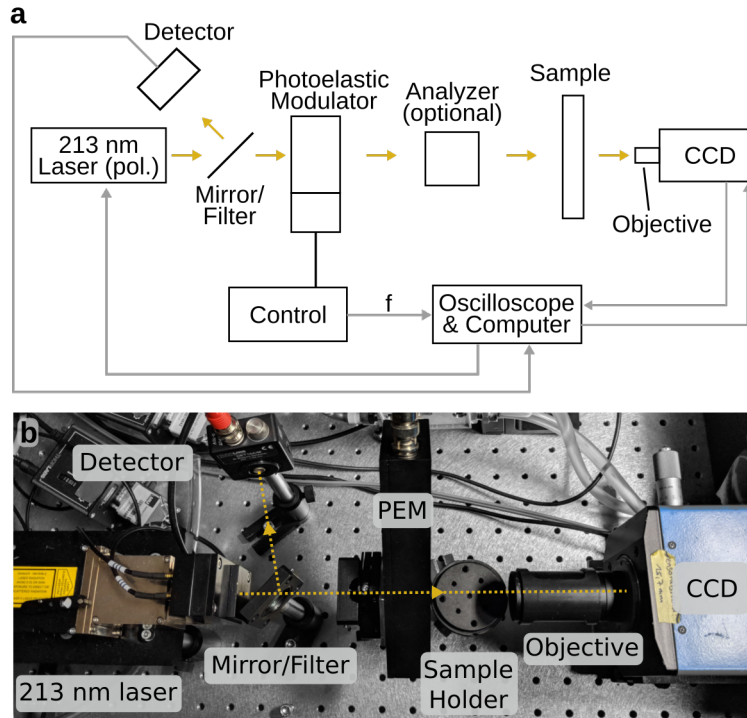
4.3.1　CDIM Setup

Figure 4.1: Circular dichroism imaging microscope. (a) Scheme of the CDIM setup. The light from the 213 nm pulsed laser has a linear, horizontally aligned polarization. It passes through a filter that eliminates remaining intensities from other wavelengths (e.g. 266 nm) and reflects approx. 70% of the incident light onto a detector. The remaining light passes through a photoelastic modulator (PEM) that is tilted by 45 degrees with respect to the direction of the laser polarization. An analyzer (linear polarizer), mounted onto a rotator, is placed behind the PEM for calibration measurements. After the light has passed through the sample, it is captured by a charge-coupled device (CCD) camper onto which an objective is mounted. The laser intensity and trigger timing is monitored by an oscilloscope attached to the detector. Laser pulses are triggered by a software-controlled signal that is modulated by the photoelastic modulator as explained in Section 4.4. **(b)** Image of the CDIM setup from above. The yellow dotted line denotes the light path from the laser to camera and detector.

Figure 4.1 shows the deep-UV circular dichroism imaging microscope. The 213 nm pulsed laser (CryLaS, FQSS213-Q4-STA, see Figure 4.2) has a maximum pulse frequency of 1 kHz. It was triggered by a software-controlled signal (see Section 4.4) in such a way that when the linearly polarized light passed through the PEM (Hinds PEM 100, I/FS50) it was circularly polarized. A 214 nm UV filter (AHF, F49-214) in front of the PEM filtered out unwanted wavelengths and reflected approx. 70% of the incident light onto a Si-detector (Thorlabs, DET10A/M) with a 1 ns rise time. The detector and PEM were connected to an oscilloscope (Agilent MSO6032A, 300 MHz), which allowed the continuous synchronization of the laser trigger and PEM frequency. After the pulse had passed through the PEM, the light was circularly polarized. It then passed through the sample and an objective (Figure 4.10) and onto the camera ("PCO Sensicam qe").

Samples could thereby be irradiated with either left or right CPL at 213 nm and simultaneously imaged. However, as the UV-sensitive camera was too sensitive to even image a single laser shot without an absorbing sample between laser and camera. As a result, I_0 could not be determined and equation 4.6 was not applicable here. It was therefore modified under the assumption that the laser intensity did not vary between two images. The CD was then determined by calculating

$$CD \ = \ \frac{I_R - I_L}{I_R + I_L}.$$ (4.7)

In the following, the main components of the setup, namely the laser and the PEM, are described in more detail.

UV Laser

According to the manufacturer, the 213 nm UV laser has a pulse to pulse stability of $< 2\%$ of the pulse energy root mean square. It has an output pulse energy of 3 µJ and an output power (in quasi cw) of 3 mW with a $> 100 : 1$ horizontal polarization. The peak power of a single pulse at 1 kHz triggering is 3.26 kW. Its full width at half maximum (FWHM) is 0.92 ns. Figure 4.2 shows the measured laser profile using a PCO Sensicam UV and a Mightex BTE-B013-UW windowless camera and the measured laser power over time using a Thorlabs PM100USB power meter with a UV-extended photo diode (S120VC). It shows that the laser profile does not exhibit a Gaussian distribution, but has several spots of higher intensity. In addition, the laser intensity varies over long periods of time and fluctuates. Therefore, single measurements were kept on the order of seconds and the direction of the CPL was changed after every image. The CD was then calculated by averaging several pairs of images over time.

Photoelastic Modulator

The photoelastic modulator (PEM) used here had a fused silica optical head with an aperture of 16 mm. It was able to achieve a quarter- and half-wave retardation of polarized light for wavelengths between 170 nm and 2 µm and 170 nm and 1 µm, respectively. The optical head was oscillating at a frequency of 50 kHz. It was thereby continuously switching between left and right CPL for a quarter-wave retardation (Figure 4.3), while also reaching all polarization states in between. The incident light was linearly polarized, with the direction of the linear polarization at an angle of 45 degrees with respect to the optical head of the PEM. Light that did not pass through the PEM at the correct time, i.e. when the retardation was not at a maximum or minimum, was either elliptically polarized or did not change in polarization (when passing through at zero retardation). As shown in Section 4.4.2, the rising and falling edge signal give the time points of maximum retardation. Data from the CD measurements of Phenylalanine shows that the rising edge gives right CPL and falling edge gives left CPL.
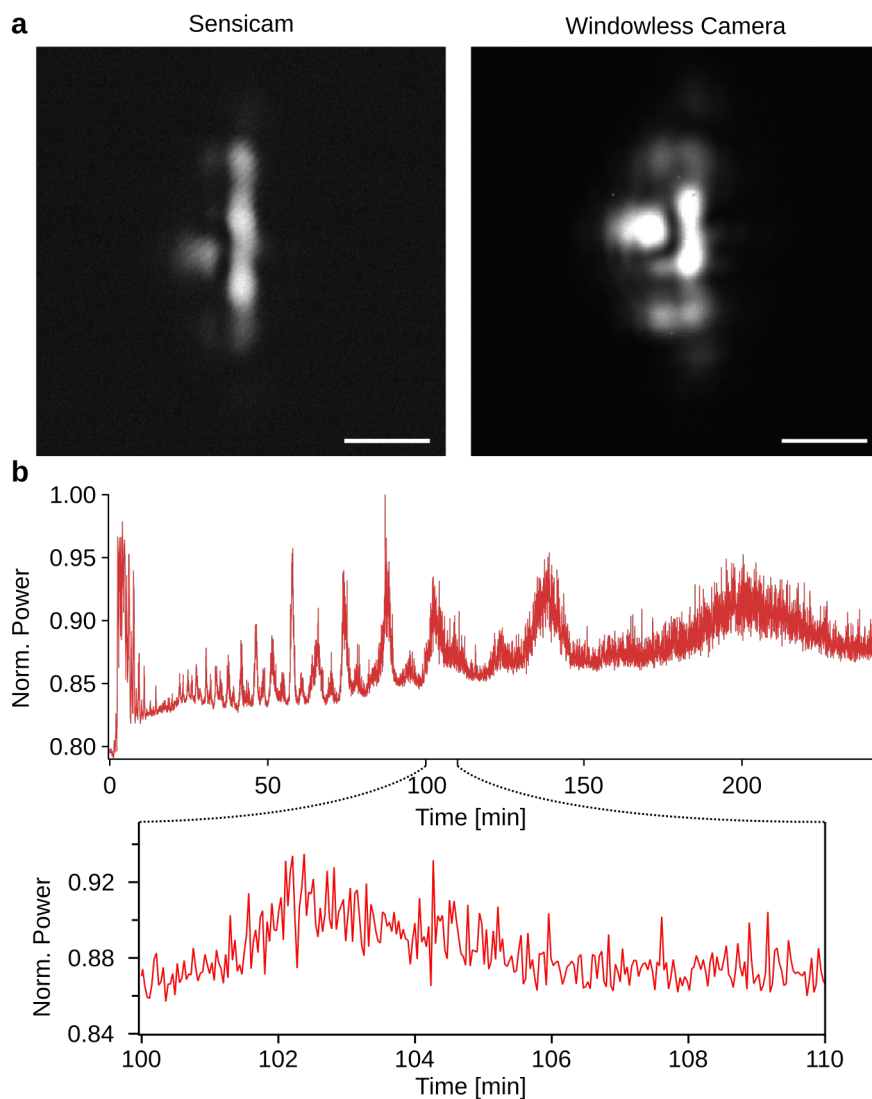
Figure 4.2: UV Laser Characteristics. (a) The 213 nm laser does not exhibit a Gaussian beam profile, but rather several intensity peaks distributed over the approximately 500 μm laser width. The left image shows the beam profile as captured by the UV-sensitive camera used in the experiments (with the beam intensity reduced by 99 %), while the right image shows the beam profile when a standard CCD camera (windowless) was used. **(b)** Normalized laser power over time. It varies on a time scale of minutes, reducing the possibility to image samples for more than a few seconds. Scale bars: 500 μm
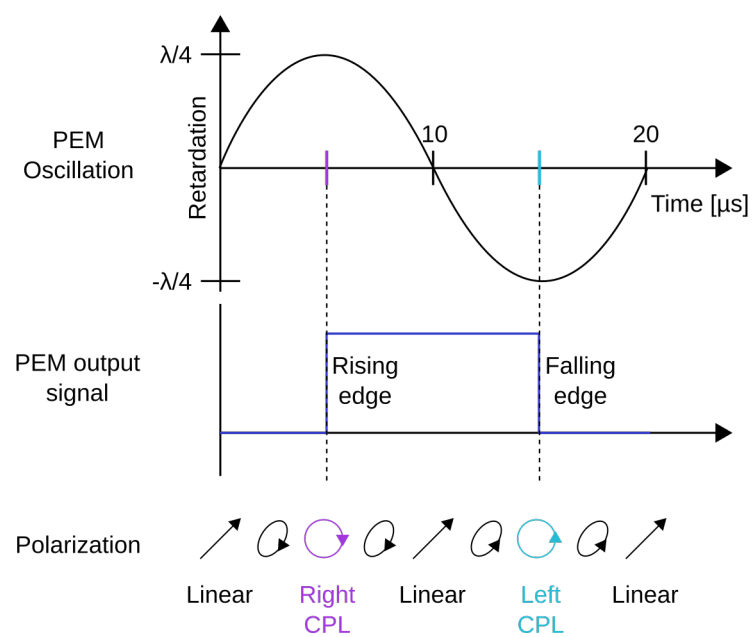
Figure 4.3: PEM mode of operation. The optical head of the PEM oscillates at a frequency of 50 kHz. When set to quarter wavelength retardation, it switches between $+\lambda/4$ (violet, right CPL) and $-\lambda/4$ (turquoise, left CPL) retardation once every 20 μs. Light passing through the PEM in between these two states will be elliptically or linearly polarized. As shown in Section 4.4.2, a maximum retardation is achieved when the PEM signal is at rising or falling edge. CD measurements from Phenylalanine indicate that the rising edge signal gives right CPL and the falling edge left CPL.

4.4 Setup Control and Calibration

The laser and PEM were synchronized as described in detail in Section 4.8.4. In short, the signal from the PEM initially triggered the laser, with an adjustable delay in between as illustrated in Figure 4.4a. This delay was varied by changing the trigger frequency f at which the laser trigger was operated. Using an oscilloscope, the delay between laser trigger and emitted pulse was monitored. Figure 4.4b shows the laser profile compared to the PEM signal as captured by the oscilloscope. It demonstrates that both could be synchronized well, with a precision of approximately 60 ns across the 20 μs time of oscillation.

4.4.1 Initial Trigger Calibration

Initially, without using the oscilloscope, the laser trigger was calibrated by gradually increasing the trigger frequency f from 61 kHz to 91 kHz, while an analyzer (see Figure 4.1) behind the PEM was rotated by 360 degrees at every frequency interval. Here, the PEM was set to quarter-wave retardation at 213 nm *via* its control unit without further calibration. The intensity measured by a power meter was then plotted (Figure 4.5). The graph shows regions of no polarization and maximum polarization (dashed lines) depending on the trigger frequency. It spans over a time delay of

$$\frac{7}{61000} - \frac{7}{91000} = 114.75 \ \mu s - 76.92 \ \mu s = 37.83 \ \mu s,$$

which is approximately two 50 kHz oscillations (see Section 4.8.4 for details). Analyzer angles have an arbitrary starting point. Since the linear increase in frequency does not correlate with a linear decrease in trigger delay time, the x-axis is slightly stretched.

When the polarization of the laser was not changed by the PEM (blue dashed lines), the light passed through the analyzer with full intensity at two given angles (60 and 240 degrees). At these angles, the analyzer direction was parallel to the horizontal laser polarization. It completely blocked the light when it was vertically aligned and therefore perpendicular to the incident light polarization at 150 and 330 degrees. When the light passing through was circularly polarized (green dashed lines), the light intensity should not have varied when the analyzer was rotated, as circularly polarized light passes through a linear polarizer (here the analyzer) at always the same intensity. However, some fluctuations in light intensity were observed. This was due to the fact that the factory settings of the PEM were not properly calibrated for deep UV, which had to be done manually (see Figure 4.6).

At low frequencies (Figure 4.5, 65 kHz), in the beginning of the calibration, strong oscillations in the signal were observed. They stem from variations in the delay between laser trigger and laser pulse, which is inherent to the laser. Therefore, from now on the laser was continuously monitored and the frequency adjusted during the following measurements.
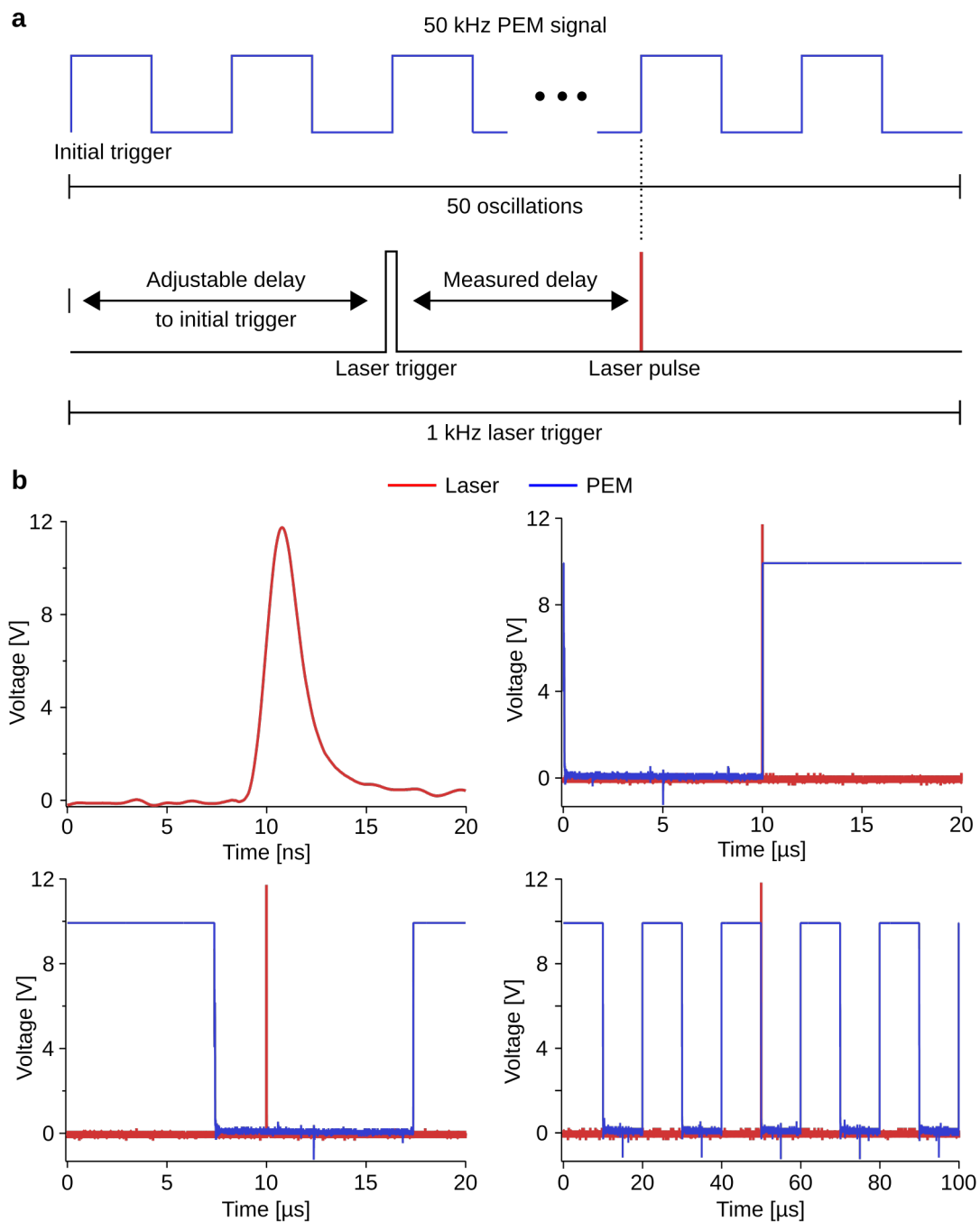
Figure 4.4: Laser trigger implementation. (a) Principles of the trigger. The PEM gave an initial rising edge signal to start the laser trigger, synchronizing the two systems. An adjustable delay to this initial signal then allowed the laser trigger to be timed correctly so that the light would pass through the PEM at the desired time. A delay after the trigger ensured that the laser pulses were fired at a maximum frequency of 1 kHz. **(b)** Measured signals. Red: laser signal from diode; blue: PEM signal. The top left graph shows the laser signal at the maximum time resolution. Top right shows both the laser and PEM signal, which was used to continuously adjust the trigger to the correct position at the PEM's rising or falling edge. Bottom left: The laser could be arbitrarily positioned at any time point with respect to the PEM. Bottom right: The laser signal shown in an array of PEM signals. It was triggered every 50 oscillations to achieve a 1 kHz trigger.
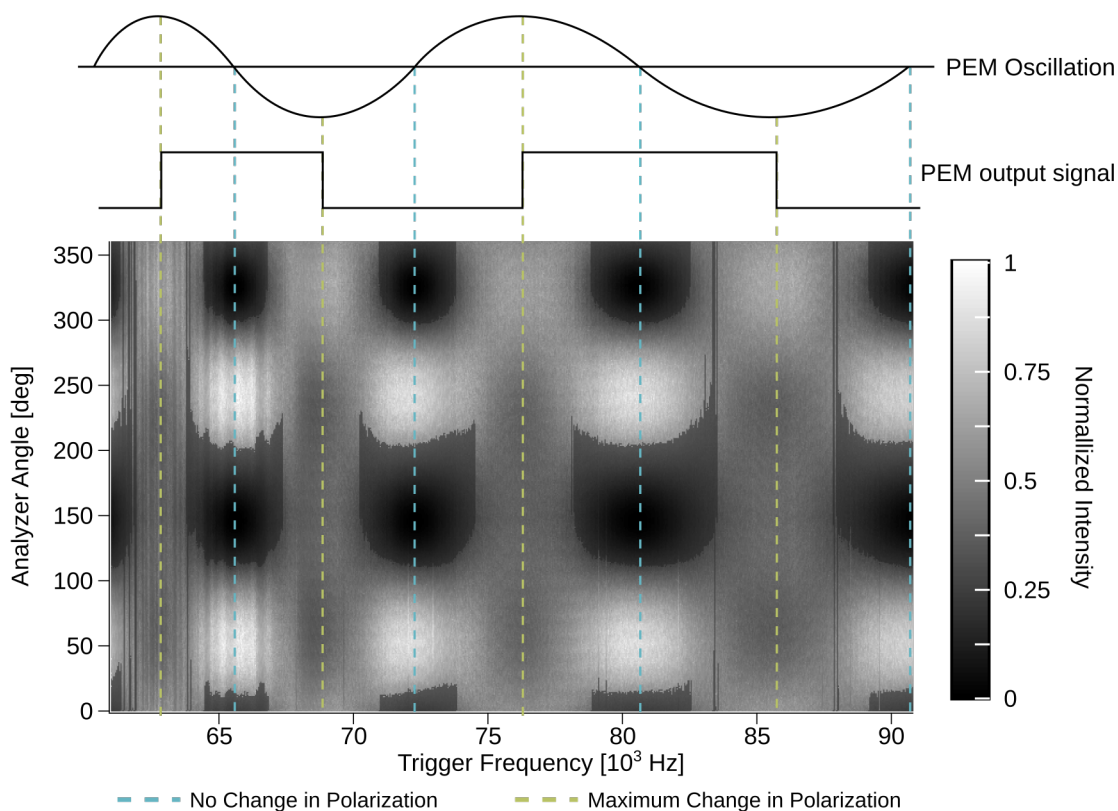
Figure 4.5: Initial trigger calibration. The image shows the measured normalized intensities at a given angle and trigger frequency. With increasing frequency, the trigger slowly went through approximately two oscillations of the PEM, illustrated above. As the trigger delay does not increase liearly with increasing frequency, the graph shows a slight stretching along the x-axis. When the trigger was timed so that the light passing through the PEM was not polarized (blue dashed lines), the light intensity shows an oscillating behavior with changing angle. It reaches a minimum and maximum intensity twice. When the light was circularly polarized, the variations in intensity decreased. In theory, they should have gone down to zero, but as described in Section 4.4.2 the light was elliptically and not perfectly circularly polarized.

4.4.2 PEM Calibration

The control unit of the photoelastic modulator defined the voltage at which the head-unit would be modulated for a given set of retardation and wavelength values. This unit was initially calibrated by the manufacturer. However, in deep UV, the factory settings greatly differed from ideal values. The PEM therefore had to be calibrated as described in [105, 106]. In short, the control voltage of the head-unit was set to a value close to what was assumed to be correct. The light's intensity was then measured after it passed through an analyzer. Depending on the desired retardation, half-wave or quarter-wave, the intensity profile then showed characteristic patterns when the delay of the laser trigger was changed (half-wave calibration) or the analyzer was rotated (quarter-wave calibration). This was repeated for different control voltages until the patterns showed the desired profile.

There were two ways to find the correct control voltage for a quarter-wave retardation at 213 nm. One approach was to find the correct value for half wave retardation and divide it by two to give the value for quarter wave retardation. In order to do so, the PEM control voltage had to be set to the assumed value for half-wave retardation and the analyzer aligned to crossing the laser polarization (rotated at 90 degrees to the horizontal axis). If the laser was continuous, this would have resulted in an oscillation of the light intensity as described in [105] and the patterns shown in Figure 4.6a. Here, as the laser was not continuous, the trigger delay had to be manually adjusted (similar as in Figure 4.5) so that the laser slowly screens through several different points along the PEM oscillation. At perfect half-wave retardation, the waveform then exhibited a flat top (black line). If the voltage was too low, the flat top vanished and the overall maximum intensity decreased (blue lines). If it was too high, the flat top turned into two maxima (orange lines). This method gave the correct voltage for a half-wave calibration of the laser at 213 nm. Knowing the voltage for a half-wave retardation (here 0.56 V) then gave the approximate value for a quarter-wave retardation by dividing the value in half (0.28 V).

The second method, which was used to then calibrate the PEM to quarter-wave retardation more precisely, required the laser pulse to be passing through the PEM at maximum retardation (rising or falling edge of the PEM signal, monitored by an oscilloscope) and the analyzer to rotate by 360 degrees (Figure 4.6b). In this setting, the PEM control voltage was varied, starting from 0.28 V. At an optimal circular polarization, the light intensity remained close to constant over the analyzer angle, as found for 0.25 V (black solid line). The black dotted line shows the signal when the initial settings of the PEM were used, indicating that here the voltage was set too high and the light was elliptically polarized.

The red interrupted line shows the waveform when the PEM was turned off, and the red solid line when the trigger was set to a 5 µs delay compared to the trigger at the rising or falling edge (i.e. in the middle of the PEM signal between rising and falling edges). The two overlap, which shows that no retardation was achieved when light passed through the PEM at this moment (compare Figure 4.3, linear polarization). From this it follows that the maximum retardation was indeed achieved when the laser pulse passed through the PEM when its control unit gave a rising or falling edge output signal.
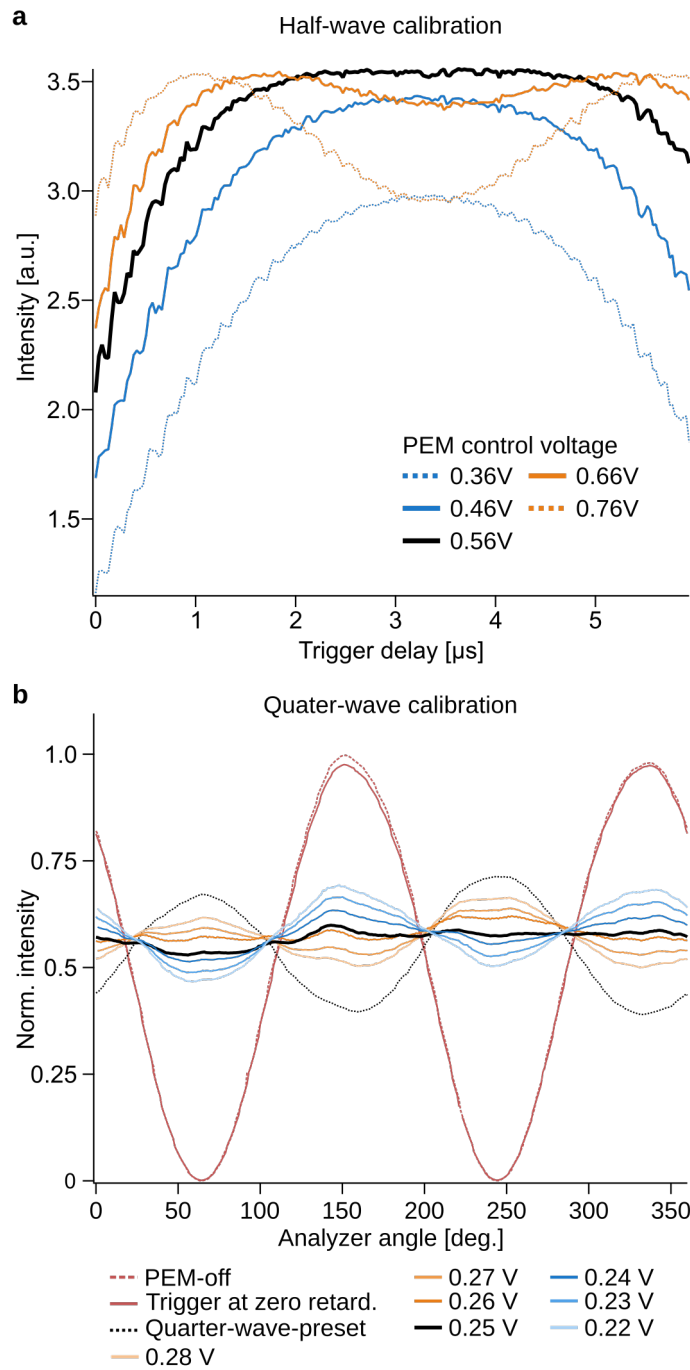
Figure 4.6: PEM calibration. (a) Half-wave calibration. The PEM was set to a voltage close to half-wave retardation and an analyzer was placed behind it at 90 degrees with respect to the horizontal laser polarization. The trigger delay was then varied to screen through different laser pulse delays. The intensity measured behind the analyzer showed several characteristic waveforms. A perfect half-wave calibration exhibited a flat top (black line). If the voltage was too low the flat top vanished (blue lines) and lost in overall intensity; if it was too high, the flat top turned into two peaks (orange lines). The value for half-wave retardation (0.56 V) divided by two gave a starting value for a quarter-wave retardation (0.28 V). **(b)** Quarter-wave calibration. The setup was set to achieve a maximum retardation of the laser pulse, while the analyzer was rotated by 360 degrees. Varying the voltage gave the setting for quarter-wave retardation when the intensity did not change over the angle (black solid line). The black dotted line shows the intensity using the factory settings for a 213 nm quarter-wave retardation. When the PEM was off (red interrupted line) or the trigger was set in between rising and falling edges of the PEM signal (red solid line), the polarization was not changed.

4.5 CD results

4.5.1 Phenylalanine

As a test of the system, the absorbance of a molecule was measured that showed a comparatively large CD at 213 nm for its two enantiomers. This was the case for L- and D-Phenylalanine (L-Phe and D-Phe, respectively). The two enantiomers have opposite CD values between wavelengths of 200 nm and 220 nm (Figure 4.7a for L-Phe, D-Phe analogue with negative $\Delta\epsilon$, in agreement with literature values [107]). For the example measurement shown in Figure 4.7, a 2 mM solution of L-Phe was filled in a cuvette (path length 3 mm) and placed in front of the camera. This concentration was chosen as it showed the best signal to noise ratio in this setup. The analyzer used during the calibration measurements was removed. The laser was then turned on and run warm for a few minutes. Laser and camera triggers were synchronized so that the number of shots per image could be controlled and the light was circularly polarized. Here, it was important not to oversaturate the camera.

As a next step the PEM control voltage was set to 0.25 V. Laser-PEM synchronization was monitored using an oscilloscope connected to a computer. This allowed a continuous and automated re-calibration of the trigger delay during the experiments. In addition, the maximum of each laser peak was recorded by the oscilloscope in order to monitor changes in the laser intensity. Although the oscilloscope had an up to 300 MHz repetition rate, the connection to the computer slowed down the maximum detection speed and the laser could only be triggered with a maximum frequency of 15 Hz.

During the experiment shown here, the laser was shot 30 times for each image. For the first image, the pulse was adjusted to coincide with a falling edge of the PEM, for the second to coincide with a rising edge. In a next step the trigger was adjusted in case it became slightly asynchronous based on data from the oscilloscope. After this, the next set of images was recorded and the cycle continued several hundred times.

Images were analyzed using a self-written Labview program. It calculated the mean intensity for a given region of interest in each image (Figure 4.7b, "Mean 1" for falling edge triggered images, "Mean 2" for rising edge) after subtracting a dark background from it. These mean values were then divided by the laser intensity as measured in the oscilloscope, although this did not noticeably change the results. For each pair of images, the software then calculated

$$\text{CD} = \frac{\text{Mean 1} - \text{Mean 2}}{\text{Mean 1} + \text{Mean 2}}. \tag{4.8}$$

according to Equation 4.7. The results are shown in Figure 4.7c. It is the calculation from Equation 4.8 for every pair of images. In theory, the intensity should be constant over time. However, it can be seen that the signal oscillated strongly. The origin of this oscillation was difficult to locate but was likely due to overall laser intensity oscillations. This made it more difficult to determine a mean value (see Section 4.6, Discussion). Measurements for D-Phenylalanine were analogue.

Figure 4.8 shows the mean CD values of several measurements for D-Phenylalanine, L-Phenylalanine, and a 1:1 mixture of both. Since I_0 could not be determined, the CD value calculated from the measurements here only gives the sign of the CD. A determination of
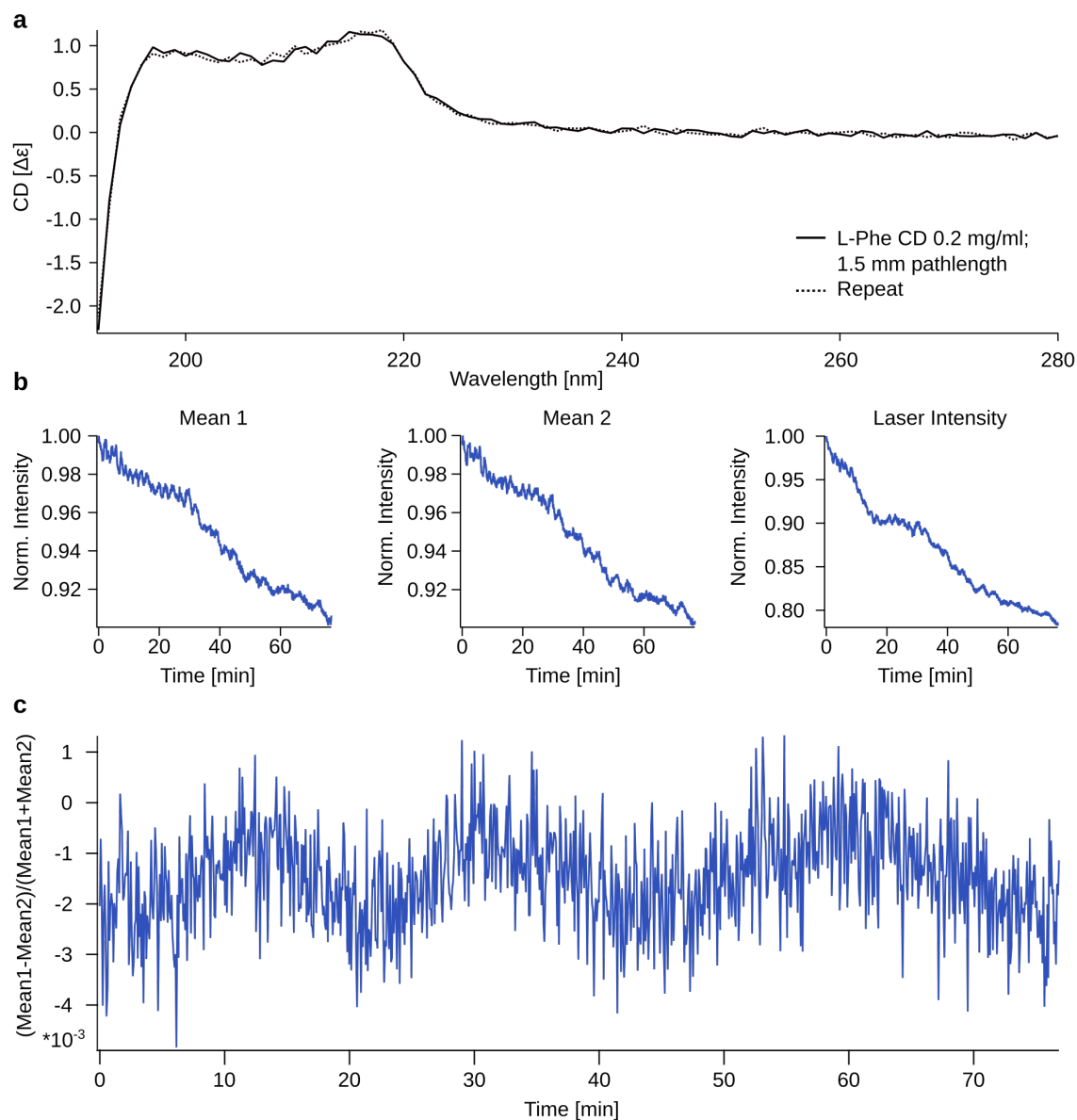
Figure 4.7: L-Phenylalanine measurement. **(a)** CD spectrum of L-Phenylalanine. It shows a peak between approx. 200 nm and 220 nm. For L-Phe, $\Delta\epsilon$ is positive at 213 nm, for D-Phe it is negative (see [107]) The data is consistent with literature values. **(b)** Mean values determined in the experiment for each image. Mean 1 shows the images that were triggered on a falling edge, Mean 2 on a rising edge. In addition, the maxima of each waveform detected from the laser shots were recorded and the mean values for each image plotted. **(c)** CD calculation. The CD was calculated according to Equation 4.8.

$\Delta\epsilon$ was not possible. In theory, the CD for the 1:1 mix should be zero, but is slightly positive here. This could be from pipetting errors or variations in laser intensity during the measurement. However, a difference between pure D-Phe and L-Phe could still be found, with the CD for D-Phe being positive and for L-Phe negative.

From this, the direction of the polarized light can be determined as follows. For L-Phe, ΔA, i.e. A_L-A_R, is positive. As here the CD was calculated by subtracting laser intensity triggered on a falling edge from laser intensity triggered on a rising edge, with intensity being inverse to the absorbance A, the sign from the CD calculated here would be inverse to the measured ΔA. As here the sign of L-Phe is negative, which matches the positive ΔA, this means that also here the intensity from left CPL was subtracted from right CPL. It follows that a rising edge of the PEM signal gave right CPL while a falling edge gave left CPL, as expected.
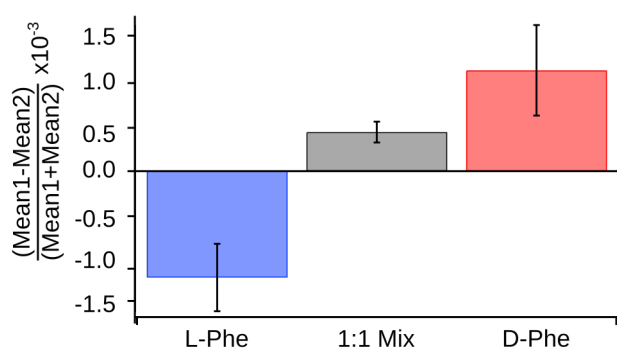

Figure 4.8: CD results of Phenylalanine in pure water. Measurements here only give the sign of the CD, with D-Phe being positive and L-Phe negative. A 1:1 mix of L-Phe and D-Phe shows a slight positive tendency.

4.5.2 Ribose Aminooxazoline

The RNA precursor ribose aminooxazoline (RAO), part of the RNA nucleotide synthesis pathway found by Powner et al. [76], crystallizes in homochiral domains [74]. This process, enhanced by the presence of an enantiomeric excess of amino acids [97], could thereby have initiated a chiral selection step at an early stage during the origin of life. It was therefore of interest to see if the sign of the CD of ribose aminooxazoline could be determined as well.

Figure 4.9a shows the absorbance of RAO in the deep UV. It peaks around 210 nm at a concentration of 3.6 mM and a path length of 3 mm. However, the CD of D-RAO at 213 nm is very small ($\Delta\epsilon = -0.04$, Figure 4.9b) compared to Phenylalanine ($\Delta\epsilon = 1$). At high concentrations in water, RAO quickly forms crystals [73, 74]. Figure 4.9c shows such a crystal that grew in a 200 μm thick capillary. The capillary was therefore filled with an RAO solution saturated at 70 °C (approx. 110 μM), put in a polystyrene box, and slowly cooled down in the fridge. This induced the growth of several crystals inside the capillary. A CD measurement of an RAO crystal was, however, not performed as it was difficult to grow large enough crystals to cover the whole beam spot. For smaller cystals reflections from the beam interfered with the measurement. Measurements in water, however, showed that also for RAO a difference between the L- and D-enantiomer could

be found (Figure 4.9d). The signs found here, positive for D-RAO and negative for L-RAO, match the Phenylalanine measurements. For these measurements, RAO was saturated at room temperature, after which the supernatant was heated to 70 °C in order to dissolve any crystals in the mixture. For the measurement the sample was mixed with water at a ratio of approximately 2:1 in a 3 mm path length cuvette.
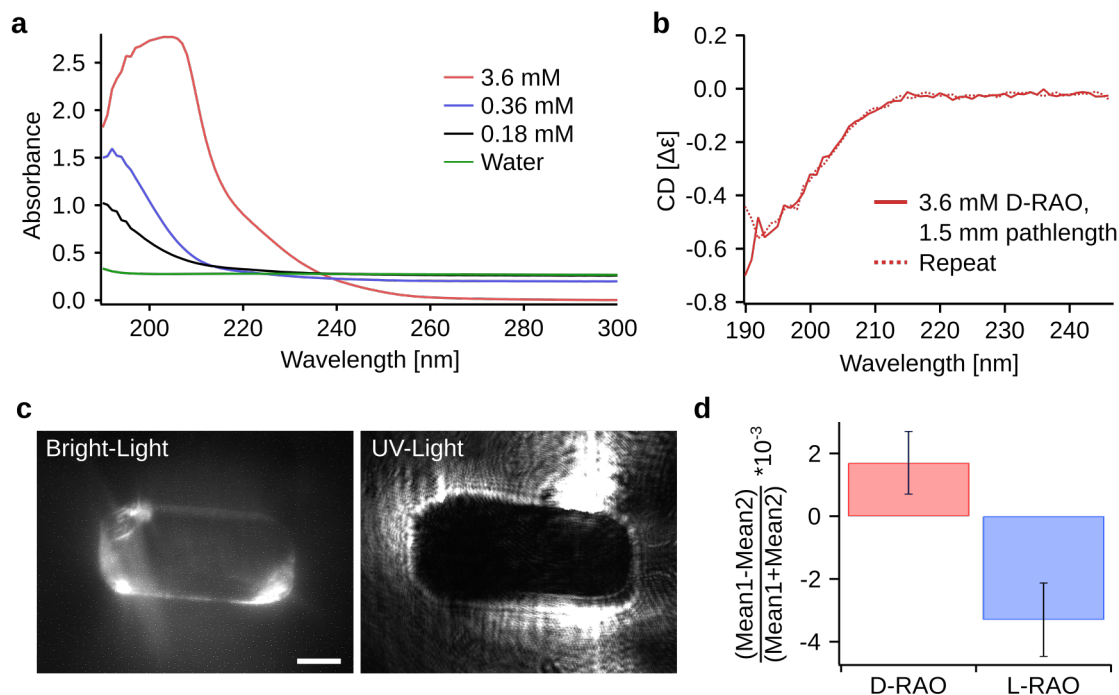

Figure 4.9: Absorbance and CD of RAO. (a) Absorbance of RAO at different concentrations against wavelength. The light path length is 3 mm. **(b)** CD spectrum of D-RAO at a concentration of 3.6 mM and a light path length of 1.5mm. At 213 nm, $\Delta\epsilon$ is -0.04.**(c)** Images of an RAO crystal. Left: Bright-Light image of the crystal using the 10x objective in the here described setup. Right: The same crystal under 213 nm UV light illumination from behind. The crystal is approx. 400 μm wide and grew in a 200 μm thick capillary from an RAO solution saturated at 70 °C (ca. 110 mM). Scale bar: 100 μm.**(d)** CD measurement of D- and L-RAO in the here built setup. Samples were saturated at room temperature and measured in a 3 mm path length cuvette.

4.6 Discussion

The setup described here allows a good control over the light polarization and the synchronization between PEM and the laser. However, calculating the CD of a sample or determining whether $\Delta\epsilon$ is positive or negative has proven challenging in deep UV.

A major challenge for the CD calculation was that the camera used here was too sensitive to image even a single laser shot without an absorbing medium in between. This made it difficult to track the variations of the laser power over time and the intensity I_0 of the incident light, without sample, could not be determined. Tracking the intensity *via* the detector at a good resolution was, unfortunately, also not possible, as the 5 ns long waveform (see Figure 4.4b) had to be monitored simultaneously with the rising or falling edge of the PEM. This required a time span of several milliseconds to be tracked and reduced the resolution of the peak detection. It only allowed monitoring an average of all laser peaks detected per image (the time resolution of the oscilloscope was chosen so that every laser shot could still be captured, however the full waveform could not be resolved and only the maximum values of the detected peaks were traced, which not necessarily coincided with the waveform maximum). This method gave an estimate of the laser intensity over time, however an integration of the waveform area would have been desirable to properly track the laser power.

In addition, Figure 4.7c shows strong oscillations in the calculated CD value over time. The source of these oscillations could not be determined. Several aspects such as laser-, PEM-, camera sensor-, and sample temperature (too warm or too cold), laser power stability, or possible effects of a linear absorbance of the cuvette and other parts of the system were checked, but a definitive source of error could not be found. The most likely source is however the variation of laser power over time.

Due to the limitations in the detection, the setup did not operate at an optimal signal to noise ration for absorbance measurements. In an optimized system with no measurement artifacts, the ideal conditions can be estimated as follows: The signal to noise ratio for the optical depth $A_e = ln(\frac{I_0}{I_t})$ of a material, with I_t the transmitted light intensity after it passed through the sample, can be estimated by the following calculation (adapted from [108]):

$$\frac{\partial A_e}{\partial I_0} = (\frac{I_o}{I_t})^{-1}(\frac{\partial(\frac{I_0}{I_t})}{\partial I_0}) = \frac{I_t}{I_0}\frac{1}{I_t} = \frac{1}{I_0} \tag{4.9}$$

and similarly,

$$\frac{\partial A_e}{\partial I_t} = \frac{-1}{I_t} \tag{4.10}$$

The error can then be calculated by:

$$(\partial A_e)^2 = (\frac{\partial A_e}{\partial I_0}dI_0)^2 + (\frac{\partial A_e}{\partial I_t}dI_t)^2 = (\frac{1}{I_0}dI_0)^2 + (\frac{1}{I_t}dI_t)^2 = \frac{1}{I_0^2}(dI_0)^2 + \frac{1}{I_0^2}\exp(2A_e)(dI_0)^2 \tag{4.11}$$

with $I_t = I_0\exp(-A_e)$. Assuming the same noise for all measurements $dI_0 = dI_t = dN$ then gives

$$(\partial A_e)^2 = \frac{(dN)^2}{I_0^2}(1 + \exp(2A_e)) \tag{4.12}$$

The signal to noise ratio is then:

$$\frac{\partial A_e}{A_e} = \frac{dN}{I_0} \frac{\sqrt{1 + \exp(2A_e)}}{A_e}. \tag{4.13}$$

The function $\frac{\sqrt{1+\exp(2A_e)}}{A_e}$ has a minimum for an optical depth of $A_e \approx 1.1$. It can be converted into absorbance by calculating $A = \frac{A_e}{ln(10)}$. The signal to noise ratio for an absorbance measurement therefore has a minimum at $A \approx 0.48$.

In case of RAO in solution, this would require a concentration of approx. 0.4 mM for a path length of 3 mm (see Figure 4.9). For these values, Equation 4.5 gives a difference in absorbance of left and right circularly polarized light of $\Delta A \approx 5 * 10^{-6}$. The relation $A = log(\frac{I_0}{I_t})$ and Equation 4.5 then give: $\frac{I_R}{I_L} = 1.00001$. The difference between I_R and I_L is therefore at least two orders of magnitude smaller than the error in our measurements (Figures 4.7c) if the optimal signal to noise ratio was chosen.

In addition, imaging an RAO crystal, the purpose of this setup, with an absorbance of 0.48, would, unfortunately, be nearly impossible. Based on crystallography data (see Chapter 3), the density of an RAO crystal is approx. 1.6 g/cm^3. This translates to a concentration of 9.2 M (MW [molecular weight] of RAO: 174.16). The absorbance of RAO for a concentration of 0.36 mM and a path length of 3 mm is 0.37. Using the relation $A = \epsilon Cl$ then shows that a crystal would have to be only 0.15 µm thick (and at the same time at least 200 $* 200$ μm^2 large to image it properly) to have an absorbance of 0.48. Unfortunately, these dimensions are virtually impossible to grow in solution without extended control mechanisms.

The calculations above are for an ideal system that is optimized for signal to noise and can measure I_0. It is therefore of limited applicability for the setup described in this chapter. However, the calculations give a hint as to why the CD measurements in this setup were error prone. In addition to the measurement artifacts described above, the setup operated far from an ideal signal to noise ratio. Instead, the aim here was to capture as much difference in absorbance as possible by optimizing the signal of each measurement. Sample concentrations were therefore chosen to best fit the system. Analyzing crystals would, however, likely suffer from this low signal to noise as their size is difficult to optimize, and they require long exposure times of the samples while the laser intensity was varying over time.

4.7 Conclusion

Figure 4.6b suggests that circularly polarized light could be produced to a reasonable extent and the control over the polarization was good. Measurements of chiral molecules in solution showed that the sign of the CD could potentially be determined for pure samples. This might, however, prove challenging for mixed solutions and crystals. Furthermore, the limited detection range of the CCD camera prevented a measurement of I_0 and therefore of $\Delta\epsilon$. Variations of laser intensity likely resulted in measurement artifacts and further experiments would be needed to clarify these. However, the advantage of the here presented setup is the creation of circularly polarized light with a good control over

the polarization. If desired, left or right CPL could be created without unwanted elliptically polarized light and on arbitrary timescales. This system could easily be extended to a wide range of wavelengths by using a tunable laser, since the PEM can be operated between 170 nm and 2000 nm.

4.8 Materials and Methods

4.8.1 Chemicals and Instruments

Phenylalanine was bought from Sigma Aldrich (L-Phe: #P2126, D-Phe #P1751) and measured in pure water as done in the literature [107]. CD measurements were performed in a Chirascan Circular Dichroism Spectrometer (Applied Photophysics) with Hellma Analytics High Precision Cells made from Quartz Suprasil (e.g. #105-251-15-40). A similar cell (#105-254-15-40) was used in the CD Setup measurements. RAO was obtained from the Powner Group (UCL, London, UK) in both D- and L- version. Absorbance was measured in a Jasco V-650 UV-Vis spectrometer.

4.8.2 Measurement Procedure

Measurements in the CD setup were performed as follows. All system components were turned on and kept running for a few minutes. This allowed the CCD to cool down the chip and the laser to power up. Samples were then mixed and filled in the cuvette. The concentration was adjusted to best fit the system; a too low concentration had a high signal to noise ratio and required only a few laser shots to saturate the camera. If the concentration was too high the laser profile could not be seen anymore and the long exposure time caused light reflections to oversaturate the sensitive CCD chip. Initially, the laser was kept running with a closed shutter to allow it to stabilize. During the measurements the maximum of each detected laser peak was recorded and an average of all peaks per image was calculated. At the same time the trigger frequency was adjusted after each pair of images to best fit the PEM signal. This avoided a migration of the laser peak relative to the PEM oscillations over time. Samples were illuminated alternately with light that passed through the PEM at a falling and rising edge, respectively. The system was controlled using a LabView 2014 control VI with a National Instruments 6229 PCI card.

4.8.3 UV Objectives

In order to potentially image crystals, two UV-compatible objectives were used (Figure 4.10). A 2-fold and a 10-fold objective, which were specifically designed using Win-Lens [109]. They were composed of UV fused silica lenses, the respective lens product numbers (Thorlabs) are given in the drawing.

4.8.4 Triggering

The PEM was oscillating at a frequency of 50 kHz, which had to be synchronized to the laser pulse in order to achieve a constant time delay between PEM and laser pulse and thereby a constant polarization of the light. The PEM control unit gave the exact frequency at which it was oscillating as an output. This signal was used to control the laser trigger *via* a National Instruments 6229 PCI card. The laser trigger itself was an analogue output signal of this PCI card that used the PEM frequency as a timebase.
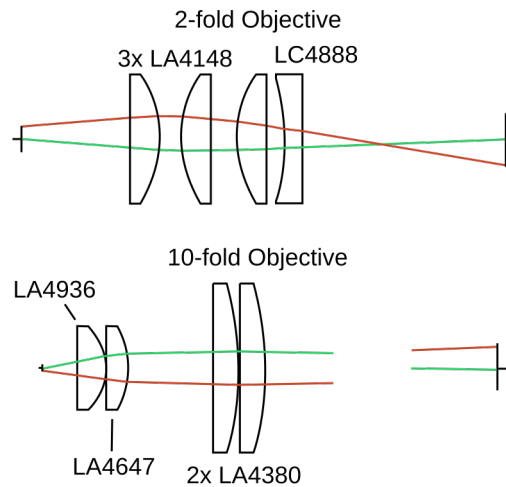
Figure 4.10: UV Objectives. Top: 2-fold objective. Working distance: 21.4 mm, numerical aperture 0.018. Bottom: 10-fold objective. Woking distance 5.2 mm, numerical aperture 0.022. The numbers in the figure are the product codes from the manufacturer (Thorlabs).

The principle of how the trigger was operated is shown in Figure 4.11. Varying not the position of the actual signal along the trigger array, but the frequency at which it was operated, allowed a very precise control over the trigger delay.
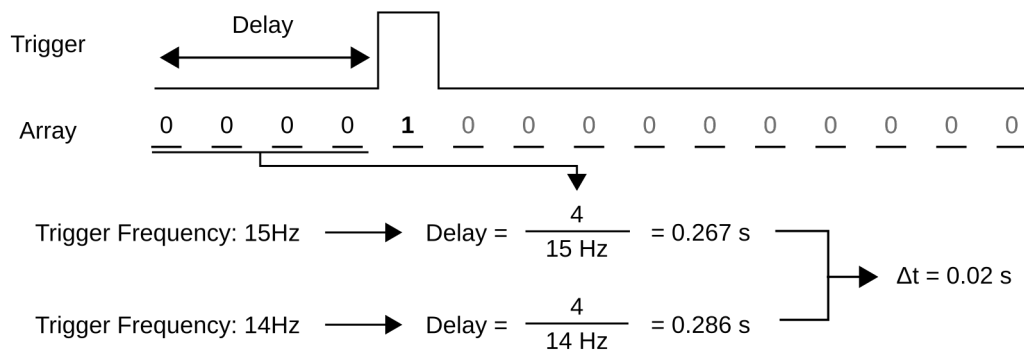
Figure 4.11: Principles of the trigger mechanism. The laser trigger was an analogue voltage output signal. It can be depicted as an array of zeros with a single one at a certain position. Once activated, the trigger would then stay at zero voltage for a specified delay, calculated by the number of zeros before the trigger signal and the trigger frequency. This delay could be fine-tuned not by changing the position of the signal along the array, which would be far less precise, but by changing the frequency at which the trigger operated. After the delay had passed, the PCI card increased the signal voltage and a laser pulse was fired. Here, the laser trigger was operated at a frequency between 50 kHz and 100 kHz, allowing a very precise control over the trigger delay.

Once the laser trigger was armed, the first rising edge signal from the PEM was used as an initial trigger, synchronizing the two systems (Figure 4.4). This started the trigger signal of the PCI card, which could be modulated at a maximum frequency of 100 kHz. Usually, this would not be enough to fine-tune the delay between initial PEM trigger and laser pulse, as it is only twice the PEM oscillation frequency. The goal, however,

was to arbitrarily set the delay between initial PEM trigger and firing of the laser pulse. Therefore, one would want a number of at least 40 possible intervals within the 50 kHz (20 μs) waveform of the PEM. If the maximum trigger frequency of approx. 100 kHz were used, the time between two positions in this trigger would be $1/(100000 Hz) = 10\ \mu s$, not short enough to vary the delay between trigger and laser pulse fine enough. Therefore, a different solution was implemented. Instead of varying the position of the signal along the trigger, it was kept constant (in this case at position 8 of the trigger array) but the frequency with which it was fired was changed. This frequency could be varied with step sizes of approximately 50 Hz. Therefore, firing this trigger at 75 000 Hz and increasing to 75 050 Hz then gave a time difference between the two triggers of

$$\frac{7}{75000} - \frac{7}{75050} = 93.333\ \mu s - 93.271\ \mu s = 62.2\ ns \tag{4.14}$$

with seven trigger positions at zero voltage before the signal itself at position eight. The difference varies slightly when using different frequencies, of course, however, it still gives well over 300 possible intervals within the 20 μs range. This is enough to fine-tune the signal.

The whole trigger with the adjustable delays, before and after the signal, had to be long enough to span over 50 oscillations of the PEM. Figure 4.4a shows the principles of this. This had to be done as the laser would shut down if it received a trigger signal faster than at a 1 kHz rate. The delay between laser trigger and laser shot was approximately 124 μs as measured by the detector. This delay, however, varied over time, which is why the trigger frequency had to be adjusted continuously.

Figure 4.4b shows the signals from the detector and PEM. The detector had a rise time of $< 1\ ns$ and therefore registered laser pulses fast enough with respect to the 20 μs PEM signal that no additional delay had to be considered. It can be seen that the laser-PEM time relation could be resolved with good accuracy and the laser precisely positioned at the rising or falling edge of the PEM.

Importantly, the intensity of the laser varied slightly depending on the trigger frequency. If two different frequencies, i.e. two different delays, were now used to position the trigger at a rising or falling edge, one would have to correct the results for an additional source of error. Therefore, to have the same frequency for both rising and falling edge triggers, the trigger structure itself (number of trigger points, frequency of the trigger) was kept constant but the initial trigger (see Figure 4.4a) was changed between rising and falling edge of the PEM signal. This allowed the exact same trigger to shift by half of a PEM oscillation on demand.

Bibliography

[1] Allen P. Nutman, Vickie C. Bennett, Clark R. L. Friend, Martin J. van Kranendonk, and Allan R. Chivas. Rapid emergence of life shown by discovery of 3,700-million-year-old microbial structures. *Nature*, 537(7621):535, 2016. ISSN 0028-0836. doi: 10.1038/nature19355.

[2] Abigail C. Allwood, Malcolm R. Walter, Ian W. Burch, and Balz S. Kamber. 3.43 billion-year-old stromatolite reef from the pilbara craton of western australia: Ecosystem-scale insights to early life on earth. *Precambrian Research*, 158(3-4): 198–227, 2007. ISSN 03019268. doi: 10.1016/j.precamres.2007.04.013.

[3] Steven A. Benner. Defining life. *Astrobiology*, 10(10):1021–1030, 2010. ISSN 1531-1074, 1557-8070. doi: 10.1089/ast.2010.0524.

[4] Erwin Schrödinger. *What is life? The physical aspect of the living cell.* University Press and The Macmillan Co, Cambridge [England] and New York, 1944.

[5] Ben K. D. Pearce, Ralph E. Pudritz, Dmitry A. Semenov, and Thomas K. Henning. Origin of the rna world: The fate of nucleobases in warm little ponds. *Proceedings of the National Academy of Sciences of the United States of America*, 114(43):11327–11332, 2017. ISSN 0027-8424. doi: 10.1073/pnas.1710339114.

[6] Leslie E. Orgel. Prebiotic chemistry and the origin of the rna world. *Critical Reviews in Biochemistry and Molecular Biology*, 39(2):99–123, 2004. ISSN 1040-9238. doi: 10.1080/10409230490460765.

[7] R. Lohrmann and L. E. Orgel. Urea-inorganic phosphate mixtures as prebiotic phosphorylating agents. *Science (New York, N.Y.)*, 171(3970):490–494, 1971. ISSN 0036-8075.

[8] Matthias Morasch, Christof B. Mast, Johannes K. Langer, Pierre Schilcher, and Dieter Braun. Dry polymerization of 3',5'-cyclic gmp to long strands of rna. *ChemBioChem*, 15(6):879–883, 2014. ISSN 14394227. doi: 10.1002/cbic.201300773.

[9] M. S. Verlander, R. Lohrmann, and L. E. Orgel. Catalysts for the self-polymerization of adenosine cyclic 2ʹ,3ʹ-phosphate. *Journal of Molecular Evolution*, 2(4):303–316, 1973. ISSN 0022-2844. doi: 10.1007/BF01654098.

[10] M. Levy and S. L. Miller. The stability of the rna bases: Implications for the origin of life. *Journal of the American Chemical Society*, 95(14):7933–7938, 1998. ISSN 1520-5126. doi: 10.1073/pnas.95.14.7933.

[11] Victor Sojo, Barry Herschy, Alexandra Whicher, Eloi Camprubí, and Nick Lane. The origin of life in alkaline hydrothermal vents. *Astrobiology*, 16(2):181–197, 2016. ISSN 1531-1074, 1557-8070. doi: 10.1089/ast.2015.1406.

[12] Philipp Baaske, Franz M. Weinert, Stefan Duhr, Kono H. Lemke, Michael J. Russell, and Dieter Braun. Extreme accumulation of nucleotides in simulated hydrothermal pore systems. *Proceedings of the National Academy of Sciences of the United States of America*, 104(22):9346–9351, 2007. ISSN 0027-8424. doi: 10.1073/pnas.0609592104.

[13] Michael J. Russell, Roy M. Daniel, and Allan J. Hall. On the emergence of life via catalytic iron-sulphide membranes. *Terra Nova*, 5(4):343–347, 1993. ISSN 0954-4879. doi: 10.1111/j.1365-3121.1993.tb00267.x.

[14] William Martin and Michael J. Russell. On the origins of cells: a hypothesis for the evolutionary transitions from abiotic geochemistry to chemoautotrophic prokaryotes, and from prokaryotes to nucleated cells. *Philosophical Transactions of the Royal Society B: Biological Sciences*, 358(1429):59–83; discussion 83–5, 2003. ISSN 0962-8436. doi: 10.1098/rstb.2002.1183.

[15] Nicholas T. Arndt and Euan G. Nisbet. Processes on the young earth and the habitats of early life. *Annual Review of Earth and Planetary Sciences*, 40(1):521–549, 2012. ISSN 0084-6597. doi: 10.1146/annurev-earth-042711-105316.

[16] Laura M. Barge, Yeghegis Abedian, Michael J. Russell, Ivria J. Doloboff, Julyan H. E. Cartwright, Richard D. Kidd, and Isik Kanik. From chemical gardens to fuel cells: Generation of electrical potential and current across self-assembling iron mineral membranes. *Angewandte Chemie (International ed. in English)*, 54(28):8184–8187, 2015. ISSN 1521-3773. doi: 10.1002/anie.201501663.

[17] M. J. Russell, A. J. Hall, and W. Martin. Serpentinization as a source of energy at the origin of life. *Geobiology*, 8(5):355–371, 2010. doi: 10.1111/j.1472-4669.2010.00249.x.

[18] Nick Lane and William F. Martin. The origin of membrane bioenergetics. *Cell*, 151 (7):1406–1416, 2012. ISSN 00928674. doi: 10.1016/j.cell.2012.11.050.

[19] Doreen Niether, Dzmitry Afanasenkau, Jan K. G. Dhont, and Simone Wiegand. Accumulation of formamide in hydrothermal pores to form prebiotic nucleobases. *Proceedings of the National Academy of Sciences of the United States of America*, 113 (16):4272–4277, 2016. ISSN 1091-6490. doi: 10.1073/pnas.1600275113.

[20] C. B. Mast, S. Schink, U. Gerland, and D. Braun. Escalation of polymerization in a thermal gradient. *Proceedings of the National Academy of Sciences of the United States of America*, 110(20):8030–8035, 2013. ISSN 0027-8424. doi: 10.1073/pnas.1303222110.

[21] Lorenz M. R. Keil, Friederike M. Möller, Michael Kieß, Patrick W. Kudella, and Christof B. Mast. Proton gradients and ph oscillations emerge from heat flow at the microscale. *Nature Communications*, 8(1):1897, 2017. ISSN 2041-1723. doi: 10.1038/s41467-017-02065-3.

[22] Moritz Kreysing, Lorenz Keil, Simon Lanzmich, and Dieter Braun. Heat flux across an open pore enables the continuous replication and selection of oligonucleotides towards increasing length. *Nature Chemistry*, 7(3):203–208, 2015. ISSN 1755-4330, 1755-4349. doi: 10.1038/nchem.2155.

[23] Itay Budin, Raphael J. Bruckner, and Jack W. Szostak. Formation of protocell-like vesicles in a thermal diffusion column. *Journal of the American Chemical Society*, 131(28):9628–9629, 2009. ISSN 0002-7863. doi: 10.1021/ja9029818.

[24] George M. Church, Yuan Gao, and Sriram Kosuri. Next-generation digital information storage in dna. *Science*, 337(6102):1628, 2012. ISSN 0036-8075, 1095-9203. doi: 10.1126/science.1226355.

[25] Victor A. Bloomfield. Dna condensation by multivalent cations. *Biopolymers*, 44 (3):269–282, 1997. ISSN 0006-3525.

[26] Guan-Ying Li, Rui-Lin Guan, Liang-Nian Ji, and Hui Chao. Dna condensation induced by metal complexes. *Coordination Chemistry Reviews*, 281:100–113, 2014. ISSN 00108545. doi: 10.1016/j.ccr.2014.09.005.

[27] Björn Drobot, Juan M. Iglesias-Artola, Kristian Le Vay, Viktoria Mayr, Mrityunjoy Kar, Moritz Kreysing, Hannes Mutschler, and T-Y Dora Tang. Compartmentalised rna catalysis in membrane-free coacervate protocells. *Nature Communications*, 9 (1):3643, 2018. ISSN 2041-1723. doi: 10.1038/s41467-018-06072-w.

[28] David P. Horning and Gerald F. Joyce. Amplification of rna by an rna polymerase ribozyme. *Proceedings of the National Academy of Sciences of the United States of America*, 113(35):9786–9791, 2016. ISSN 0027-8424. doi: 10.1073/pnas.1610103113.

[29] Christine C. Conwell, Igor D. Vilfan, and Nicholas V. Hud. Controlling the size of nanoscale toroidal dna condensates with static curvature and ionic strength. *Proceedings of the National Academy of Sciences of the United States of America*, 100 (16):9296–9301, 2003. ISSN 0027-8424. doi: 10.1073/pnas.1533135100.

[30] Lerman L. S. A transition to a compact form of dna in polymer solutions. *Proceedings of the National Academy of Sciences of the United States of America*, 68(8):1886–1890, 1971. ISSN 0027-8424.

[31] Yu.M. Evdokimov, A. L. Platonov, A. S. Tikhonenko, and Ya.M. Varshavsky. A compact form of double-stranded dna in solution. *FEBS Letters*, 23(2):180–184, 1972. ISSN 00145793. doi: 10.1016/0014-5793(72)80335-1.

[32] G. Zanchetta, M. Nakata, M. Buscaglia, T. Bellini, and N. A. Clark. Phase separation and liquid crystallization of complementary sequences in mixtures of nanodna oligomers. *Proceedings of the National Academy of Sciences of the United States of America*, 105(4):1111–1117, 2008. ISSN 0027-8424. doi: 10.1073/pnas.0711319105.

[33] T. Bellini, G. Zanchetta, T. P. Fraccia, R. Cerbino, E. Tsai, G. P. Smith, M. J. Moran, D. M. Walba, and N. A. Clark. Liquid crystal self-assembly of random-sequence dna oligomers. *Proceedings of the National Academy of Sciences of the United States of America*, 109(4):1110–1115, 2012. ISSN 0027-8424. doi: 10.1073/pnas.1117463109.

[34] Tommaso P. Fraccia, Gregory P. Smith, Giuliano Zanchetta, Elvezia Paraboschi, Yougwooo Yi, David M. Walba, Giorgio Dieci, Noel A. Clark, and Tommaso Bellini. Abiotic ligation of dna oligomers templated by their liquid crystal ordering. *Nature Communications*, 6:6424, 2015. ISSN 2041-1723. doi: 10.1038/ncomms7424.

[35] Paul W. K. Rothemund. Folding dna to create nanoscale shapes and patterns. *Nature*, 440(7082):297–302, 2006. ISSN 0028-0836. doi: 10.1038/nature04586.

[36] Shawn M. Douglas, Hendrik Dietz, Tim Liedl, Björn Högberg, Franziska Graf, and William M. Shih. Self-assembly of dna into nanoscale three-dimensional shapes. *Nature*, 459(7245):414–418, 2009. ISSN 0028-0836. doi: 10.1038/nature08016.

[37] Sabine Sellner, Samet Kocabey, Katharina Nekolla, Fritz Krombach, Tim Liedl, and Markus Rehberg. Dna nanotubes as intracellular delivery vehicles in vivo. *Biomaterials*, 53:453–463, 2015. ISSN 1878-5905. doi: 10.1016/j.biomaterials.2015.02. 099.

[38] Anton Kuzyk, Robert Schreiber, Hui Zhang, Alexander O. Govorov, Tim Liedl, and Na Liu. Reconfigurable 3d plasmonic metamolecules. *Nature Materials*, 13(9): 862–866, 2014. ISSN 1476-1122. doi: 10.1038/nmat4031.

[39] Ralf Jungmann, Maier S. Avendaño, Johannes B. Woehrstein, Mingjie Dai, William M. Shih, and Peng Yin. Multiplexed 3d cellular super-resolution imaging with dna-paint and exchange-paint. *Nature Methods*, 11(3):313–318, 2014. ISSN 1548-7091. doi: 10.1038/nmeth.2835.

[40] Ingo H. Stein, Verena Schüller, Philip Böhm, Philip Tinnefeld, and Tim Liedl. Single-molecule fret ruler based on rigid dna origami blocks. *ChemPhysChem : A European Journal of Chemical Physics and Physical Chemistry*, 12(3):689–695, 2011. ISSN 1439-7641. doi: 10.1002/cphc.201000781.

[41] Dan T. Nguyen and Omar A. Saleh. Tuning phase and aging of dna hydrogels through molecular design. *Soft Matter*, 13(32):5421–5427, 2017. ISSN 1744-683X. doi: 10.1039/c7sm00557a.

[42] S. R. de Groot and P. Mazur. *Non-equilibrium Thermodynamics*. Dover Publications, New York, 1984. ISBN 0486647412.

[43] Stefan Duhr and Dieter Braun. Thermophoretic depletion follows boltzmann distribution. *Physical Review Letters*, 96(16), 2006. ISSN 0031-9007. doi: 10.1103/ PhysRevLett.96.168301.

[44] Stefan Duhr and Dieter Braun. Why molecules move along a temperature gradient. *Proceedings of the National Academy of Sciences of the United States of America*, 103 (52):19678–19682, 2006. ISSN 0027-8424. doi: 10.1073/pnas.0603873103.

[45] Dieter Braun and Albert Libchaber. Trapping of dna by thermophoretic depletion and convection. *Physical Review Letters*, 89(18), 2002. ISSN 0031-9007. doi: 10.1103/ PhysRevLett.89.188103.

[46] Franz M. Weinert and Dieter Braun. Optically driven fluid flow along arbitrary microscale patterns using thermoviscous expansion. *Journal of Applied Physics*, 104(10):104701, 2008. ISSN 00218979. doi: 10.1063/1.3026526.

[47] Franz Weinert, Jonas Kraus, Thomas Franosch, and Dieter Braun. Microscale fluid flow induced by thermoviscous expansion along a traveling wave. *Physical Review Letters*, 100(16), 2008. ISSN 0031-9007. doi: 10.1103/PhysRevLett.100.164501.

[48] Matthias Morasch, Dieter Braun, and Christof B. Mast. Heat-flow-driven oligonucleotide gelation separates single-base differences. *Angewandte Chemie (International ed. in English)*, 55(23):6676–6679, 2016. ISSN 1521-3773. doi: 10.1002/anie. 201601886.

[49] G. A. Soukup and R. R. Breaker. Relationship between internucleotide linkage geometry and the stability of rna. *RNA (New York, N.Y.)*, 5(10):1308–1325, 1999. ISSN 1355-8382.

[50] William B. Moore and A. Alexander G. Webb. Heat-pipe earth. *Nature*, 501(7468): 501–505, 2013. ISSN 0028-0836. doi: 10.1038/nature12473.

[51] M. C. Cross and P. C. Hohenberg. Pattern formation outside of equilibrium. *Reviews of Modern Physics*, 65(3):851, 1993. doi: 10.1103/RevModPhys.65.851.

[52] Eberhard Bodenschatz, Werner Pesch, and Guenter Ahlers. Recent developments in rayleigh-bénard convection. *Annual Review of Fluid Mechanics*, 32(1):709–778, 2000. ISSN 0066-4189. doi: 10.1146/annurev.fluid.32.1.709.

[53] David C. Fritts. Gravity wave dynamics and effects in the middle atmosphere. *Reviews of Geophysics*, 41(1):1, 2003. ISSN 8755-1209. doi: 10.1029/2001RG000106.

[54] J. K. Eaton and J. R. Fessler. Preferential concentration of particles by turbulence. *International Journal of Multiphase Flow*, 20:169–209, 1994. ISSN 03019322. doi: 10.1016/0301-9322(94)90072-8.

[55] Andreas Götzendorfer, Christof A. Kruelle, Ingo Rehberg, and Daniel Svensek. Localized subharmonic waves in a circularly vibrated granular bed. *Physical Review Letters*, 97(19):198001, 2006. ISSN 0031-9007. doi: 10.1103/PhysRevLett.97.198001.

[56] Junmei Chen and José A. López. Interactions of platelets with subendothelium and endothelium. *Microcirculation*, 12(3):235–246, 2005. ISSN 1073-9688. doi: 10.1080/10739680590925484.

[57] Thorne Lay, John Hernlund, and Bruce A. Buffett. Core–mantle boundary heat flow. *Nature Geoscience*, 1(1):25, 2008. ISSN 1752-0908. doi: 10.1038/ngeo.2007.44.

[58] Louis Lerman. Potential role of bubbles and droplets in primordial and planetary chemistry: Exploration of the liquid-gas interface as a reaction zone for condensation process. *Origins of Life and Evolution of the Biosphere : The Journal of the International Society for the Study of the Origin of Life*, 16(3-4):201–202, 1986. ISSN 0169-6149. doi: 10.1007/BF02421980.

[59] Katsuhiko Ariga and Jonathan P. Hill. Monolayers at air-water interfaces: from origins-of-life to nanotechnology. *Chemical Record*, 11(4):199–211, 2011. doi: 10.1002/tcr.201100004.

[60] Thomas H. Eickbush and Evangelos N. Moudrianakis. A mechanism for the entrapment of dna at an air-water interface. *Biophysical Journal*, 18(3):275–288, 1977. ISSN 00063495. doi: 10.1016/S0006-3495(77)85613-0.

[61] Elizabeth C. Griffith and Veronica Vaida. In situ observation of peptide bond formation at the water-air interface. *Proceedings of the National Academy of Sciences of the United States of America*, 109(39):15697–15701, 2012. ISSN 1091-6490. doi: 10.1073/pnas.1210029109.

[62] Robert D. Deegan, Olgica Bakajin, Todd F. Dupont, Greb Huber, Sidney R. Nagel, and Thomas A. Witten. Capillary flow as the cause of ring stains from dried liquid drops. *Nature*, 389(6653):827, 1997. ISSN 0028-0836. doi: 10.1038/39827.

[63] K. A. Smith. On convective instability induced by surface-tension gradients. *Journal of Fluid Mechanics*, 24(02):401, 1966. ISSN 0022-1120. doi: 10.1017/S0022112066000727.

[64] George Keith Batchelor. *An Introduction to Fluid Dynamics.* Cambridge Univ. Press, London, reprinted. edition, 1974. ISBN 0521098173.

[65] Deegan. Pattern formation in drying drops. *Physical Review. E, Statistical Physics, Plasmas, Fluids, and Related Interdisciplinary Topics*, 61(1):475–485, 2000. ISSN 1063-651X.

[66] Ronald G. Larson. Transport and deposition patterns in drying sessile droplets. *AIChE Journal*, 60(5):1538–1571, 2014. ISSN 0001-1541. doi: 10.1002/aic.14338.

[67] R. Savino, D. Paterna, and N. Favaloro. Buoyancy and marangoni effects in an evaporating drop. *Journal of Thermophysics and Heat Transfer*, 16(4):562–574, 2002. ISSN 0887-8722. doi: 10.2514/2.6716.

[68] Marc S. Weinberg and John J. Rossi. Comparative single-turnover kinetic analyses of trans-cleaving hammerhead ribozymes with naturally derived non-conserved sequence motifs. *FEBS letters*, 579(7):1619–1624, 2005. ISSN 0014-5793. doi: 10.1016/j.febslet.2005.02.016.

[69] SueAnn C. Dahm and Olke C. Uhlenbeck. Role of divalent metal ions in the hammerhead rna cleavage reaction. *Biochemistry*, 30(39):9464–9469, 1991. ISSN 0006-2960. doi: 10.1021/bi00103a011.

[70] Joseph N. Zadeh, Conrad D. Steenberg, Justin S. Bois, Brian R. Wolfe, Marshall B. Pierce, Asif R. Khan, Robert M. Dirks, and Niles A. Pierce. Nupack: Analysis and design of nucleic acid systems. *Journal of Computational Chemistry*, 32(1):170–173, 2011. ISSN 1096-987X. doi: 10.1002/jcc.21596.

[71] Ting F. Zhu and Jack W. Szostak. Coupled growth and division of model protocell membranes. *Journal of the American Chemical Society*, 131(15):5705–5713, 2009. ISSN 0002-7863. doi: 10.1021/ja900919c.

[72] I. Budin and J. W. Szostak. Physical effects underlying the transition from primitive to modern cell membranes. *Proceedings of the National Academy of Sciences of the United States of America*, 108(13):5249–5254, 2011. ISSN 0027-8424. doi: 10.1073/pnas.1100498108.

[73] Saidul Islam, Dejan-Krešimir Bučar, and Matthew W. Powner. Prebiotic selection and assembly of proteinogenic amino acids and natural nucleotides from complex mixtures. *Nature Chemistry*, 2017. ISSN 1755-4330. doi: 10.1038/nchem.2703.

[74] Carole Anastasi, Michael A. Crowe, Matthew W. Powner, and John D. Sutherland. Direct assembly of nucleoside precursors from two- and three-carbon units. *Angewandte Chemie (International ed. in English)*, 118(37):6322–6325, 2006. ISSN 0044-8249. doi: 10.1002/ange.200601267.

[75] S. F. Jones, G. M. Evans, and K. P. Galvin. Bubble nucleation from gas cavities — a review. *Advances in Colloid and Interface Science*, 80(1):27–50, 1999. ISSN 00018686. doi: 10.1016/S0001-8686(98)00074-8.

[76] Matthew W. Powner, Béatrice Gerland, and John D. Sutherland. Synthesis of activated pyrimidine ribonucleotides in prebiotically plausible conditions. *Nature*, 459(7244):239–242, 2009. ISSN 0028-0836. doi: 10.1038/nature08013.

[77] Jay G. Forsythe, Sheng-Sheng Yu, Irena Mamajanov, Martha A. Grover, Ramanarayanan Krishnamurthy, Facundo M. Fernández, and Nicholas V. Hud. Ester-mediated amide bond formation driven by wet-dry cycles: A possible path to polypeptides on the prebiotic earth. *Angewandte Chemie (International ed. in English)*, 54(34):9871–9875, 2015. ISSN 1521-3773. doi: 10.1002/anie.201503792.

[78] Nilesh Vaidya, Michael L. Manapat, Irene A. Chen, Ramon Xulvi-Brunet, Eric J. Hayden, and Niles Lehman. Spontaneous network formation among cooperative rna replicators. *Nature*, 491(7422):72–77, 2012. ISSN 0028-0836. doi: 10.1038/nature11549.

[79] Hannes Mutschler, Aniela Wochner, and Philipp Holliger. Freeze-thaw cycles as drivers of complex ribozyme assembly. *Nature Chemistry*, 7(6):502–508, 2015. ISSN 1755-4330. doi: 10.1038/nchem.2251.

[80] Laura Toppozini, Hannah Dies, David W. Deamer, Maikel C. Rheinstädter, and Heidar-Ali Tajmir-Riahi. Adenosine monophosphate forms ordered arrays in multilamellar lipid matrices: Insights into assembly of nucleic acid for primitive life. *PLOS One*, 8(5):e62810, 2013. doi: 10.1371/journal.pone.0062810.

[81] Sudha Rajamani, Alexander Vlassov, Seico Benner, Amy Coombs, Felix Olasagasti, and David Deamer. Lipid-assisted synthesis of rna-like polymers from mononucleotides. *Origins of Life and Evolution of the Biosphere : The Journal of the International Society for the Study of the Origin of Life*, 38(1):57–74, 2008. ISSN 0169-6149. doi: 10.1007/s11084-007-9113-2.

[82] Clémentine Gibard, Subhendu Bhowmik, Megha Karki, Eun-Kyong Kim, and Ramanarayanan Krishnamurthy. Phosphorylation, oligomerization and self-assembly in water under potential prebiotic conditions. *Nature Chemistry*, 10(2):212, 2018. ISSN 1755-4330. doi: 10.1038/nchem.2878.

[83] I. F. Sbalzarini and P. Koumoutsakos. Feature point tracking and trajectory analysis for video imaging in cell biology. *Journal of Structural Biology*, 151(2):182–195, 2005. ISSN 1047-8477. doi: 10.1016/j.jsb.2005.06.002.

[84] Philipp Reineck, Christoph J. Wienken, and Dieter Braun. Thermophoresis of single stranded dna. *Electrophoresis*, 31(2):279–286, 2010. ISSN 0173-0835. doi: 10.1002/elps.200900505.

[85] N. B. Vargaftik, B. N. Volkov, and L. D. Voljak. International tables of the surface tension of water. *Journal of Physical and Chemical Reference Data*, 12(3):817–820, 1983. ISSN 0047-2689. doi: 10.1063/1.555688.

[86] David R. Lide. *CRC Handbook of Chemistry and Physics*. CRC Press, Boca Raton, 82nd, ed., 2001-2001. edition, 2001. ISBN 9780849304828.

[87] Li Yuan-Hui and Sandra Gregory. Diffusion of ions in sea water and in deep-sea sediments. *Geochimica et Cosmochimica Acta*, 38(5):703–714, 1974. ISSN 00167037. doi: 10.1016/0016-7037(74)90145-8.

[88] Christopher J. D. Fell and H. Peter. Hutchison. Diffusion coefficients for sodium and potassium chlorides in water at elevated temperatures. *Journal of Chemical & Engineering Data*, 16(4):427–429, 1971. ISSN 0021-9568. doi: 10.1021/je60051a005.

[89] Agilent Technologies Ltd, Yarnton, Oxfordshire, England. Crysalispro, 2017.

[90] George M. Sheldrick. A short history of shelx. *Acta Crystallographica. Section A, Foundations of Crystallography*, 64(Pt 1):112–122, 2008. ISSN 0108-7673. doi: 10.1107/S0108767307043930.

[91] George M. Sheldrick. Crystal structure refinement with shelxl. *Acta Crystallographica. Section C, Structural Chemistry*, 71(Pt 1):3–8, 2015. doi: 10.1107/S2053229614024218.

[92] George A. Khoury, Richard C. Baliban, and Christodoulos A. Floudas. Proteome-wide post-translational modification statistics: frequency analysis and curation of the swiss-prot database. *Scientific Reports*, 1, 2011. ISSN 2045-2322. doi: 10.1038/srep00090.

[93] Joseph Gal. Pasteur and the art of chirality. *Nature Chemistry*, 9(7):604–605, 2017. ISSN 1755-4330. doi: 10.1038/nchem.2790.

[94] T. Eriksson, S. Bjorkman, B. Roth, and P. Hoglund. Intravenous formulations of the enantiomers of thalidomide: pharmacokinetic and initial pharmacodynamic characterization in man. *The Journal of Pharmacy and Pharmacology*, 52(7):807–817, 2000. ISSN 0022-3573.

[95] Donna G. Blackmond. The origin of biological homochirality. *Cold Spring Harbor Perspectives in Biology*, 2(5):a002147, 2010. ISSN 1943-0264. doi: 10.1101/cshperspect. a002147.

[96] Sandra Pizzarello. The chemistry of life's origin: a carbonaceous meteorite perspective. *Accounts of Chemical Research*, 39(4):231–237, 2006. ISSN 0001-4842. doi: 10.1021/ar050049f.

[97] Jason E. Hein, Eric Tse, and Donna G. Blackmond. A route to enantiopure rna precursors from nearly racemic starting materials. *Nature Chemistry*, 3(9):704–706, 2011. ISSN 1755-4330. doi: 10.1038/nchem.1108.

[98] Cornelia Meinert, Patrick Cassam-Chenaï, Nykola C. Jones, Laurent Nahon, Søren V. Hoffmann, and Uwe J. Meierhenrich. Anisotropy-guided enantiomeric enhancement in alanineusing far-uv circularly polarized light. *Origins of Life and Evolution of Biospheres*, 45(1):149–161, 2015. ISSN 1573-0875. doi: 10.1007/s11084-015-9413-x.

[99] G. Holzwarth and P. Doty. The ultraviolet circular dichroism of polypeptides 1. *Journal of the American Chemical Society*, 87(2):218–228, 1965. ISSN 0002-7863. doi: 10.1021/ja01080a015.

[100] John A. Schellman. Circular dichroism and optical rotation. *Chemical reviews*, 75 (3):323–331, 1975. ISSN 0009-2665. doi: 10.1021/cr60295a004.

[101] S. Beychok. Circular dichroism of biological macromolecules. *Science (New York, N.Y.)*, 154(3754):1288–1299, 1966. ISSN 0036-8075.

[102] Lee Whitmore and B. A. Wallace. Protein secondary structure analyses from circular dichroism spectroscopy: methods and reference databases. *Biopolymers*, 89(5):392–400, 2008. ISSN 0006-3525. doi: 10.1002/bip.20853.

[103] Kacey Claborn, Eileen Puklin-Faucher, Miki Kurimoto, Werner Kaminsky, and Bart Kahr. Circular dichroism imaging microscopy: application to enantiomorphous twinning in biaxial crystals of 1,8-dihydroxyanthraquinone. *Journal of the American Chemical Society*, 125(48):14825–14831, 2003. ISSN 0002-7863. doi: 10.1021/ja035644w.

[104] Richard G. Nelson and W. Curtis Johnson. Optical properties of sugars. i. circular dichroism of monomers at equilibrium. *Journal of the American Chemical Society*, 94(10):3343–3345, 1972. ISSN 0002-7863. doi: 10.1021/ja00765a013.

[105] Theodore C. Oakberg, John G. Trunk, and John C. Sutherland. Calibration of photoelastic modulators in the vacuum uv. In David B. Chenault, Michael J. Duggin, Walter G. Egan, and Dennis H. Goldstein, editors, *Polarization Analysis, Measurement, and Remote Sensing III*, SPIE Proceedings, pages 101–111. SPIE, 2000. doi: 10.1117/12.406617.

[106] J. C. Sutherland. Calibration of photoelastic modulator based dichrometers: maintaining constant phase across the spectrum. *Journal of Instrumentation*, 11(07): P07016–P07016, 2016. doi: 10.1088/1748-0221/11/07/P07016.

[107] Jan Hendrik Bredehöft, Nykola C. Jones, Cornelia Meinert, Amanda C. Evans, Søren V. Hoffmann, and Uwe J. Meierhenrich. Understanding photochirogenesis: solvent effects on circular dichroism and anisotropy spectroscopy. *Chirality*, 26(8): 373–378, 2014. doi: 10.1002/chir.22329.

[108] Donald A. Burns and Emil W. Ciurczak. *Handbook of Near-Infrared Analysis*, volume 35 of *Practical Spectroscopy*. CRC Press, Boca Raton, FL, 3rd ed. edition, 2008. ISBN 084937393X.

[109] Dr. Geoff Adams. Winlens 3d basic v1.2.8, 2018.

List of Figures

List of Tables

Appendix A: Associated First Author Publication

Matthias Morasch, Dieter Braun, and Christof B. Mast. **Heat-Flow-Driven Oligonucleotide Gelation Separates Single-Base Differences.** Angew. Chem. In. Ed. 2016, 55, 6676-6679.

DNA Hydrogels | Hot Paper |

Heat-Flow-Driven Oligonucleotide Gelation Separates Single-Base Differences

Matthias Morasch, Dieter Braun, and Christof B. Mast*

Abstract: DNA phase transitions are often induced by the addition of condensation agents or by dry concentration. Herein, we show that the non-equilibrium setting of a moderate heat flow across a water-filled chamber separates and gelates DNA strands with single-base resolution. A dilute mix of DNA with two slightly different gel-forming sequences separates into sequence-pure hydrogels under constant physiological solvent conditions. A single base change in a 36 mer DNA inhibits gelation. Only sequences with the ability to form longer strands are concentrated, further elongated, and finally gelated by length-dependent thermal trapping. No condensation agents, such as multivalent ions, were added. Equilibrium aggregates from dry concentration did not show any sequence separation. RNA is expected to behave identically owing to its equal thermophoretic properties. The highly sequence-specific phase transition points towards new possibilities for non-equilibrium origins of life.

Nucleic acids are one of the most abundant molecules in biology. They are able to store large amounts of information in a condensed state at an unprecedented density.[1] At the same time, they provide access for readout at any time by local unwinding and re-packing. Their ability to efficiently condense or self-organize while still being accessible for sequence-selective processes, such as replication or transcription, is an essential aspect for the development of life and has been intensively researched.[2,3]

Experimentally, such condensation processes are described as phase transitions between the dilute (sol) phase and a dense phase. The dense phase is usually induced by concentrating nucleic acids or adding multivalent ions or proteins. One example is the condensation of long DNA (> 1 kbp), assisted by spermidine^{3+} or $Co(NH_3)_6^{3+}$ ions that bind to the negatively charged phosphate groups, allowing for DNA–DNA attraction.[2,4] Further condensation agents include cationic lipids, polymers, and metal complexes.[3] Monovalent ions, on the other hand, only partially shield the repulsive force between the DNA strands. This hinders strand condensation without the help of neutral polymers or the use of modified DNA hybrids.[5] In pure water, complementary DNA strands can self-organize into liquid crystals at

very high concentrations (300–1000 mg mL^{-1}) achieved by drying.[6] Interestingly, this process was found to generate complementarity from a pool of random and short (< 16 nts) sequences during their concentration,[7] forming initial conditions for abiotic ligation.[8] Longer random strands, however, formed liquid crystals without any sequence selective behavior.

The experiments discussed above illustrate the diversity of DNA self-assembly and aggregation. They focus only on the final equilibrium result of the ordering process, which is frozen and locked in a minimal state of the free-energy landscape. Herein, we demonstrate that a dynamic, non-equilibrium approach to a DNA phase transition allows for a highly sequence-selective accumulation and separation of initially dilute oligomers. Compared to the discussed methods, heat-flow-driven gelation of DNA occurs without the addition of condensation agents, such as multivalent ions, and under physiological buffer conditions (Supporting Information Movie M1).

The non-equilibrium condition is solely implemented by a heat flux across the probe vessel and causes simultaneous solvent convection and thermophoresis of biomolecules (Supporting Information Figure S1–S3).[9] Both effects superimpose and implement a length-dependent thermal trap for biomolecules. Thermal traps have been shown to push the concentration of fatty-acids above their critical micelle concentration,[10] they can also arrange micrometer-sized beads to 2D-crystals via slip-flow,[11] and drive the replication and selection of DNA in an open flow chamber.[12]

Herein, we use thermal traps to concentrate short DNA strands that can hybridize to their own kind at several binding sites. At higher concentrations, these building blocks assemble into larger DNA polymers that are subsequently accumulated more efficiently by thermal trapping (Figure 1).[13] We show that this escalated elongation of DNA by a thermal trap acts as a dynamic non-linear switch that amplifies even the smallest sequence differences: though initially mixed, different gel-forming sequences are separated into distinct, sequence-pure gels. In contrast to non-equilibrium thermal trapping, the equilibrated DNA assemblies obtained by dry-condensation did not show any sequence dependent separation.

To quantify the sequence selectivity of heat-flow-driven gelation of oligonucleotides, we designed five slightly different 36 mer DNA strands. Strand **A** is a reference strand with three self-complementary binding sites (Table 1). Strands **B**–**E** have one, three, four, and six single nucleotide changes compared to **A**. The three hybridization sites of each strand can either form hairpins (Figure 1b, Box 1) or bind to corresponding sequences on other strands (Figure 1b, Box 3).

[*] M. Morasch, Prof. D. Braun, Dr. C. B. Mast
    Systems Biophysics, Physics Department, NanoSystems Initiative
    Munich and Center for Nanoscience
    Ludwig Maximilians Universität München
    Amalienstrasse 54, 80799 Munich (Germany)
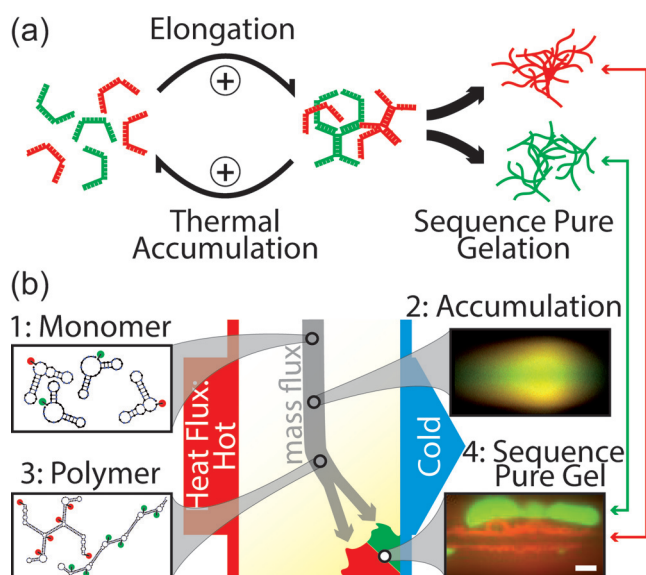   E-mail: christof.mast@physik.uni-muenchen.de

Figure 1. DNA gelation by thermal accumulation. a) DNA that contains self-complementary sequences can bind to its own kind (same color in scheme) after heat-flux-driven concentration. The longer complexes are more efficiently concentrated by length-dependent thermal trapping, leading to the formation of a DNA hydrogel. b) Even small differences in the sequence lead to a demixing or inhibition of DNA gelation. Sequences are distinguished using different fluorescent labels (FAM: green, Cy5: red). Scale bar: 20 μm.

Table 1: Properties of strands **A**–**E**.[a]

Strand	**A**	**B**	**C**	**D**	**E**
Dye	Cy5		——— FAM ———		
# Mutated Bases vs. A	0	1	3	4	6
Structure					
Builds Gel: (Fig. 2)	Yes	No	No	Yes	Yes
Separates From A (Fig. 3):					
Thermal Trap:	-	Yes	Yes	No	Yes
Drying (50°C):	-	No	No	No	No

[a] To show the sequence selectivity of the heat flow driven gelation of DNA, five different sequences were analyzed. Strand **A** is the reference strand with three self-complementary binding regions for hybridization, each made out of 12 nts and stained with Cy5. Strands **B** and **C** comprise one or three single base changes, respectively, which already inhibits their gelation (Figure 2). Both strands also separate well from the reference strand **A** in a competitive gelation (Figure 3). Strands **D** and **E** contain 4 or 6 single base changes, respectively, while retaining the full self-complementarity of the binding regions. In contrast to strand **E**, strand **D** is not separated from **A** during competitive gelation, probably due to its common center binding region (Figure 3)

All five sequences consist exclusively of G and C bases, which represents a worst-case scenario: The reduced alphabet size decreases sequence specificity while the high G-content

facilitates G-quadruplex formation.[14, 15] Our results therefore also apply to more moderate designs using four base letters. To show this, we additionally demonstrate the gelation of AT-only sequences or sequences that contain all canonical bases (Figure S4,S5).

We experimentally implemented a thermal trap by focusing an infrared laser inside the center of a water-filled, horizontally aligned borosilicate capillary (Figure S1).[13, 16] The implementation with a laser allows for full optical inspection and ensures faster relaxation times of the system as compared to a purely gravitationally driven trap (Figure S6). The absorption of the moving IR laser simultaneously creates a thermal gradient as well as circular fluid convection via thermoviscous pumping (Figure S1–S3, Movie M3).[17] The peak and center temperature is 65°C, while the bottom surface is actively cooled by a thermoelectric element to 49°C.

While the setup is almost identical to the one shown in previous work, we are now extending the principle of length-dependent thermal trapping:[13] By including multiple DNA strands that cover a wide range of the smallest possible sequence differences, we demonstrate that thermal traps allow for a sequence selectivity on a single-base level by utilizing the non-equilibrium formation of hydrogels (Sequences: Table ST1).

We first checked strands **A**–**E** individually for their ability to form a hydrogel in physiological buffer at $c_0 = 10$ μM initial concentration (Figure 2a). As expected, the thermal trap gelated the strands **A**, **D**, and **E** after around 40 min because of their three full self-complementary hybridization sites. Strands **B** and **C**, however, did not form a gel. This shows that even a single base difference compared to **A** is enough to inhibit gelation.

This result can be explained by the calculated length distribution of the DNA assemblies at 55°C shortly before gelation, at which strands were concentrated to 100 μM (Figure S7). Only solutions containing strands **A**, **D**, and **E** allow for larger DNA assemblies. The assemblies are then favorably accumulated by thermal trapping, while strands with sequence mismatches (**B**, **C**) stay unbound and cannot be further concentrated.

The ability to form branched assemblies is not a necessary requirement for heat-driven gelation of DNA: Strands with only two hybridization sites made out of 25 canonical bases each also form hydrogels, which we used to compare it to UV and calculated melting curves (Figures S5,S8).[13] We also excluded the possibility that the DNA could have formed highly ordered structures, such as crystals, using polarization microscopy (Figure S9). The DNA hydrogel showed a remarkable stability even outside the trap, where it remained stable for days under physiological conditions (see Movie M2).

We were also interested to see how two gel-forming strands compete against each other in the race for the limited space in the same solution. Thermal trapping of an initially mixed solution with strands **A** and **E** resulted in separated, sequence-pure hydrogels with a time difference of 15 min (Figure 3a, Movie M4). Both strands only differ by a change of one base pair per binding site, showing the strong sequence selecting abilities of the process.
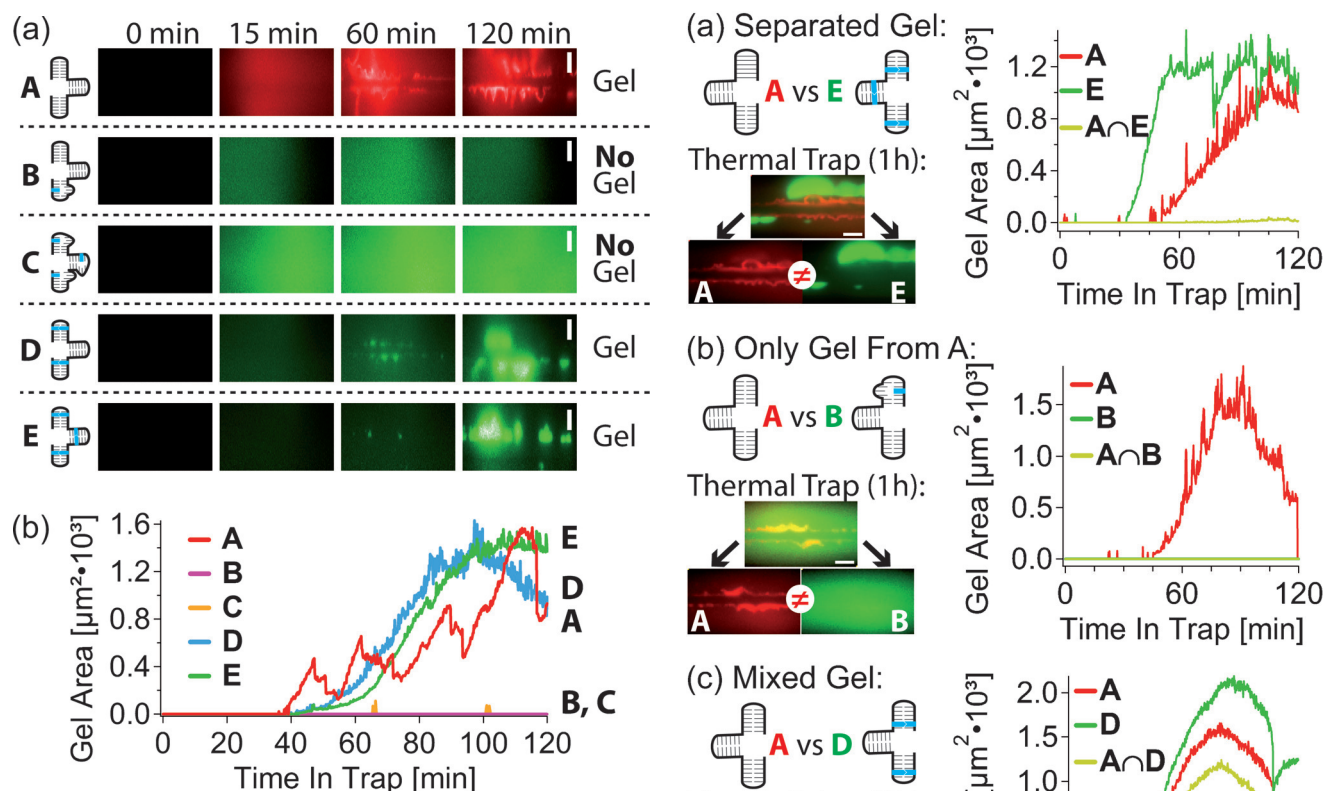
Figure 2. Sequence-selective gelation of DNA oligomers in a thermal trap. a) Strands **A**, **D**, and **E** are made of three fully self-complementary hybridization sections, and thus are elongated and further concentrated by length-selective thermal trapping. Strands **B** and **C** contain one or three changes in their sequence, respectively. This alone suffices to hinder heat-flow-driven gelation owing to their reduced ability to form longer strands that are favored by thermal trapping. The color of the pictures indicates the attached dye (red: Cy5, green: FAM). b) The measured hydrogel area reflects the snapshots shown in (a). The gelation dynamics and its fluctuating release from the glass surface lead to a damped oscillatory dynamics (e.g. strand **A**). Scale bars: 20 μm.

Trapping of a solution that contained both sequences **A** and **B** resulted in a sequence pure hydrogel from **A**, while strands **B** could not gelate, as expected (Figure 3b). This also corresponds to a separation of both strands, for example after flushing the capillary with buffer solution, and shows that sequence selection is possible with only a single base difference in the full 36 mer strand. No separation is achieved by thermally trapping and strands **A** and **D** gelate together. They differ only in one base pair in two full self-complementary hybridization sites, while the central binding site is unchanged. This allows for both strands to form large, mixed networks (Figure 3c). We compared the non-equilibrium gelation by a temperature gradient to the equilibrated DNA assemblies obtained by dry concentration and re-suspension to the initial volume of 10 μl at 55 °C. The formed aggregates did not show any signs of sequence separation (Figure 3d).

We showed experimentally that the heat-flux driven sol–gel phase transition of oligonucleotides is a highly sequence selective process. Already a single base difference between two DNA sequences was enough to separate both strands by gelation. One base pair per self-complementary binding site
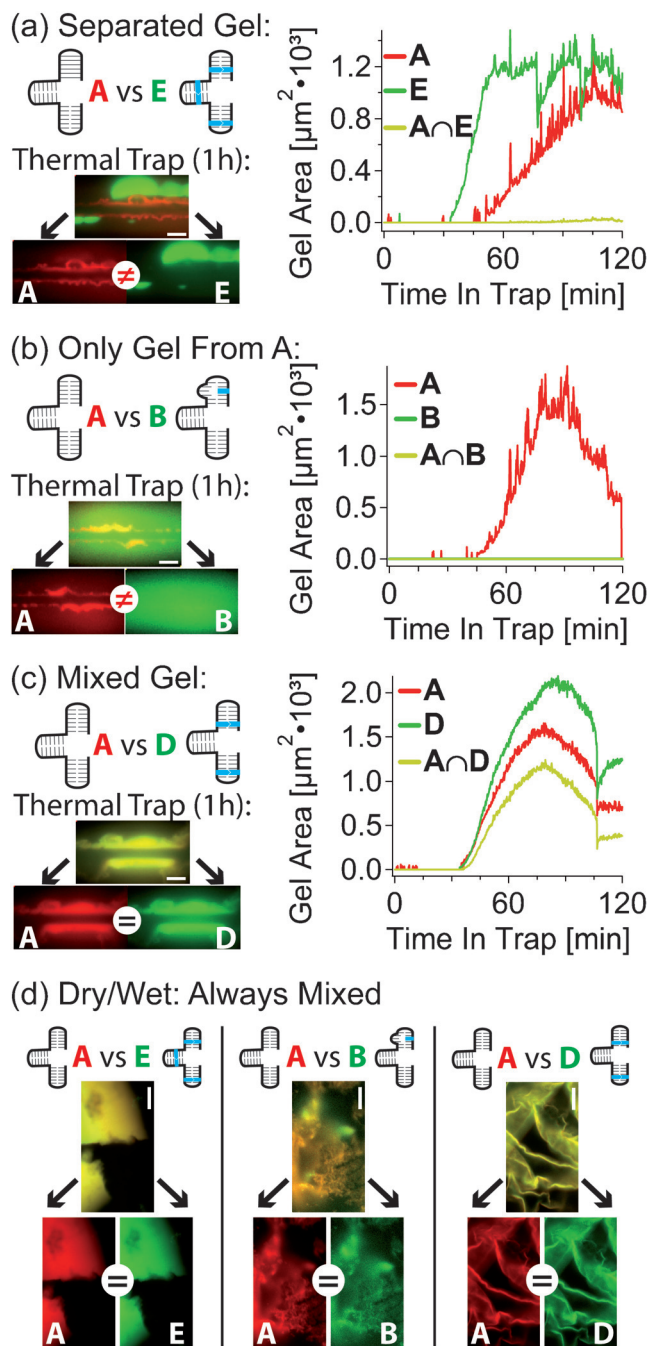

Figure 3. Competitive hydrogel formation: Strands **B**–**E** were each mixed with **A** in 1xPBS and concentrated by thermal trapping as well as in a dry-wet cycle. a) One base pair was modified in each of the three hybridization sites of strand **E**, which preserved self-complementarity. The sequence change alone sufficed to allow for the formation of spatially distinct and sequence pure hydrogels (no common gel area **A∩E**, plotted in yellow). b) Even a single base change in sequence suffices to inhibit the gelation of strand **B**. This allows for a sequence separation of strands **B** and **A** from a mixed solution. c) One base pair was modified in each of the two framing hybridization sites of strand **D**, preserving the self-complementarity of each 12 nts sequence block. The central sequence block is unchanged and therefore compatible to strand **A**, yielding a mixed gel made out of **D** and **A**. d) Dry-concentration and subsequent resuspension with MilliQ water of the same solutions used in (a–c) always produced mixed aggregates without strand separation or other indication of sequence selectivity. Scale bars: 20 μm.

sufficed to create two sequence-pure, distinct hydrogels. The gelation of sticky-ended DNA confirms the predicted hyper-exponential escalation in a thermal gradient.

The process could also be a promising mechanism to approach several questions concerning the origins of life. While recent advances demonstrate the prebiotically plausible synthesis of RNA oligonucleotides and their replication by RNA enzymes, it remains unclear how functional ribozymes came into existence in the first place.[18] If placed in porous rock and filled with a dilute mix of random oligonucleotides, thermal traps could have accumulated and selected for the most interacting RNA strands. Only those would be concentrated that were able to stick to each other and form hairpins, the most prevalent secondary structures in ribozymes. At the same time, the separation of these strands into sequence-pure gels could allow for high local ribozyme concentrations and therefore fast catalytic reaction times.

In contrast to crystalline phases, oligonucleotide hydrogels mostly consist of water and should still be accessible to small RNA substrates via diffusion. These could interact within the whole hydrogel volume and not only on its surface. Moreover, sequence-pure hydrogels act as sequence filters. From a mixed solution, they only incorporate sequences of their own kind. In the presence of a random oligomer pool, for example, built by dry polymerization, this corresponds to a replication reaction that enriches one family of sequences from a random input.[19] Even within the relatively unknown conditions during the origins of life, thermal traps should have been highly abundant. A heat flow is generated by almost all hydrothermal, chemical, and geological systems, making heat fluxes through porous systems a common scenario.

Experimental Section

The chamber geometry and laser heating are similar to the conditions in the previously described polymerization trap.[13] A borosilicate capillary with a rectangular cross section of $100\ \mu m \times 50\ \mu m$ contains the analyte solution and is thermally coupled to a Peltier element with sapphire and silicon (see Figure S1 for experiments). The absorption of a moving 1940 nm infrared (IR) laser (20W, IPG Photonics) implements the thermal gradient and the thermoviscous convection flow. The thermal gradient of 7 K over 50 μm is measured using the temperature dependent fluorescence of the BCECF (2′,7′-bis-(2-carboxyethyl)-5-(and-6)-carboxyfluorescein) signal in 10 mM TRIS buffer. Flow speeds are measured using position tracking of silica beads (Figure S2). For DNA trapping, we use physiological salt concentrations (1xPBS) without any multivalent ions or proteins as standard buffer. All sequences were fluorescently labeled to measure gelation and subsequent sequence separation (Sequences: Table ST1). By gelating unstained DNA we excluded artifacts from a false-positive gelation mediated by interacting fluorophores (Figure S5). Multiple images at various LED currents are used to increase the dynamic range of the 12-bit CCD camera (PCO imaging). Determination of gel area from experimental data is done as described in the supplementary information.

Acknowledgements

[1] G. M. Church, Y. Gao, S. Kosuri, *Science* **2012**, *337*, 1628.
[2] V. A. Bloomfield, *Biopolymers* **1997**, *44*, 269–282.
[3] G.-Y. Li, R.-L. Guan, L.-N. Ji, H. Chao, *Coord. Chem. Rev.* **2014**, *281*, 100–113.
[4] C. C. Conwell, I. D. Vilfan, N. V. Hud, *Proc. Natl. Acad. Sci. USA* **2003**, *100*, 9296–9301.
[5] a) L. S. Lerman, *Proc. Natl. Acad. Sci. USA* **1971**, *68*, 1886–1890; b) Y. Evdokimov, A. L. Platonov, A. S. Tikhonenko, Y. Varshavsky, *FEBS Lett.* **1972**, *23*, 180–184; c) A. Singh, M. Tolev, M. Meng, K. Klenin, O. Plietzsch, C. I. Schilling, T. Muller, M. Nieger, S. Bräse, W. Wenzel et al., *Angew. Chem. Int. Ed.* **2011**, *50*, 3227–3231; *Angew. Chem.* **2011**, *123*, 3285–3289.
[6] G. Zanchetta, M. Nakata, M. Buscaglia, T. Bellini, N. A. Clark, *Proc. Natl. Acad. Sci. USA* **2008**, *105*, 1111–1117.
[7] T. Bellini, G. Zanchetta, T. P. Fraccia, R. Cerbino, E. Tsai, G. P. Smith, M. J. Moran, D. M. Walba, N. A. Clark, *Proc. Natl. Acad. Sci. USA* **2012**, *109*, 1110–1115.
[8] T. P. Fraccia, G. P. Smith, G. Zanchetta, E. Paraboschi, Y. Yi, D. M. Walba, G. Dieci, N. A. Clark, T. Bellini, *Nat. Commun.* **2015**, *6*, 6424.
[9] a) S. Duhr, D. Braun, *Proc. Natl. Acad. Sci. USA* **2006**, *103*, 19678–19682; b) M. Reichl, M. Herzog, A. Götz, D. Braun, *Phys. Rev. Lett.* **2014**, *112*, 198101; c) J. K. G. Dhont, S. Wiegand, S. Duhr, D. Braun, *Langmuir* **2007**, *23*, 1674–1683; d) J. K. G. Dhont, W. J. Briels, *Eur. Phys. J. E* **2008**, *25*, 61–76; e) P. Baaske, F. M. Weinert, S. Duhr, K. H. Lemke, M. J. Russell, D. Braun, *Proc. Natl. Acad. Sci. USA* **2007**, *104*, 9346–9351; f) K. Clusius, G. Dickel, *Naturwissenschaften* **1938**, *26*, 546.
[10] I. Budin, R. J. Bruckner, J. W. Szostak, *J. Am. Chem. Soc.* **2009**, *131*, 9628–9629.
[11] F. M. Weinert, D. Braun, *Phys. Rev. Lett.* **2008**, *101*, 168301.
[12] M. Kreysing, L. Keil, S. Lanzmich, D. Braun, *Nat. Chem.* **2015**, *7*, 203–208.
[13] C. B. Mast, S. Schink, U. Gerland, D. Braun, *Proc. Natl. Acad. Sci. USA* **2013**, *110*, 8030–8035.
[14] M. H. Huntley, A. Murugan, M. P. Brenner, *arXiv* **2016**, 1602.05649v1.
[15] T. Simonsson, *Biol. Chem.* **2005**, *382*, 1431–6730.
[16] C. B. Mast, D. Braun, *Phys. Rev. Lett.* **2010**, *104*, 188102.
[17] a) F. M. Weinert, D. Braun, *J. Appl. Phys.* **2008**, *104*, 104701; b) F. M. Weinert, J. A. Kraus, T. Franosch, D. Braun, *Phys. Rev. Lett.* **2008**, *100*, 164501.
[18] a) M. Powner, J. Sutherland, J. Szostak, *Synlett* **2011**, 1956–1964; b) A. Wochner, J. Attwater, A. Coulson, P. Holliger, *Science* **2011**, *332*, 209–212.
[19] a) J. M. A. Carnall, C. A. Waudby, A. M. Belenguer, M. C. A. Stuart, J. J.-P. Peyralans, S. Otto, *Science* **2010**, *327*, 1502–1506; b) M. S. Verlander, R. Lohrmann, L. E. Orgel, *J. Mol. Evol.* **1973**, *2*, 303–316; c) M. Morasch, C. B. Mast, J. K. Langer, P. Schilcher, D. Braun, *ChemBioChem* **2014**, *15*, 879–883.

Angewandte Chemie

Eine Zeitschrift der Gesellschaft Deutscher Chemiker

Supporting Information

Heat-Flow-Driven Oligonucleotide Gelation Separates Single-Base Differences

Matthias Morasch, Dieter Braun, and Christof B. Mast*

ange_201601886_sm_miscellaneous_information.pdf
ange_201601886_sm_Movie_1.m4v
ange_201601886_sm_Movie_2.m4v
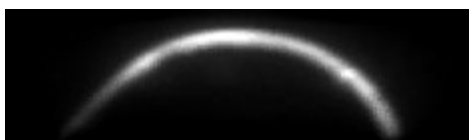ange_201601886_sm_Movie_3a.m4v
ange_201601886_sm_Movie_3b.m4v
ange_201601886_sm_Movie_4.mp4

Supplementary Movie M1

The thermal trap drives the gelation of 10 µM concentrated DNA **A** in 1x PBS buffer (see above). One second in the movie corresponds to 250 seconds in real time. Measurement time was 2 h.
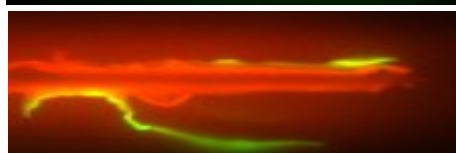
Supplementary Movie M2

The loosening of the DNA gel (DNA **X/Y**) from the capillary and its behavior is shown here. The gel was therefore first exposed to a high flow of water and then tracked.
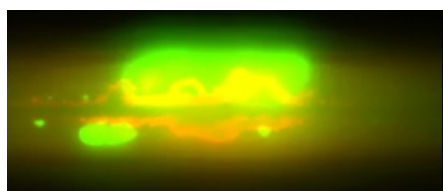
Supplementary Movie M3
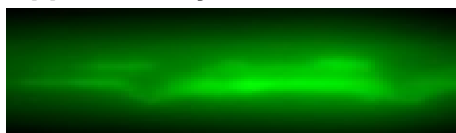
a) Formation of a hydrogel by thermal trapping with FAM labeled DNA **A**.

b) After flushing in Cy5 labeled DNA **A** of the same sequence, thermal trapping leads to the replacement of previously formed gel from the center.

Supplementary Movie M4

Gelation of DNA **A** (red) and **E** (green) at the same time (see Fig. 3a).

DNA Sequences

The sequences of the used DNA strands are given below. Differences in sequence to DNA **A** are marked blue. DNA **X** and **Y** together form a linear, double-stranded segment with self-complementary sticky ends that also forms a gel inside the trap (see movie M2, Fig. S5) and was used for some of the analysis. Due to its size it requires less DNA (1 µM starting concentration) to form the gel in the same buffer (1 x PBS withouth multivalent ions).

Name	5'-3'-sequence
A	GCGGGC-GCCCGC-*CGCGGC-GCCGCG*-GGCCGC-GCGGCC-(Cy5)
B	GCGGGC-GCCCGC- *CGCGGC-GCCGCG*-GGCCGC-GC**C**GCC-(FAM)
C	GCGG**C**C-GCCCGC-*CGCG**C**C-GCCGCG*-GGCCGC-GCGG**G**C-(FAM)
D	GCGG**C**C-G**G**CCGC- *CGCGGC-GCCGCG*- G**C**CCGC-GCGG**G**C-(FAM)
E	GCGG**C**C-G**G**CCGC- *CG**G**GGC-GCCC**C**G*- GG**G**CGC-GCGC**C**C-(FAM)
X	GTTATTGCAC(FAM)TGCATGTAGCCCTGAACACTCTGGGGGCCCAGTGACTACTCCTCCTCGACGCCTGAGGGCACTT GGTCTTGAGAGCCCCTTAGGTAGTTGAACCGGCCATTCCCCAGGGC
Y	TCAGGGCTACATGCA(ROX)GTGCAATAACGCCCTGGGGAATGGCCGGTTCAACTACCTAAGGGGCTCTCAAGACCAA GTGCCCTCAGGCGTCGAGGAGGAGTAGTCACTGGGCCCCCAGAGTGT
AT	TTTAATATAATTATATTAAATTAATATTAATTAATATTAAATATATATTTAAATATATAT -(FAM)

Table ST1. Sequences of the branching DNA strands from the main text and the linear DNA strands used for additional analysis of the gel. DNA **A**-**E**: 36 mer branching DNA strands with 1, 3, 4, and 6 bases difference with respect to **A**, shown in blue. DNA **X**/**Y**: In combination, they form a dsDNA strand with two sticky ends, which was used for some of the analysis due to its simpler structure. **AT** DNA: DNA made of A and T bases only, showing that not only short G/C-pure strands form a gel.

Finite element simulations.

We used Comsol as framework for the 3D finite-element simulations and incorporated a 2-D temperature map from the experiment using the convection speeds of both orthogonal fluid flows as well as the temperature dependent fluorescence of (2',7'-Bis-(2-Carboxyethyl)-5-(and-6)-Carboxyfluorescein) (BCECF).[1] We measured the convection speeds of both orthogonal fluid flows using fluorescent beads. The three-dimensional temperature and velocity fields are therefore extrapolated from the two dimensional, z-averaged measurements. The second, gravitationally driven flow speed was determined when symmetrically moving the laser spot. This stopped thermoviscous pumping but still allowed for gravitationally driven convection. While available methods are unable to cover combined calculations of polymerization, phase transition and three-dimensional thermal trapping, it is possible to calculate the exclusive cases with separate fluid flows in the x-y (thermoviscous) or the y-z plane (gravitation), respectively. We find that the gravitationally driven thermal trap predominantly accumulates long nucleic acids >1e^4 nts on the bottom surface, centered along the y-axis. The thermoviscous driven thermal trap however favors DNA strands with a length of 37 nts that are accumulated in the center of the capillary (see Fig. S2, S3). Accordingly, the short DNA strands are first accumulated in the capillary center by the thermoviscous driven trap, while the longer, hybridized polymers and the hydrogel are concentrated at the capillary bottom by the gravitationally driven thermal trap.
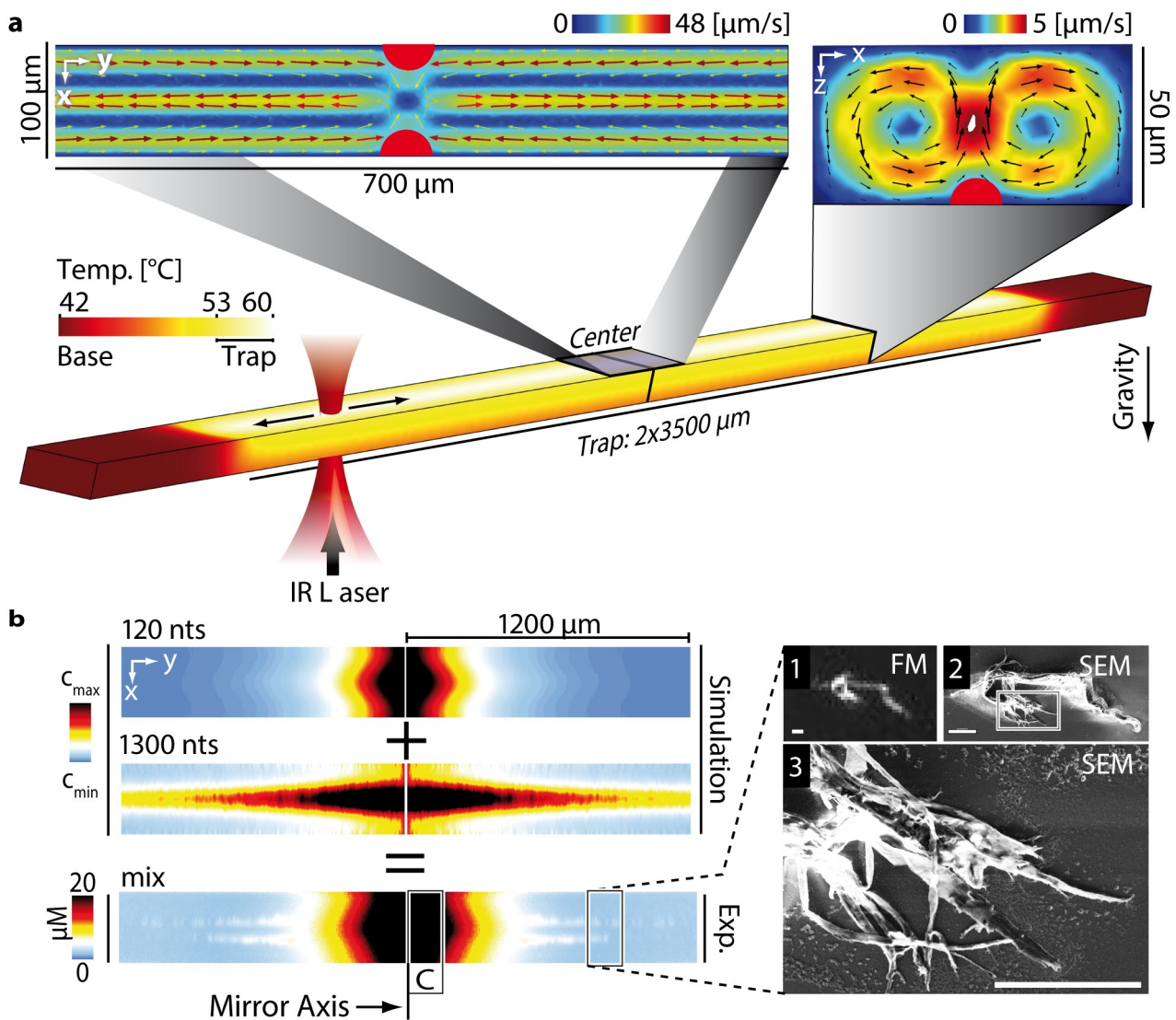
Figure S1. Finite element simulation of the experiment. (a) Convection flow speeds. The experimental value for the maximal thermoviscous flow speed is 46 µm/s, while the maximal gravitationally driven convection flow speed is 4 µm/s. Both values were measured using fluorescent beads (1 µm) and used in the finite element simulation. Temperature field: We measured the 2-D temperature distribution using temperature dependent fluorescent dyes in order to estimate the 3-D temperature field which is created by the IR beam absorption inside the capillary. The width of the IR laser spot (10µm), the absorption characteristics of the focused, 1940 nm beam, and the thermal boundary conditions (Peltier-elements: 10 °C) were then used to infer the corresponding, three-dimensional temperature distribution. (b) Simulation and experiment. Finite element simulations of the experiment illustrate that the thermoviscous driven trap (flow in x-y plane) accumulates the short DNA monomers predominantly at the capillary center. In contrast, the gravitationally driven thermal trap (flow in x-z plane) concentrates preferentially long polymers at the capillary bottom, which allows for the formation of the DNA hydrogel. The measurement starts with 1 µM sticky ended DNA **X/Y** and shows the qualitative agreement with the superimposed simulations for various

oligomer lengths after ~40 minutes. The DNA **X/Y** gel is stable enough to be extracted in one piece (see supplementary movie M2) and visualized with fluorescence microscopy and scanning electron microscopy. The scale bars correspond to 50 μm.
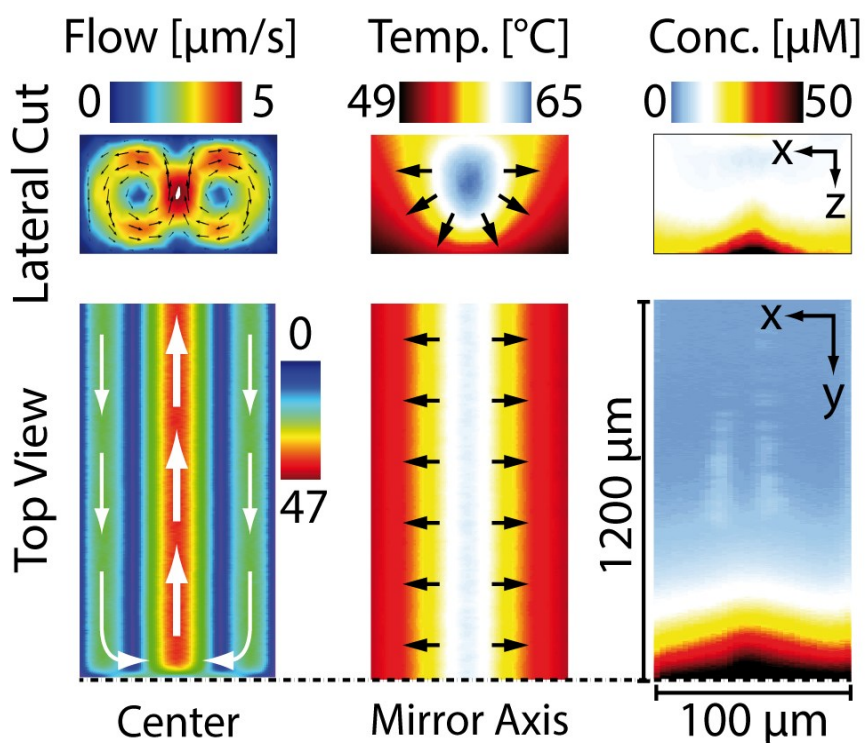

Figure S2. Left: Velocities of both orthogonal convection flows, measured along the x-y plane using fluorescent bead tracking and calculated along the x-z plane using finite element methods (FEM). Center: Measured (x-y plane) and calculated (x-z plane) temperature profiles using BCECF fluorescence and FEM, respectively. Direction of thermophoresis is indicated with black arrows. Right: Measured (x-y plane) and calculated (x-z plane) concentration profiles using the fluorescence of FAM and Cy5 labeled DNA **X/Y** and FEM, respectively.
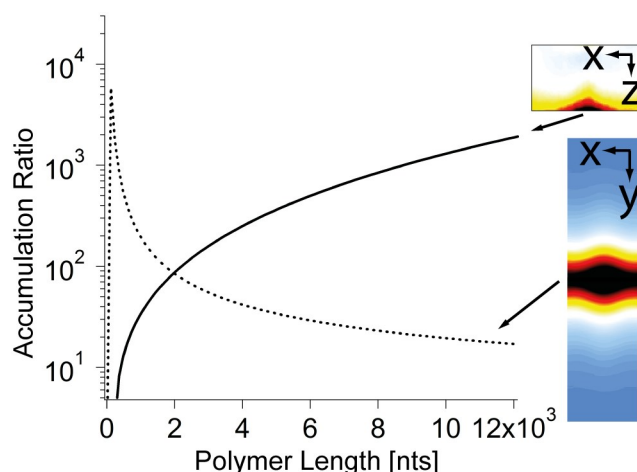
Figure S3. Calculated, steady state length dependence of thermal molecule trapping. Finite element simulations show that the thermal trap in x-y-direction accumulates predominantly short DNA (e.g. 37 bp for a 3500 x 50 μm compartment as used here), while the trap in x-z-direction prefers 21 kbp long strands (see Fig. S2).

DNA Gelation.

We use the term hydrogel for the found DNA with an estimated density of 0.01 g/cm³. This estimate is made by taking into account the initial total DNA content (initial concentration = 0.5 μM up to 10 μM) in the trapping volume of 3500 μm x 50 μm x 100 μm = 17.5 nl. This results in a maximum DNA content inside the trapping volume of 0.5 - 10 ng that can be incorporated into the gel with an estimated hydrogel-size of 1 mm x 20 μm x 20 μm = 0.4 nl. Accordingly, the DNA concentration inside the dense phase must be lower than 450 μM or 0.03 g/cm³. In comparison, dried DNA in the solid phase has a density of 1.4 g/cm³.[2] Polarization microscopy does not reveal any internal order as found in liquid crystal phases (see Fig. S9). We therefore conclude, that the found structure is a DNA hydrogel, defined as an amorphous and unordered, swollen structure of entangled, long DNA strands.

Single-stranded cross-polymerizing or branching 36 mer DNA **A** and double stranded DNA **X/Y** with a length of 95 base pairs and with sticky ends of 25 bases act as monomers for reversible polymerization by hybridization of their sticky ends. The dissociation constant of the polymer bond / sticky end was determined to be $K_D = 1 \mu M$ for the DNA **X/Y** monomer, with an identical sequence as in previous studies.[3] We trapped and gelated DNA with the same sequences discussed above but without any fluorescent labels in order to exclude cross-linking artifacts of the fluorophores. The fluorescent dye SybrGreen I was carefully flushed into the reaction chamber after the gelation of DNA in order to stain the hydrogel (Fig. S5).
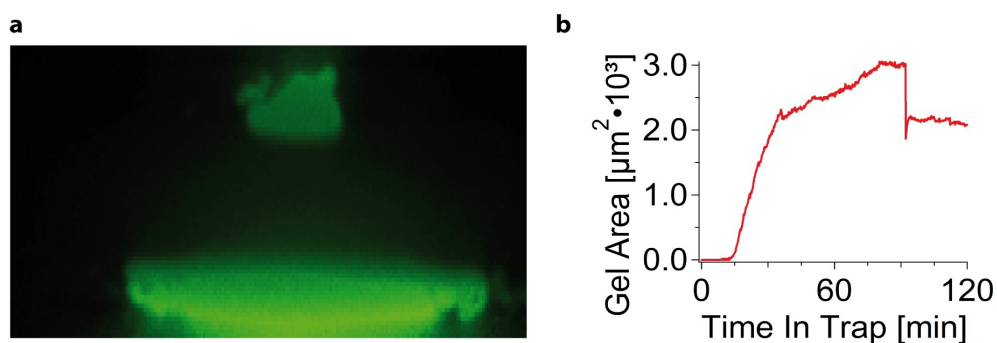
Figure S4. Gelation of **AT** DNA. (a) Image of gel (green) made of **AT** DNA (see table ST1) under the same conditions as for the other DNA **A**-**E**. (b) Analysis of gel formation of **AT** DNA.
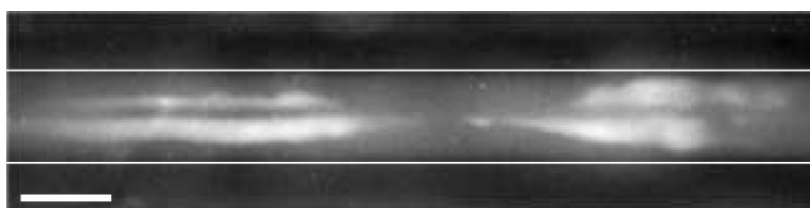

Figure S5. Gelation without fluorescent label present. Unlabeled DNA **X/Y** was trapped without optical control for ~1.5 h and post-stained with 10x SYBR Green I. The results exclude cross-linking of fluorescent molecules as possible mechanism for the gelation of DNA. Scale bar: 100 μm.

Timescales of gravitational and laser driven traps.

The two orthogonal thermal traps of a tilted pore were simulated by using thermoviscous pumping in a horizontally aligned capillary (Fig. S1/2).[4,5] The geometry is identical to the experimental situation, with a size of the thermal trap of 50 μm (width, x-axis) times 3500 μm (length, y-axis) times 50 μm (height, z-axis) and a temperature difference of 7 K along the x-axis. The three dimensional temperature field is calculated using finite element methods as described below. Fig. S6 illustrates the fast accumulation timescales of laser driven traps compared to a trap using gravitational convection. While in a gravitationally driven trap the relative accumulation in equilibrium is higher by a small margin (Fig. S6 a, after 100 min), the laser-driven trap reaches its equilibrium much faster (Fig. S6 b, after 10 min) due to faster pumping speeds. The trapping timescales for different DNA lengths show a similar behavior for both gravitational and laser-driven trap (Fig. S6 c). The laser-driven trap is however consistently 30x times faster.
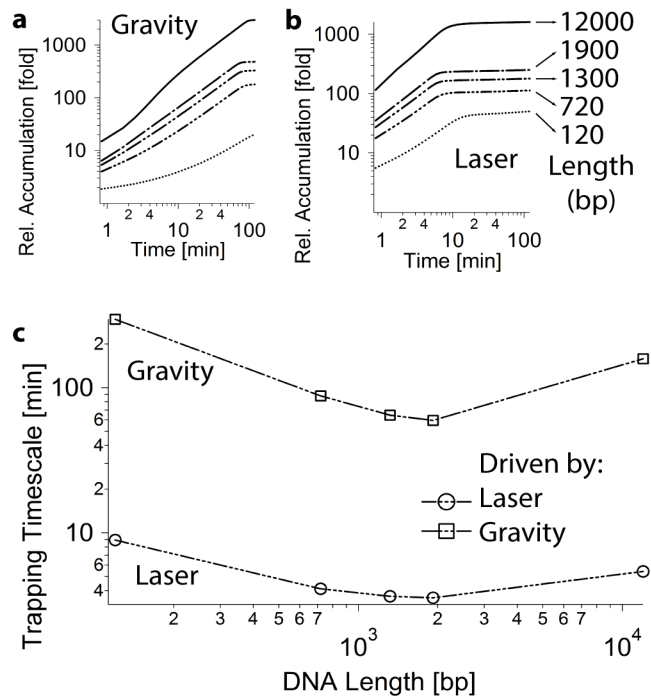
Figure S6. Simulated thermal trapping timescales for different DNA lengths in a pore of 50 x 3500 x 50 µm (width x length x width). (a, b) Gravitationally driven trap. Compared to the laser driven situation (b), the experimental thermal trap (a) would equilibrate much slower when driven only by gravity in an upright oriented condition. (c) Upright thermal traps show a similar trapping timescale characteristic over oligomer length. The laser driven thermal trap in the experiment is 30 x faster than the comparable gravitationally driven trap at the cost of a slightly reduced steady state accumulation of oligomers. Timescales were determined using an exponential relaxation model-fit of the numerical results from finite element simulations.

Theory and simulation. We implement the thermal trap by the combination of a convective fluid flow v_c and linear thermophoresis, the movement $v_T = -D_T \cdot \nabla T$ of biomolecules with a thermodiffusion coefficient D_T in a temperature gradient ∇T .[6] The length dependence of thermal trapping was calculated as done before.[7] A finite element simulation (Comsol) of the experiment was implemented using the previously measured temperature distribution as well as the flow velocities of both orthogonal convection flows using fluorescently labeled silica beads. We used fixed polymer lengths to qualitatively describe the interaction of both orthogonal thermal traps in the experiment because the timescales of trapping, hydrodynamics and polymerization kinetics are similar and make it impossible to perform a combined simulation.

Setup and Experimental Details

For the experiment, custom-made borosilicate capillaries (VitroCom, Mountain Lakes, NJ) with a rectangular cross section of 100 µm x 50 µm are fixated onto IR-transparent silicon wafers and covered with immersion oil and a sapphire cover slip. The wafers are cooled down to a 10 °C base temperature using Peltier elements (9502/065/018M, Ferrotec), while the temperature along the height of the capillary (50µm) is set to $T_{min} = 53\,°C$ and $T_{max} = 60\,°C$ via IR absorption.

A high precision syringe pump (neMESYS, cetoni) controls the flow speed and refilling of the capillary. The imaging is performed using a 40x objective (Plan-Neufluar 40x 0.9 NA, Zeiss; with 0.5x adapter and therefore 20x effective magnification) in a fluorescence microscope (Axiotech Vario, Zeiss) where two LEDs (590 nm and 470 nm, Thorlabs) and a dual view unit (Optosplit II, Cairn research) connected to a CCD camera (Sensicam, PCO) allow the recording of color separated FRET images.

An IR laser (TLR-20-1940, IPD Photonics) is focused inside the capillary with a custom built scanner lens system consisting of three lenses (L_A : Linos, G063095000, f = 15mm; $L_B = L_C$: Thorlabs, LA1422-C, f = 40mm) with lens separations of $\varDelta x_{L_A,L_B} = 57\text{mm}$, $\varDelta x_{L_B,L_C} = 45\text{mm}$ and $\varDelta x_{L_C,scanner} = 10\text{mm}$. The laser is responsible for heating the samples and driving the thermoviscous flow using scanning mirrors (6200-XY, Cambridge Technology). The 30 µm wide spot is thereby asymmetrically driven along the 2 x 3.5 mm scanning range, which transports water in the opposite laser direction during each run.[3-5] The microscopy stage and scanning mirrors are cooled using a refrigerated circulator (F12, Julabo).

Due to gravitation, the thermal gradient also drives a second convective flow that is orthogonal to the mentioned thermoviscous driven convection (Fig. S2). In combination with the thermal gradient, both flow contributions implement two thermal traps with different length selectivities: Short DNA is accumulated at the capillary center, while longer DNA and the DNA hydrogels are predominantly concentrated on the capillary bottom along a centered line in the y-direction .

The DNA **X/Y** was delivered in aqueous solutions in 100 µM and 200 µM concentrations for the labeled and unlabeled DNA, respectively, and immediately frozen. A 1 x PBS buffer (137 mM NaCl, 2.7 mM KCl, 10 mM $Na_2HPO_4 \cdot H_2O$, 2 mM KH_2PO_4) served as medium during the experiments.

The DNA **A**-**E** was chosen to be as simple and short as possible and consists therefore only of 36 G and C bases.

Before diluting the DNA for usage it was annealed by driving a temperature ramp from 95 °C to 10 °C with a cooling rate of 1 °C / 10 s to create defined starting conditions. The observation site (y = 710 µm) is offset from the accumulation center (y = 0 µm) in order to track the hydrogel formation on the bottom surface of the capillary.

We determined a 2-D temperature profile $T(x,y)$ of the filled capillary by measurements of the temperature dependent dye BCECF (2',7'-Bis-(2-Carboxyethyl)-5-(and-6)-Carboxyfluorescein). For the former, we switched from an asymmetrically driven laser to a symmetric pattern. This removed the thermoviscous flow but kept the IR absorption constant.

To determine the fluid flow velocity, we tracked 1 μm large green fluorescent silica particles (PSI-G1.0NH2, Kisker) under trapping conditions. We found the maximum fluid speed to be 43 ± 2 μm/s along the y-axis and 5 ± 1 μm/s along the z/x-axis. Due to their lower diffusion coefficient compared to DNA, the particles were not trapped but followed the fluid flow.
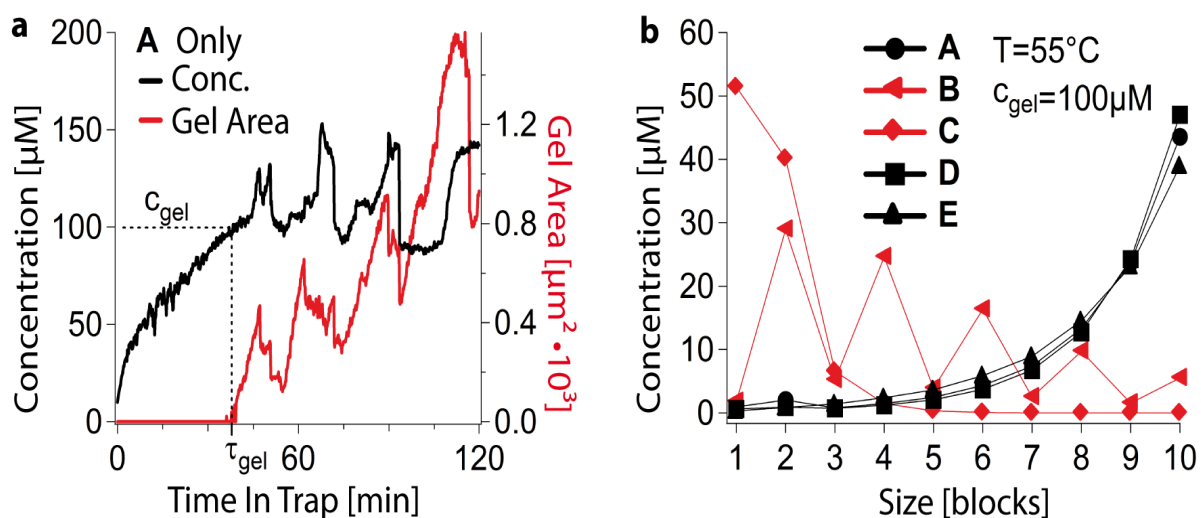

Figure S7. Gelation of DNA **A** and building block calculation. (a) Analysis of the DNA concentration from fluorescence intensity during a trapping experiment. It shows a gel formation starting at $c_{gel} \sim 100$ μM local concentration. The total gel area oscillates due to a continuous melting and formation of the gel. (b) Calculation of the concentration of hybridized strands (blocks) from DNA **A**-**E** at c_{gel}. It can be seen that for DNA **B** and **C**, which do not form a gel, the concentration decreases with block size, while it increases for DNA **A**, **D** and **E**.

Determination of gel area from experimental data

In order to derive the total amount of gel from the fluorescence data, we applied an automatic edge detection based image algorithm to every measured frame:

- Background noise (obtained by recording pure H_2O in the same capillary) is substracted from every picture.
- Every picture is divided by the first frame which corrects for uneven illumination.
- The result is first normalized to account for absolute intensity change between pictures.

- The result is then substracted by its own convolution with a blurring 7x7 filter-matrix with matrix elements $a_{i,j}=1$ for all I,j in order to correct for concentration differences of dissolved DNA by thermal trapping.
- The outcome is then convoluted with a 3x3 Gaussian matrix go correct single pixel errors in edge detection.
- In the resulting picture, uneven distributions of dissolved DNA without edges (=hydrogel) are corrected and form a Gaussion curve in the histogram. Gel structures with a visible contrast are not filtered out and lead to an increased tail of the Gaussian brightness distribution in the histogram. In order to get the gel-positions, all pixels with an intensity within 4σ of the gaussian distribution are skipped and the remaining pixels are considered to be gel-pixels.
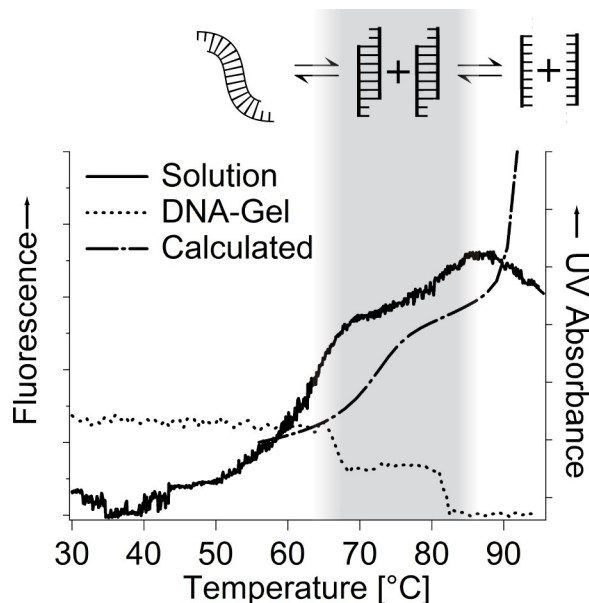

Figure S8. Melting analysis and calculation of DNA **X/Y**. Melting analysis (dotted line) of a hydrogel made from DNA **X/Y** using FRET and with dissolved DNA **X/Y** (solid line) using UV absorbance. The melting transitions of both measurements correspond to the melting temperatures of the sticky ends and the stem part of DNA **X/Y**. Interrupted line: Nupack calculation of the fraction of unbound DNA **X/Y** vs. temperature (1µM DNA conc., 150µM NaCl).

Melting analysis and calculation of DNA X/Y (Fig. S8)

To determine the melting points of the gel, we trapped DNA **X/Y** as described before until the gel had formed. We then switched off the thermoviscous flow but kept the temperature profile constant by symmetrically driving the laser along the trapping region. Starting from this, we slowly increased the base temperature of the Peltier elements from 10 °C to 94 °C while measuring the fluorescence intensity of the gel regions. Fig. S8, shows the fluorescence intensity profile of a DNA **X/Y** gel (dotted line) with increasing base temperature. Two distinct transition points can be observed, corresponding to the melting temperatures of the sticky ends (67 °C) and the stem part (83 °C). A

melting analysis of the DNA in solution (solid line) shows similar transitions. Here, 1 µM of DNA **X/Y** was analyzed in a 1x PBS solution using a Jasco V-650 spectrometer (260nm, Ramp rate: 0.2°C/min, intervals: 0.1 °C, 10 nm UV bandwidth, corrected vs 1xPBS blank). The interrupted line shows a calculation of the fraction of unbound bases of DNA **X/Y** vs. temperature using Nupack (nupack.org, melting analysis with complex size = 6, NaCl = 150 mM, MgCl2 = 0 mM, 1µM DNA concentration).[8] The calculation shows similar melting transitions at 65-75 °C and 85-90 °C compared to the UV absorbance and FRET measurements. FRET corrections were made as described in previous work.[3]
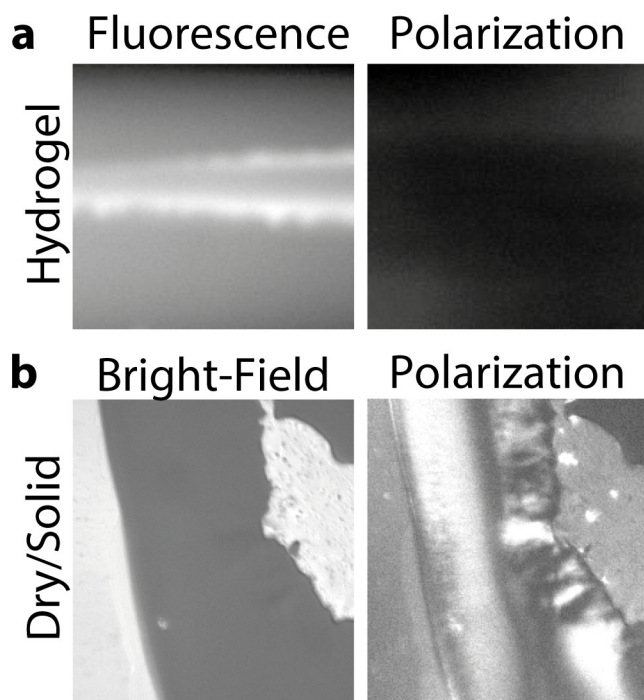

Figure S9. Polarization microscopy measurements of dried and gelated DNA **A**. (a) Hydrogel formation was inspected using fluorescence microscopy. Polarization microscopy with bright-field and fluorescence configurations did not show any birefringence, indicating an unordered structure like as extpected from a hydrogel. (b) Control: DNA **A** was also dried to obtain solid or liquid crystal phases of DNA. The polarization microscopy clearly shows birefringence, indicating aligned DNA strands.

SEM analysis of DNA gel (Fig. S1)

The DNA **X/Y** gel was extracted by first flushing the PBS out of the capillary using a small flow of not more than 0.5 nl/s and replacing it with pure water. This is necessary to remove most of the salt from the sample. We then increased the flow speed to separate the gel from the capillary. The behavior of a separate gel inside the capillary can be seen in Movie S02. The gel was flushed out of the capillary into a 5 µl droplet of pure water and allowed to dry at 4 °C. Scanning electron microscopy (SEM) images were taken with a Zeiss Ultra-55 Scanning Electron Microscope.

References:

[1] I. Schoen, H. Krammer, D. Braun, *Proc. Natl. Acad. Sci. U. S. A.* **2009**, *106*, 21649–21654.

[2] M. A. Śmiałek, N. C. Jones, S. V. Hoffmann, N. J. Mason, *Phys. Rev. E Stat. Nonlin. Soft Matter Phys.* **2013**, *87*, 60701.

[3] C. B. Mast, S. Schink, U. Gerland, D. Braun, *Proc. Natl. Acad. Sci. U. S. A.* **2013**, *110*, 8030–8035.

[4] F. M. Weinert, D. Braun, *J. Appl. Phys.* **2008**, *104*, 104701.

[5] F. M. Weinert, J. A. Kraus, T. Franosch, D. Braun, *Phys. Rev. Lett.* **2008**, *100*, 164501.

[6] S. Duhr, D. Braun, *Proc. Natl. Acad. Sci. U. S. A.* **2006**, *103*, 19678–19682.

[7] P. Debye, *Annalen der Physik* **1939**, *428*, 284–294.

[8] J. N. Zadeh, C. D. Steenberg, J. S. Bois, B. R. Wolfe, M. B. Pierce, A. R. Khan, R. M. Dirks, N. A. Pierce, *Journal of computational chemistry* **2011**, *32*, 170–173.

Danksagung

Ich möchte mich bei allen bedanken, die mich über die letzten Jahre unterstützt haben.

Mein erster Dank gilt natürlich **Dieter**, für die Möglichkeit, meinen Doktor in seiner Gruppe zu machen, für die interessanten Diskussionen und den Willen, bekannte Denkmuster zu durchbrechen und neue Ideen zuzulassen.

Ein großer Dank gilt auch den Braunies, alt wie neu, für die tolle Zeit. **Lorenz**, für... naja... er ist halt Lorenz. Ich hab das Gefühl ich sollte hier mehr über ihn schreiben aber das steigt ihm nur wieder zu Kopf. Danke auch den anderen Ehemaligen aus der Physik, **Ike**, **Georg**, **Susi**, **Peter** und die BWL connection mit **Vyara** und **Antje** für die anhaltende Freundschaft. Den **Braunies** Alan, Alex, Annalena, David, den Julians, Noel, Patrick, Philipp, Thomas, Victor, besonders auch Christina und allen weiteren für die gute Zusammenarbeit, Diskussionen an der Kaffeeecke und ihre Freundschaft. Ein ganz besonderer Dank auch an **Zhenya** für die Yogastunden, Handstand (irgendwann schaffen wir das noch) und die gemeinsame Zeit. **Christof** dafür, dass er von Anfang bis Ende mit Rat und Tat dabei war, ohne ihn wäre das ganze nicht gegangen. Danke auch an **CeNS** für die tollen Events.

Ich danke auch all meinen Freunden, besonders den **Holis** und der restlichen **Mensacrew**. **Lorenz** und **Regina** für die Videoabende und Quizduelle, **Illei** für die Reisen und **Patrick** und **Schorschi** für den Tetris-Fanatismus. Besonders auch **Muki** und **Maya** für die Anhaltende Freundschaft und Unterstützung. Und natürlich bei allen last-minute Korrekturlesern.

Besonders möchte ich mich auch bei meiner Familie bedanken. Bei meiner **Mutter** für die jahrelange Unterstützung und das anhaltende Interesse an meiner Arbeit und meinem **Vater** für den ungebrochenen Glauben an mich. Bei meinen **Brüdern** für die Age of Empires Sessions und meiner **Schwester** für die tollen Wiesn-Abende und Gespräche.